Structural Characteristics, Vacancy Arrangements, and Copper Clustering on the TiO_2 (110) Surface: A First-Principles Theoretical Study.

by

Scott J. Thompson

(Under the direction of Steven P. Lewis)

Abstract

TiO_2 has a wide variety of industrial applications and has received significant attention from the experimental and theoretical communities. Using *ab-initio* Density Functional Theory calculations to study the (110) surface of TiO_2, my research has resulted in a substantial increase in knowledge for this important material. Specifically, investigations were conducted on (1) the structural properties of the (110) surface, (2) interactions between bridging O vacancies, and (3) the adsorption of Cu atoms and nanoclusters. In this work, a compelling case is presented to describe the structure of TiO_2 and similar systems in terms of bond lengths and angles. Additionally, the wide variety of experimentally observed bridging O vacancy arrangements are explained using a vacancy interaction model. Furthermore, Monte Carlo simulations of this model lead to first ever predictions of specific ordered vacancy phases for this system. Finally, studies involving Cu adsorption on the stoichiometric and reduced TiO_2 surfaces provide insight into the diffusion of Cu atoms and their growth into nanoclusters and islands.

Index words: TiO_2, Cu Nanoclusters, O Vacancy, DFT, Monte Carlo

Structural Characteristics, Vacancy Arrangements, and Copper Clustering on the TiO_2 (110) Surface: A First-Principles Theoretical Study.

by

Scott J. Thompson

B.S., Georgia Institute of Technology, 1995

M.S., Georgia Institute of Technology, 1997

A Dissertation Submitted to the Graduate Faculty

of The University of Georgia in Partial Fulfillment

of the

Requirements for the Degree

Doctor of Philosophy

Athens, Georgia

2007

Structural Characteristics, Vacancy Arrangements, and Copper Clustering on the TiO_2 (110) Surface: A First-Principles Theoretical Study.

by

Scott J. Thompson

Approved:

Major Professor: Steven P. Lewis

Committee: David P. Landau
William M. Dennis

Electronic Version Approved:

Maureen Grasso
Dean of the Graduate School
The University of Georgia
May 2007

Dedication

To my son and daughter, Elliot Grey and Elizabeth Winter Thompson.

Acknowledgments

I would like to thank my advisor, Steve Lewis, and the other members of my committee, David Landau and Bill Dennis, for their numerous contributions to my academic and research pursuits. Additionally, I would like to thank all of my friends, family, and coworkers for everything they have provided, from motivational thoughts to a new perspective on a difficult problem. I also wish to thank my wife, Samantha, son, Elliot, and daughter, Winter, for their continuous unwavering support. To everyone mentioned above, "Thank You", I could not have done it without you!

Table of Contents

List of Figures

List of Tables

Chapter 1

Introduction

Developing new ways of producing energy that do not rely on fossil fuels, efficiently detecting harmful and potentially dangerous compounds, and fighting the unwanted spread of newly discovered and potentially epidemic diseases are all very important problems facing today's society. Research into these problems, and many others, are similar in that some of the most successful and promising strategies involve semiconductor photocatalysists. Titanium dioxide, TiO_2, is one of the most significant and promising photocatalysists being investigated, and theoretical insight into the physical properties and structure that correlate with the photocatalytic activity are highly anticipated in the experimental community [1]. Besides the characteristics that make TiO_2 particularly well suited to use as a photocatalyst, there are numerous additional industrial applications for this important material. However, my research is primarily devoted to the study of fundamental materials properties related to the catalytic behavior of TiO_2 (110) surfaces. As presented in the following chapters, I have focused on understanding the surface structural characteristics, defect interactions, and Cu absorbtion properties for the (110) surface of TiO_2.

A discussion of the numerous industrial and scientific applications that use TiO_2 is presented in Chapter 2. Since my research focuses on the catalytic properties of this important material, particular attention is given to the structural characteristics possessed by a good catalyst. Furthermore, the multitude of ways in which the catalytic properties of semiconductor photocatalysists can be improved are also described. In particular, the existence of defects and adsorption of metals on the TiO_2 surface are

discussed in depth, since both have been shown to significantly effect the catalytic activity [1–5].

The majority of research presented in the following chapters employs first-principles total-energy calculations, which are done within the framework of Density Functional Theory (DFT) [6]. This robust quantum mechanical approach is a well-proven method for studying the complex behavior of crystal surfaces. In particular, my calculations were performed using the Vienna Ab-Initio Simulation Package (VASP) [7–9]. A detailed discussion of the theoretical framework underlying these *ab-initio* calculations is provided in Chapter 3. Additionally, extensive information is presented for the specific settings and computational approximations available in VASP, which has found wide use in the theoretical materials physics community [10–16]. One of the main reasons for the popularity of VASP is its incorporation of ultrasoft pseudopotentials [17, 18], which significantly reduces the computational time required to study a particular problem. More details on ultrasoft pseudopotentials will also be provided in Chapter 3. Another advantage of VASP is that significant effort has been spent to make it computationally efficient, which allows for the study of relatively large systems (on the order of hundreds of atoms) by electronic structure standards. The ability to perform relatively quick calculations on large systems is essential for my investigations on the TiO_2 (110) surface.

Calculations on the rutile crystal structure of bulk TiO_2 are presented in Chapter 4. While elementary, these calculations are an essential first step in understanding the characteristics of the surface structure. The experimental and theoretical structural data on this material are both comprehensive and in good agreement [19–22]. This vast wealth of available data allows for detailed testing of the computational approximations implemented in my investigations. Specifically, significant investigations on the convergence of the calculated total energy, atomic positions, bond lengths, and lattice parameters were conducted to optimize the precision of my calculations within

the constraints of the available computational resources. A subtle but important consideration in the preliminary study of bulk TiO_2 pertains to the effects structural symmetries have on the transition from the bulk crystal structure to the TiO_2 (110) surface. This issue is also discussed at length in Chapter 4.

Surprisingly, given the importance of the TiO_2 (110) surface, there are long-standing discrepancies among earlier experimental [23] and theoretical [13, 24–31] studies on the surface structure. The combination of my precise theoretical results [32, 33] and recent experimental data that provides a more accurate account of the structure at the surface boundary [34], resolves these structural discrepancies [32]. These discrepancies, as addressed in Chapter 5, are partially due to the significant effects that many commonly used computational approximations have on the TiO_2 (110) surface structure. Additionally, a significant portion of the observed discrepancies relates to the common practice of reporting surface structures by giving absolute atomic positions. As discussed in Chapter 5, reporting an atom's displacement from its bulk terminated position, while convenient, relies on an arbitrary reference point, not a germane physical characteristic. Therefore, in order to obtain a good comparison between experiment and theory, the same reference positions for each atom must be consistently applied. Further complications arise due to the fact that both experimental and past theoretical results have only been able to obtain data on atoms relatively near the surface. More recent analysis on thicker surfaces reveals that the structural changes caused by forming the (110) surface extend much deeper than previously anticipated [32, 35]. However, all of these issues can be resolved by focusing on physical quantities, such as bond lengths and angles, that do not rely on a non-physical reference point [32, 33]. This makes a compelling case to represent the structures of TiO_2 and other covalently bonded crystals in terms of bond lengths and angles instead of atomic positions. Another issue presented in Chapter 5 is the development of an efficient and accurate structural model for the TiO_2 (110) surface.

The resulting relatively small (24 atom) primitive slab unit cell allows for in-depth investigations on the effects of defects and adsorbates on TiO_2 (110).

The first of these investigations, the inclusion of defects on the surface, is presented in Chapter 6. Particular focus is placed on the most energetically favorable, and therefore most abundant, type of defect: bridging O vacancies [36, 37]. At relatively low defect concentrations, experimental [38, 39] and theoretical [24, 28, 29, 36, 37, 40–45] studies have shown a preference for a new bridging O vacancy to form at a site that is isolated from other vacancies already present on the surface. Experimental work has also found clustering of vacancies at slightly higher defect concentrations [46], and ordered vacancy arrangements at very high defect concentrations [47, 48]. Previously, this type of behavior had not been observed or explained theoretically. Chapter 6 presents a detailed account for the development of a vacancy-vacancy interaction model using DFT total-energy calculations. This model provides, for the first time, a theoretical basis for understanding the diverse array of experimentally observed vacancy arrangements [38, 39, 46–48]. Furthermore, this interaction model can be used in conjunction with Monte Carlo techniques [49] that allow for the simulation of surfaces with sizes comparable to those seen experimentally. As described in Chapter 6, this results in a new prediction of two ordered vacancy phases and qualitatively reproduces particular aspects of the experimental observations.

The study of adsorbates on the TiO_2 (110) surface, as presented in Chapters 7 and 8, focuses on the adsorption of Cu atoms. Chapter 7 looks at the adsorption and diffusion characteristics of single Cu atoms on the stoichiometric and reduced surfaces, i.e. TiO_2 surfaces without and with O vacancies respectively. Specific attention is paid to the effects that a surface with interacting O vacancies has on an adsorbed Cu atom, which are significantly different from those due to an isolated vacancy. The formation of two- and three-atom nanoclusters, by the adsorption of additional Cu atoms, is the primary focus of Chapter 8. Comparison is made to experimentally

observed Cu nanocluster formation [50], as well as the further growth of these clusters into Cu islands [47, 48, 51–55]. Experimental studies of Cu island formation have all agreed on the clustering of Cu into an fcc structure (the natural state of bulk Cu [56]) when adsorbed on the TiO_2 (110) surface. However, different orientations of the fcc Cu islands relative to the surface have been observed [47, 55], as have the growth of different shapes and sizes of Cu islands [47, 48, 51–55]. While DFT total-energy calculations are not well suited to the study of Cu island formation, due to the large number of atoms and large unit cell size that would be required, they can be applied to study the causes of differences in initial growth patterns. As discussed in Chapter 8, the resulting Cu island orientation and size are found to correlate with the concentration and arrangement of O vacancies on the TiO_2 surface.

A summary of the many important results from my investigations is presented in Chapter 9. Additional discussion is also included on particular aspects of my research that merit further investigation in the future.

Chapter 2

Background Information

2.1 Applications Involving TiO_2

Titanium dioxide is a highly popular material in the industrial, experimental, and theoretical communities. This is due in part to the high availability of this important material from numerous manufacturers as well as the ease of preparation in a laboratory setting. One result of the wide range of industrial and experimental applications is that theoretical investigations, with the goal of understanding the fundamental aspects of TiO_2 surfaces and interfaces, are being pursued by many research groups. In addition to the favorable impact these studies are bound to have on the current industrial uses and experimental investigations, TiO_2 is also highly popular in theoretical surface science studies, due to its status as a model metal-oxide system [41, 57], where the results obtained for this particular material provide insights into the physical and electronic structure of a wide range of metal-oxide systems in general.

Current industrial interest is dominated by the use of TiO_2 in powdered form as a pigment, where due to its high opacity, brilliant whiteness, excellent covering power and resistance to color change, it is valuable for a wide range of applications [58]. TiO_2 can be found in everyday products such as white paint, plastics, and ink, but humans can share an even closer relationship with this important material since it is also found in food, sunscreen, cosmetics, and most toothpastes. Additionally, photoelectrolysis was demonstrated for the first time in 1975 when exposure of a TiO_2 electrode to near-UV light resulted in the decomposition of water into oxygen

and hydrogen [59]. This provides another industrial use for TiO_2, solar cells, which can produce both electrical energy and hydrogen.

Many additional applications for TiO_2 are currently under scientific investigation. For example, TiO_2 is used as a semiconductor gas sensor, where current studies are focused on understanding the interaction of the gas molecule with the surface of the semiconductor. In addition to the detection of gases at low concentrations, TiO_2 photocatalysts have been shown to purify the surrounding atmosphere of foul smelling gases such as ammonia, hydrogen sulfide, and acetaldehyde when exposed to the relatively week UV illumination that is produced by a fluorescent light bulb [1]. TiO_2 powders have also played a role in the photochemical reduction of CO_2 in experimental studies focused on the recycling of this gas [1].

Further applications are currently planed for industrial use in the very near future. One such example involves the surface interaction of TiO_2 with water. When TiO_2 films are prepared with a certain percentage of SiO_2, the film acquires superhydrophilic properties under UV illumination [60], which results in water spreading uniformly across the surface. This property leads to the production of self-cleaning surfaces, such as windows, since rainfall can easily displace stain-causing compounds, as well as anti-fogging and anti-beading windows and mirrors, which are soon to be equipped on Japanese cars [1]. Additionally, TiO_2 surfaces also possess a sterilization effect. Due to its strong oxidative ability, photoexcited TiO_2-coated surfaces are adept at decomposing most organic compounds, including bacteria. Specifically, studies have shown that TiO_2-coated surfaces under weak UV exposure, such as typical indoor room lighting, result in significant destruction of viable bacteria, such as *E. Coli* and *MRSA* [1]. Thus, the use of TiO_2 coated tiles and walls in hospitals and other indoor living areas could significantly reduce the occurrence of infection caused by these harmful bacteria.

2.2 Optimizing the Catalytic Properties

The photocatalytic activity of semiconductors, such as TiO_2, is governed by three basic properties of the system [1]. The first of these properties relates to the light adsorption of the material, which is heavily influenced by the bulk structure of the semiconductor solid, and therefore is rather difficult to modify. However, systems may be designed to ensure that almost all of the incident photons are adsorbed, so this property will negligibly influence the rate of the desired reactions. Assuming all incident photons are adsorbed, a set number of electron-hole pairs are produced, and these pairs proceed to react in two distinct ways.

The desired reaction is that of reduction and oxidation occurring at an adsorbate, where the primary consideration then becomes the rate of electron and hole transfer across the semiconductor-environment interface onto the adsorbate. This strongly correlates to the amount of adsorbate on the surface of the semiconductor, which in turn depends primarily on the surface area of the semiconductor. Studies have shown that, as the surface area of the photocatalyst increases, additional atoms can be adsorbed, and an increase is seen in the reaction rate [61]. However, this relationship assumes that enough of the photocatalyst is present so that all of the incident photons are adsorbed.

Secondly, it has been shown that the recombination rate of the electron-hole pairs has a large influence on the photocatalytic activity, since a significant number of electron-hole pairs could potentially recombine before reaching the adsorbate [62]. While the exact amount of recombination is rather difficult to estimate, it is believed to be effected by the density of crystal defects in the semiconductor [63]. This poses a potential conflict with the desire to increase the surface area, since the surface of a crystal is an inherent defect in the crystal structure.

The catalytic activity of semiconductors can also be improved by introducing a co-catalyst to the surface. Specifically, when metals are added to the surface of a

transition metal oxide, the catalytic activity can increase due to the onset of so-called strong metal/support interactions [2]. For example, TiO_2 possesses a high oxidation ability and a relatively lower reduction ability due to its electronic band structure. This is seen explicitly in the photocatalytic dehydrogenation of alcohols, where a negligible amount of hydrogen gas is liberated from the bare TiO_2 surface. However, when a small amount of platinum is added to the surface, the rate of hydrogen gas production vastly increases [3], which is directly related to the reduction ability of the co-catalysts. It has been shown that other metals such as gold, silver, and copper have similar effects [4].

It is apparent from the above discussion that crystal structure, particle size, and surface area all play an important and complex role in the production of highly efficient photocatalysts. Furthermore, the inherent catalytic properties can be enhanced by making use of the effects of the strong metal/support interactions that occur upon the addition of a metal to the semiconductor surface. However, this enhancement is a rather complex phenomenon, as witnessed in experiments that have shown a decrease in the catalytic activity due to excess loading of metals [5]. Therefore, the minimum requirements to produce highly active and efficient photocatalysts are the optimization of the parameters mentioned above. Due to the large number of potential photocatalytic systems that could be produced, the development of accurate theoretical models of these photocatalysts could greatly aid in the prediction and optimization of promising new materials and configurations.

2.3 Cu on the Rutile TiO_2 (110) Surface

As previously mentioned, when metal atoms such as Pt, Au, Ag, and Cu are adsorbed on the (110) surface of TiO_2, the catalytic characteristics of the semiconductor are enhanced. While significant resources have been devoted to the properties of Group VIII metals (such as Pt) as well as Au atoms and clusters on TiO_2 [10–16, 64, 65],

fewer studies have focused on the addition of Cu [14, 64, 66]. In particular, there is some disagreement as to weather Cu-TiO_2 exhibits the same strong metal/support interactions and enhanced photocatalytic properties of Pt-TiO_2 [67]. In addition to the role of Cu in catalytic reactions, recent experimental evidence has shown interesting growth modes for Cu on the TiO_2 (110) surface. Specifically, as the amount of Cu adsorbed on the surface increases, the Cu structures formed on the surface transform from small nanoclusters consisting of a few atoms [50], to larger Cu islands [47, 48, 51–55], and eventually thin films [68].

Focusing initially at the small Cu nanoclusters, experiments in which Cu is deposited on the surface via chemical reactions have yielded the formation of Cu trimers on the surface. These Cu trimers were shown to bond primarily to the O atoms on the surface and to have Cu-Cu bond lengths comparable to that of bulk Cu in the fcc crystal structure [50]. Also, the plane containing the 3 Cu atoms was found to be inclined approximately -30° from the surface plane [50]. Addition of a second Cu trimer was shown to occur on top of the first, such that Cu growth occurred roughly perpendicular to the TiO_2 (110) surface.

For larger amounts of Cu added to the surface, experiments used vapor deposition in lieu of specific chemical reactions. These experiments resulted in the formation of Cu islands on the TiO_2 (110) surface, where the height and diameter of the islands appeared to vary from one experiment to another [47, 51–55]. Observations of these systems also showed that both the orientation of the Cu islands with respect to the TiO_2 surface and the defect arrangements on the TiO_2 substrate differed among the various experimental studies. Furthermore, experiments have shown that the addition of O_2 gas to the Cu-TiO_2 system results in the dissociation of the Cu islands [52]. Along with recent theoretical calculations that focused on the roles of isolated O defects [14], this result suggests that a definitive role is played in the formation of Cu islands by O defects on the surface of TiO_2.

Chapter 3

First-Principles Total Energy Methodology

3.1 Overview

One of the great challenges in theoretical physics has been to develop computational methods that can accurately and efficiently treat the interacting system of many electrons and nuclei, which determine the nature of atoms, molecules, and condensed matter. Theoretical insights into the structural, electronic, optical, and magnetic properties that result from the solution of this problem are crucial to both the advancement of understanding of the underlying physical processes at work in these complex systems, as well as the development of interesting and useful new materials. Arguably, the most successful and widely used approach for quantitative quantum mechanical calculations of real materials and molecules is Density Functional Theory (DFT), which provides the theoretical basis for the inclusion of many-body effects into solvable independent particle equations [6]. In the following sections, I will discuss the development of DFT and many of the methods and approximations used in my first-principles total energy calculations, which is the basis for my research involving the TiO_2 surface.

3.2 Density Functional Theory

A collection of atomic nuclei and their corresponding electrons constitute a many-body fully-interacting problem that can be completely described by the Hamiltonian shown in equation 3.1. The terms in the Hamiltonian represent, in order from left

to right, the kinetic energy of the electrons, the potential energy between the nuclei and electrons, the potential energy corresponding to the electrons interacting with each other, the kinetic energy of the nuclei, and finally the potential energy of the nuclei interacting with each other. In equation 3.1 and future equations, I make use of the notation of capital letters representing nuclear variables and lowercase letters for electronic variables. Also, Z_I corresponds to the atomic number of the I^{th} nucleus, e is the proton charge, and m_e and M_I represent the mass of the electron and the I^{th} nucleus respectively. Solving this problem requires finding the energy eigenvalues and many-body wave functions of this Hamiltonian by solving the corresponding time-independent Schrödinger equation. However, this is an intractable problem since for N total electrons and nuclei, the solution scales as $(3N)^{(3N)}$. The exponential scaling arises from the interactions of each particle with the remaining N-1 particles, and the coefficient 3 is from the fact that each of the N particles have three spatial degrees of freedom.

$$\hat{H} = -\frac{\hbar^2}{2m_e}\sum_i \nabla_i^2 - \sum_{i,I}\frac{Z_I e^2}{|\mathbf{r}_i - \mathbf{R}_I|} + \frac{1}{2}\sum_{i\neq j}\frac{e^2}{|\mathbf{r}_i - \mathbf{r}_j|} - \frac{\hbar^2}{2}\sum_I \frac{1}{M_I}\nabla_i^2 + \frac{1}{2}\sum_{I\neq J}\frac{Z_I Z_J e^2}{|\mathbf{R}_I - \mathbf{R}_J|}, \tag{3.1}$$

In general, only a single reasonable approximation can be made to equation 3.1, which is that the kinetic energy of the nuclei is small and can be safely neglected. This occurs since the mass of the nucleus is at least three orders of magnitude larger than the electronic mass. Therefore, in the adiabatic approximation, where $\frac{1}{M_I}$ is small, we can neglect the nuclei kinetic energy term. However, this assumption can be taken a step further, and the mass of the nuclei can be considered infinite, which corresponds to the Born-Oppenheimer approximation [6]. In this case, the kinetic energy of the nuclei is set to zero, and the potential energy corresponding to the internuclear interaction becomes constant, since all of the nuclear positions, R_I's, can be interpreted as fixed in space. An additional way to interpret this approximation

is to allow for the nuclei to move, as long as the electrons instantaneously relax to the ground state for the new nuclear configuration. Regardless of the interpretation chosen, this approximation results in a new Hamiltonian for the fully interacting electron problem as shown in equation 3.2, where the potential energy term for the interactions between the now-fixed nuclei is a constant denoted by E_{II}. It is also evident that the second term in equation 3.2 can be expressed as an external potential, V_{ext}, which corresponds to a summation of the potentials between each electron and the positive charge density produced by the now fixed nuclei which are external to the system of electrons. Even though a significant reduction in the number of particles has occurred with the use of the Born-Oppenheimer approximation, as only the electrons remain, the equation is still not currently solvable in the general case.

$$\hat{H} = -\frac{\hbar^2}{2m_e}\sum_i \nabla_i^2 - \sum_{i,I}\frac{Z_I e^2}{|\mathbf{r}_i - \mathbf{R}_I|} + \frac{1}{2}\sum_{i\neq j}\frac{e^2}{|\mathbf{r}_i - \mathbf{r}_j|} + E_{II} \tag{3.2}$$

Important inroads into finding a solution were made in 1964 with the proof of the Hohenberg-Kohn theorems [69]. The first of these connects the external potential for a system of interacting particles to the ground-state particle density, $n_o(\mathbf{r})$, by showing that $n_o(\mathbf{r})$ uniquely determines V_{ext}, except for a constant. The second theorem proved that a universal functional of the energy, in terms of the particle density, can be defined for any given external potential. The global minimum of this functional was shown to be the ground-state energy of the system, and the density that minimizes the energy functional was shown to be the ground-state particle density. An important corollary arises from the first theorem, which provides a way to fully determine the Hamiltonian of the system. In principle, since the Hamiltonian is fully determined, every property of the system is uniquely determined. Therefore, the ground-state particle density determines the many-body wavefunctions and corresponding properties for all states, ground and excited. However, while these theorems provide important insights into

the problem, they do not provide a practical method for solving the fully interacting electron problem, since a method for determining the ground-state particle density is not specified.

The method for determining the ground-state particle density was provided a year later through the Kohn-Sham Ansatz [70], which assumes that the ground-state particle density of the fully interacting system is identical to that of some fictitious, non-interacting system. Therefore, the difficult interacting problem that, in practice, isn't solvable can be replaced with a much simpler non-interacting problem that can be more efficiently solved. This occurs since the computational requirements now scale as $(3N)^r$ where N now represents the number of electrons and r is a small whole number that depends on method choice. One problem does still exist, approximating the complicated and unknown many-body electron-electron interactions such that the ground-state particle density obtained is identical to that of the real problem. Therefore, determining the ground state properties of the fully interacting problem rests upon how good our approximation of these interactions are.

$$V_{Hartree}(\mathbf{r}) = -\, e \int \frac{\rho(\mathbf{r}')}{|\mathbf{r} - \mathbf{r}'|}\, \mathrm{d}\mathbf{r}' \tag{3.3}$$

$$\rho(\mathbf{r}) = -\, e\, n_o(\mathbf{r}) = -\, e \sum_i |\psi_i(\mathbf{r})|^2 \tag{3.4}$$

One way, although not a very accurate one, to approximate these electron-electron interactions is to assume the electrons are independent, but that each electron interacts with some smooth, classical charge density produced by the remaining electrons [71]. The resulting Hartree potential, as shown in equation 3.3, can be found exactly if the charge density, defined in equation 3.4, is known. However, as seen in the equations above, in addition to neglecting the complicated many-body interaction between the electrons, this approximation also includes a nonphysical self-interaction

term. This term arises because the charge density is found by the sum over all of the electrons, which includes the electron that is interacting with the charge density. This nonphysical self-interaction term must be (and is) accounted for in order to avoid significant errors, and the details concerning how this is accomplished are presented in the next section. However, the true genius lies not in using the Hartree approximation, but by adding and subtracting the Hartree potential to the right hand side of equation 3.2. This results in the Kohn-Sham Hamiltonian, equation 3.5, where the exchange-correlation potential, defined in equation 3.6, contains all of the many-body electron-electron interaction terms. Both defining the physical meaning of $V_{XC}(\mathbf{r})$ and discussing how it is approximated are presented in detail in the following section. For the moment, assuming a good approximation for $V_{XC}(\mathbf{r})$ exists, the Kohn-Sham Schrödinger-like equations, shown in equation 3.7, for $i = 1 \ldots$N, are obtained, where ε_i correspond to the Kohn-Sham eigenvalues.

$$\hat{H}_{KS} = -\frac{\hbar^2}{2m_e}\sum_i \nabla_i^2 + V_{ext}(\mathbf{r}) + V_{Hartree}(\mathbf{r}) + V_{XC}(\mathbf{r}) + E_{II} \tag{3.5}$$

$$V_{XC}(\mathbf{r}) = \frac{1}{2}\sum_{i\neq j}\frac{e^2}{|\mathbf{r}_i - \mathbf{r}_j|} - V_{Hartree}(\mathbf{r}) \tag{3.6}$$

$$\hat{H}_{KS}\ \psi_i(\mathbf{r}) = \varepsilon_i\ \psi_i(\mathbf{r}) \tag{3.7}$$

An iterative process, as illustrated in the flow-chart in figure 3.1, is then used to solve these equations. For reasons of clarity and brevity, several items have not been included in either the flow-chart or the previous descriptions. Specifically, extensive time and effort is used to make a good initial guess at the initial particle density, as well as mixing the old and new particle densities prior to the next iteration. Additionally, the electron spin must also be included in the calculation. The end result is the determination of the ground-state charge density and single-particle wave functions

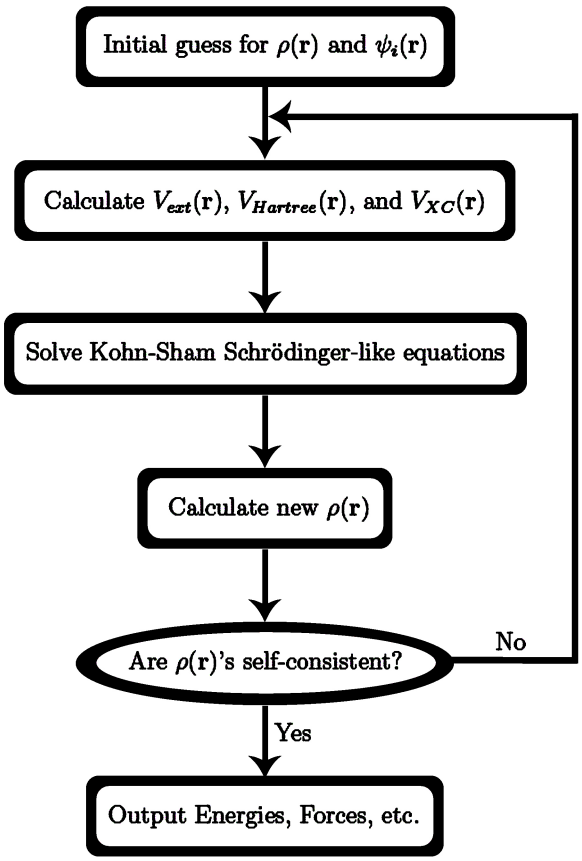

Figure 3.1: Schematic representation of the iterative process used to solve the Kohn-Sham Schrödinger-like equations for a DFT calculation.

for the fictitious non-interacting system. Applying the Kohn-Sham Ansatz [70] and the Hohenberg-Kohn Theorems [69] results in the solution for the ground state of the many-body, fully interacting system, and, in principle, allows for the determination of all ground and excited state properties of the system.

3.3 Exchange and Correlation

Exactly how well the solution of the solvable non-interacting system compares with the fully interacting problem rests upon the validity behind the approximations that enter into the exchange and correlation term. In order to understand these approximations, it is important to first have a basic understanding of the physics behind both the exchange and the correlation components of the interactions. To illustrate the properties of the exchange and correlation terms, it is convenient to express the Kohn-Sham Hamiltonian, as described in equation 3.5, in its energy-functional form, which is done by taking the expectation value. The results, shown in equation 3.8, describe the Kohn-Sham energy as a functional of the particle density, $\mathrm{n}(\mathbf{r})$, which is the expectation value of the density operator as defined in equation 3.9. The exact definition of the exchange-correlation energy, E_{XC}, is the difference between the sum of the electron-electron potential energy and the electron kinetic energy of the actual fully interacting many-body system and that of the non-interacting, Kohn-Sham system. Previously, only the potential-energy portion of E_{XC} was defined, and the physical explanations that follow will focus on this aspect, since the understanding behind the interactions and their approximations flow naturally from a discussion focused on this portion. However, it is important to remember that the kinetic energy of the system also depends on the many-body electron-electron interactions, and this must be accounted for in the exchange-correlation approximation in order to provide a more accurate model of the real interacting system [6].

$$E_{KS}[n] = T_o[n] + E_{ext}[n] + E_{Hartree}[n] + E_{XC}[n] + E_{II} \tag{3.8}$$

$$\hat{n}(\mathbf{r}) = \sum_i \delta(\mathbf{r} - \mathbf{r}_i) \tag{3.9}$$

$$E_{Hartree}(\mathbf{r}) = \frac{e^2}{2} \int \int \frac{n(\mathbf{r}')n(\mathbf{r})}{|\mathbf{r} - \mathbf{r}'|} \, \mathrm{d}\mathbf{r}'\mathrm{d}\mathbf{r} \tag{3.10}$$

Recall that the potential-energy portion of E_{XC} is defined by the difference between the electron-electron potential energy of the fully interacting system and the Hartree energy, which as shown in equation 3.10, is the electron-electron potential energy for to a classical, non-interacting system. Until this point, the spins of the electrons have been neglected. However, one consequence of the Pauli exclusion principle, is that two electrons with the same spin, σ, can not be at the same position in space, or, more generally, that no two electrons can possess the same quantum numbers. The exchange contribution [72] to the E_{XC} takes this into account, and assuming the wave functions are orthonormal, the exchange energy, E_{ex}, can be expressed as shown in equation 3.11. Two properties of E_{ex} are immediately apparent when written in this form. First, E_{ex} is zero when the electron spins are different, which makes sense, since the Pauli exclusion principle would not apply in this case. Therefore, it is obvious that E_{ex} only accounts for interactions between electrons with the same spin. Second, if a single electron system is studied, the non-zero E_{ex} will be equal in absolute value to $E_{Hartree}$. As a result, E_{ex} cancels the spurious, non-physical self-interaction term in the $E_{Hartree}$ that was introduced when defining the Hartree potential in the previous section.

$$E_{ex} = -\frac{e^2}{2} \sum_\sigma \int \int \frac{\delta_{\sigma\sigma'} |\sum_i \psi_i^{\sigma *}(\mathbf{r}) \psi_i^{\sigma}(\mathbf{r}')|^2}{|\mathbf{r} - \mathbf{r}'|} \, \mathrm{d}\mathbf{r}'\mathrm{d}\mathbf{r} \tag{3.11}$$

$$E_{ex} = \frac{e^2}{2} \int n(\mathbf{r}) \int \frac{n_{ex}(\mathbf{r}')}{|\mathbf{r} - \mathbf{r}'|} \, \mathrm{d}\mathbf{r}' \mathrm{d}\mathbf{r} \tag{3.12}$$

Another way to interpret the interaction underlying E_{ex} is to notice that if an electron is at some position $\mathbf{r}$ in space, then the charge density from all of the remaining electrons with the same spin in the system would have a hole, or lack of charge, in the vicinity of $\mathbf{r}$. Mathematically, E_{ex} can be written as shown in equation 3.12, where the interaction is now explicitly expressed as that of each electron interacting with its corresponding exchange hole [6]. There are two stringent conditions placed on the exchange hole density. First, the integration over primed space must yield one missing electron per electron at any point $\mathbf{r}$, resulting in a sum rule. The second is that n_{ex} is always negative. Physically, this allows for the interpretation of E_{ex} as lowering the energy due to the interaction of each electron with its exchange hole.

The remaining portion of E_{XC}, correlation, consists of all other many-body interaction terms. However, since exchange describes interactions of electrons with like spins, the largest component of the correlation term comes from interactions of electrons with opposite spins. Unlike exchange, there is no simple solution for the correlation contribution to the energy. A complete description of correlation is beyond the scope of this dissertation. However, useful insight into the nature of correlation is provided by looking at the progression from the Hartree energy to the exchange energy. Mathematically, this can be described as an expansion, where the next higher order term is the largest contributor to the correlation energy [73]. The solution for this term has been found to depend only on interactions between electrons that are closer together than some cutoff distance [74]. This cutoff distance provides the physical interpretation, since it corresponds to the distance for which disturbances in the potential of a uniform gas are screened from the surroundings [6, 56].

Correlation effects can be combined with those of exchange, and the resultant E_{XC}, as shown in equation 3.13, can be expressed in terms of the electron interaction with an exchange-correlation hole density, n_{XC}, in a manner similar to that shown in equation 3.12. The details of the coupling-constant averaged exchange-correlation hole, $\bar{n}_{XC}(\mathbf{r}, \mathbf{r}')$ can be found in references [6] and [75]. For this discussion, two properties of the n_{XC} are important. First, the n_{XC} obeys the same sum rule as the n_{ex}, which means that the effect of correlation is to re-distribute the density in the hole. Second, the calculation of the E_{XC} relies on the spherical average of the n_{XC}. Both of these properties play essential roles in making good approximations to the E_{XC}, as will be shown in detail below.

$$E_{XC}[n] = e^2 \int n(\mathbf{r}) \epsilon_{XC}([n], \mathbf{r}) \, \mathrm{d}\mathbf{r} = e^2 \int n(\mathbf{r}) \int \frac{\bar{n}_{XC}(\mathbf{r}, \mathbf{r}')}{|\mathbf{r} - \mathbf{r}'|} \, \mathrm{d}\mathbf{r}' \mathrm{d}\mathbf{r} \tag{3.13}$$

From the physical explanations of the exchange and correlation terms, it is apparent that the effects of exchange and correlation on a given electron are due only to other electrons in the immediate vicinity of the first. This arises because both the Pauli exclusion principle, and electron screening are short-range effects. Therefore, the problem of approximating the E_{XC} is simplified into determining a good approximation to the local density around each electron. The approach of transforming a complex problem into a solvable one is used once again by approximating the local exchange-correlation hole energy density, $\epsilon_{XC}([n], \mathbf{r})$, as the same as that of the homogenous electron gas with the given density found at each point $\mathbf{r}$. This is referred to as the Local Density Approximation (LDA). In the LDA, the exchange energy is calculated analytically and the correlation energy is found using Monte Carlo techniques, which results in calculated physical properties that are in unexpectedly good agreement with those found experimentally [76].

This agreement is unexpected since the electron density in solids and molecules is generally close to the superposition of atomic densities, and thus far from the uniform density of the homogeneous electron gas and, therefore, the LDA. Additionally, the LDA results in an incomplete cancelation of the previously mentioned unphysical self-interaction term [6]. Therefore, large spurious self-interaction terms will remain, and when combined with the non-uniformity of the density, suggest that the LDA should not work very well. However, since the LDA does predict physical properties that are in very good agreement with experiment, the question arises as to why the LDA works as well as it does. The answer rests in the mathematics used to determine the E_{XC}. As seen in equation 3.13, determining E_{XC} depends on the spherical average of $\epsilon_{XC}([n], \mathbf{r})$, so the detailed shape need not be precisely correct. More importantly, since the use of the density of the homogenous electron gas gives the exact exchange-correlation hole for some Hamiltonian (even though it's not the correct one), the sum rules for the n_{XC} are rigorously obeyed, which is an otherwise difficult condition to satisfy. As a result, even though the assumptions made in the LDA do not take into account the non-uniformity of the local density, the calculated properties compare well with experiment. Moreover, the disagreements between calculated and experimental properties are systematic. Specifically, the binding energies are typically overestimated, and the corresponding bond lengths are found to be too short [76]. Furthermore, lattice constants are typically found to differ from experimental values by -1% to 1% and the bulk modulus can be overestimated by up to 30% [77]. These systematic deviations are a result of the incomplete cancelation of the self-interaction terms. However, since the small deviations from experimental values are systematic, the use of the LDA allows for a reasonable prediction of experimental properties, which is one of the goals of DFT.

Since the density around each electron is not uniform, a possible improvement to the LDA is to conduct a gradient expansion of the density, as originally suggested by

Kohn and Sham [70]. However, this approach does not lead to an improvement over the LDA, even though it does seem physically sensible, since the resulting approximation for the n_{XC} violates the sum rules [6]. Additionally, since the n_{XC} in many real materials have large gradients, a simple expansion breaks down. These problems can be remedied by modifying the gradient expansion at large gradients such that both the use of an expansion is justified and the sum rules are enforced. This results in a so-called Generalized Gradient Approximation (GGA) for the E_{XC}, and unlike the LDA, there are numerous ways to construct GGA functionals [78].

GGA functionals fall into two main categories, which are classified by whether or not experimental data is used in the development of the approximation and, typically, the field of study of the researcher. One way to develop a GGA is to produce a reasonable form and then fit some adjustable parameters to experimental data. For example, the Becke-Lee-Yang-Parr (BLYP) and B3LYP functionals incorporate data from up to 407 experimental systems [79], and they are widely used in the chemistry community due to the high accuracy of their predictions for many systems. On the other hand, the physics community typically takes a different approach, and develops GGA functionals by building on the LDA and incorporating exact physical or mathematical constraints in the hope that the description of the system is improved. Some examples of widely used GGA's produced in this way are those of Perdew-Burke-Ernzerhof (PBE) [80], Becke (B88) [81], and Perdew-Wang (PW-91) [82]. Specifically, my calculations use the PW-91 GGA functional form, which is the default GGA functional form used by VASP [9]. Regardless of the approach used in the development of a given GGA functional, many material properties calculated using this method show an improvement over those found using LDA and are in good agreement both amongst themselves and with experimental values [6, 76]. Additionally, the small errors that do exist, when compared to experiment, are once again systematic. Specifically, the tendency for over-binding is reduced by the use of GGA functionals, so much so some-

times, that bond lengths are often slightly overestimated. Moreover, lattice constants are found to be within 0% to 3% (comparable to the range for LDA calculations) and the bulk modulus is between -10% to 10% (an improvement over LDA results) of the experimental values [77].

3.4 Solving the Kohn-Sham Schrödinger-like Equation

At this point, the unsolvable many-body problem has been successfully mapped onto an effective non-interacting problem, and a good approximation for the many-body interaction terms that constitute E_{XC} has been made. Therefore, what remains is the solution of the Kohn-Sham Schrödinger-like equations, shown in equation 3.7. While there are multiple methods available [6] to go about the task of solving these equations, one of the most natural methods, both mathematically and physically (when the focus of study is on materials in a periodic crystal structure) involves the use of a plane-wave basis set.

$$\psi_j(\mathbf{r}) = e^{i\mathbf{k}\cdot\mathbf{r}} u_j(\mathbf{r}) \tag{3.14}$$

$$u_j(\mathbf{r}) = \sum_{\mathbf{G}} c_{j,\mathbf{G}} e^{i\mathbf{G}\cdot\mathbf{r}} \tag{3.15}$$

$$\psi_j(\mathbf{r}) = \sum_{\mathbf{G}} c_{j,\mathbf{k}+\mathbf{G}} e^{i(\mathbf{k}+\mathbf{G})\cdot\mathbf{r}} \tag{3.16}$$

In this case, the periodicity of the system is essential, since Bloch's theorem [56] can then be applied to the Kohn-Sham wave functions. Bloch's theorem states that each single-particle electronic wave function, in a periodic solid, can be written as the product of a wave-like part and a periodic function, $u_i(\mathbf{r})$, as shown in equation 3.14. Since the periodic function can then be expanded using a discrete set of plane

waves with wave vectors corresponding to the reciprocal lattice vectors of the crystal, $\mathbf{G}$, as shown in equation 3.15, the electronic wave functions can be expressed as a sum of plane waves, equation 3.16. The problem has now been changed from one that required calculating an infinite number of electronic wave functions to one where only a finite number of wave functions exist at an infinite number of k points, since only a finite number of electronic states (bands) are occupied at each k point. At first glance, it appears that no significant improvement has been achieved, since calculations must still be performed at an infinite number of k-points. However, the electronic wave functions at k-points that are very close together will be almost identical, which means that the electronic wave functions over a region of space can be represented by those at a single k-point.

Several methods have been devised for obtaining special sets of k-points such that calculations performed at a small finite number of k-points give accurate approximations for the electronic potential and total energy of the system [83]. Specifically, my calculations make use of the method proposed by Monkhorst and Pack [84]. In this method, a k-point grid is generated, which, when combined with the symmetry present in the TiO_2 (110) surface, requires calculations at a minimal number of points in order to generate a good representation of the Brillouin zone. In general, care must be taken to ensure that the calculated total energy is converged with respect to the number of k-points used in the calculation, as specified by the dimensions of the grid. Moreover, metals typically require the use of a denser k-point grid than insulators due to the presence of a Fermi surface [9, 83]. As a result, if for example, a defect is introduced into an insulating system, the system may become conducting and require the inclusion of additional k-points to obtain results of comparable precision.

One problem still remains, since in principle, an infinite plane-wave basis set is still required to expand the electronic wave functions at each k-point. However, the coefficients, $c_{j,\mathbf{G}}$, for plane waves with small wave vectors are typically more important

[83]. This arises since a plane wave with a large wave vector has a smaller wavelength and thus more rapid oscillations. Therefore, plane waves with a larger wave vector, $\mathbf{G}$, contribute to higher-resolution features. In general, the wavefunctions of the system are relatively smooth, so not a lot of spatial resolution is needed. Therefore, a cutoff can be set at some given wave vector, $\mathbf{G}_{cut}$ where if a higher resolution is needed, the cutoff is increased. As seen in equation 3.17, the kinetic energy (T) at a given k-point depends on the reciprocal lattice vector. By tradition, the cutoff energy corresponding to $\mathbf{G}_{cut}$ is reported instead of $\mathbf{G}_{cut}$. As a result, coefficients for large $\mathbf{G}$'s are negligible, and the sums in equations 3.15 and 3.16 can be truncated. Once again, care must be taken to ensure that the total energy is converged when a given plane-wave cutoff energy is implemented.

$$T = \frac{\hbar^2}{2m_e}|\mathbf{k} + \mathbf{G}|^2 \tag{3.17}$$

Therefore, when a plane wave basis set is chosen, and the transformation to reciprocal space is made, the Kohn-Sham equations take the relatively simple form shown in equation 3.18. In this form, the kinetic energy terms are diagonal, and the effective potential is the sum of the Fourier transforms of the external, Hartree, and exchange-correlation potentials discussed previously. These equations are then solved by diagonalizing the Hamiltonian matrix, shown in brackets in equation 3.18, where the size of the matrix is determined by the cutoff energy. Computationally, iterative matrix diagonalization methods based on conjugant gradient [85, 86], block Davidson [87], and residual minimization [88, 89] schemes are used to solve equation 3.18.

$$\sum_{\mathbf{G'}}[\frac{\hbar^2}{2m_e}|\mathbf{k} + \mathbf{G}|^2\delta_{\mathbf{G}\mathbf{G}'} + V_{ext}(\mathbf{G} - \mathbf{G}')]c_{i,\mathbf{k}+\mathbf{G}'} = \varepsilon_i c_{i,\mathbf{k}+\mathbf{G}} \tag{3.18}$$

However, the plane-wave cutoff and hence the size of the Hamiltonian matrix is too large for efficient calculations if all of the electrons in the crystal are included directly. This occurs due to the fact that a large number of plane waves are needed to describe the tightly bound core (inner) electrons as well as the rapid oscillations of the valence (outer) electrons in the core region due to orthogonalizing to core electrons. The solution to this problem rests upon the knowledge that the majority of physical properties of solids depend to a much greater extent on the valence electrons than on those in the core. This occurs because the valence electrons screen those in the core, leaving them largely inert to their physical environment. Therefore, the core electrons and the strong ionic potential can be replaced by a weaker pseudopotential. The overall goal of this pseudopotential approximation is to generate a smooth, weak pseudopotential that results in calculated physical properties that are essentially identical to those found in the all electron case, but require significantly fewer plane waves and therefore a much smaller cutoff energy.

As shown previously, E_{XC} is a function of the electron density. Therefore, in order to model E_{XC} accurately, it is necessary that the pseudo and real wave functions be identical in both absolute magnitude and spatial dependence outside of the core region. This ensures that the first-order energy dependence of the scattering from the ion-core is correct, so that scattering is accurately described over a wide range of energy, which is a physical requirement for the pseudopotential approximation to be accurate for a wide variety of environments. These types of pseudopotentials are termed norm-conserving, and are transferable from one system to another [6, 83]. However, this high degree of accuracy typically results in some sacrifice of smoothness, which is directly related to the number of plane waves required in the calculation.

Another approach, ultrasoft pseudopotentials, allows for accurate calculations by expressing the wave functions in terms of a smooth function and an auxiliary function around each ion core [17, 18]. However, this transformation requires the relax-

ation of the norm-conservation condition for the smooth function, which results in both advantages and disadvantages [6]. The main disadvantage is that the loss of norm-conservation results in a more complicated generalized eigenvalue problem, but fortunately this is not a major complication with the use of the iterative methods mentioned previously. On the other hand, a significant advantage is that the ultrasoft pseudopotential method leads to smoother potential and wavefunctions, so that a much lower cutoff energy is needed. This results in a more efficient use of computational time for comparable sized calculations and the ability to study larger systems than realistically possible with the use of norm-conserving pseudopotentials.

My calculations were performed with ultrasoft pseudopotentials as supplied in Vienna Ab-initio Simulation Package (VASP) [7–9] for calculations that use a GGA for the E_{XC}. Specifically, I used the standard pseudopotential [9] for C (O), where the core contains the $1s^2$ electrons, leaving the 4 (6) 2s and 2p electrons as valence. For Ti, I used the pseudopotential that treats the 10 3p, 4s, and 3d electrons as valence. Since the 6 semi-core 3p electrons are not sufficiently screened, they participate in bonding, and therefore must be included in the valence manifold. The only remaining pseudopotential used in my calculations is for Cu, where only a single version is available for use. The O atom has the highest cutoff energy of the atoms used in my calculations, 396eV. Use of this cutoff energy in my initial calculations gave accurate results (while using significantly less computational resources) that are comparable to those found using norm-conserved pseudopotentials, which require a higher cutoff energy of 680 eV. As a result, unless otherwise specified, my calculations used the ultrasoft pseudopotentials mentioned above, and only included plane waves up to a cutoff energy of 396 eV. Having chosen a plane-wave basis with a cutoff energy of 396 eV, the matrix eigenvalue problem shown in equation 3.18 is then solved using an iterative matrix diagonalization algorithm [85–89]. This procedure is repeated for each

symmetry-independent k-point on the Monkhorst-Pack [84] grid, where the specific size of the grid varies from project to project, and is specified in later chapters.

3.5 Computational Details

All of my DFT calculations were performed using the Vienna Ab-initio Simulation Package (VASP) [7–9], which is a commercial code designed to perform fast, efficient, and accurate calculations in first-principles modeling of materials. In addition to the specifications described in the previous section, there remain numerous flags that can be specified by the user in order to focus on the desired properties of the system being studied. In general, recommended default settings exist for these flags, as described in reference [9]. As a result, I will limit my discussion below to the changes I made to tailor the runs to study the (110) surface of TiO_2.

The Precision (PREC) tag specifies the three computational parameters listed in table 3.1, and there are five possible settings for this tag. However, I only made use of three settings, Normal, Accurate, and High, and will therefore focus my discussion on the differences among these three. The first computational parameter is the cutoff energy, which as discussed earlier, has a recommended value of 396 eV for the set of pseudopotentials used in my research. Both the Normal and Accurate settings use this value, whereas the High setting uses a value 1.3 times larger. In general, it is only important to have a larger E_{cut}, and correspondingly larger plane wave basis set, if the cell volume is allowed to change during the calculations, as discussed in the following chapter.

The next parameter effected by the PREC tag involves the Fast Fourier Transform (FFT) grid size. As discussed in the previous section, the Kohn-Sham equations are solved in reciprocal space. However, E_{XC} is most naturally calculated in real space. Therefore, frequent Fourier transformations between real and reciprocal space are required throughout the calculation. The fast Fourier transform algorithm [90],

Table 3.1: Details of PREC setting in VASP are specified for the specific values used in my calculations. Explanations of the parameters are given in the text.

Parameter	Normal	Accurate	High
E_{cut}	1 × max	1 × max	1.3 × max
FFT grids	$\frac{3}{4}$	1	1
Real Space projection points	1000	1000	1500

adapted to three dimensions, greatly facilitates this procedure computationally. These FFT's are done on a grid whose size depends on the number of reciprocal space lattice vectors. If the FFT grid that is used in the calculation does not contain all required (as determined by the cutoff energy) reciprocal space lattice vectors, then so-called wrap-around errors occur. In general, small reductions in the FFT grid result in faster calculations at the cost of computational precision that may or may not be significant, depending on the other approximations in use. Setting the PREC tag to Accurate and High results in an FFT grid that avoids wrap-around errors, whereas Normal uses a smaller grid, thus introducing a small error into the calculation.

The remaining difference concerns the use of real-space projection operators, which is governed by the LREAL tag. Determining the non-local portion of the pseudopotential requires evaluation of a projected wave function, and this projection can either be performed in real or reciprocal space. While it is more precise to perform the projections in reciprocal space, it can also considerably increase the computational time, especially for larger systems, since this evaluation scales with the number of plane waves. When performed in real space, the projections are confined to spheres around each atom, which are discretized into a grid containing a certain number of points specified by the PREC setting, as seen in table 3.1. Since the radius of these spheres

does not change as the system size increases, using real-space projection operators is much more computationally efficient, and is recommended for calculations containing more than 20 atoms [9]. Even though using real-space projection operators always results in a small (and not necessarily negligible) error, the error is usually a constant for each atom. Therefore, if one is only interested in energy differences, it may be possible to obtain the same answer (within the precision error resulting from other approximations) in less time by using real-space projection operators.

The iterative process of solving the Kohn-Sham equations, as described previously, results in a single total energy calculation. It is then possible to determine the force acting on each atom and, using these forces, allow the atomic positions to relax to optimal values. The ISIF tag specifies two things related to structural optimization. One is whether or not the stress tensor is calculated, a relatively time consuming process. It also determines which degrees of freedom, such as individual atom positions and cell volume, are allowed to change. Unless otherwise specified, I have set the ISIF tag such that the cell volume and shape remain constant and the positions of certain ions (those not specified as fixed) are allowed to relax into their lowest energy configuration, within the constraints of the system symmetries. The specific algorithm used to find the lowest energy configuration can be specified by the IBRION tag. In my calculations, I used both quasi-Newton [89] and conjugate-gradient [85, 86] algorithms to relax ionic positions. While the quasi-Newton method required fewer steps if the initial configuration was close to the minimum, the conjugate gradient method is guaranteed (assuming the energy surface has a quadratic form) to find the minimum in a set number (total number of ionic degrees of freedom) steps. I performed numerous calculations with each method, and found no noticeable difference in the final configurations obtained, and as a result, I made use of both methods, as appropriate to the individual circumstances.

Table 3.2: Energy and atomic position differences are listed for the specified force tolerance. In each case, the difference is with respect to the most precise system calculated, where the atoms in their relaxed configuration experience forces less than 0.01 eV per Å. Calculations were performed on a five trilayer, symmetric TiO_2 slab as described in later chapters.

Force Tol. (eV/Å)	Energy Difference (meV)	Atomic Position Difference (Å)
0.04	1.08	0.006
0.03	0.42	0.004
0.02	0.06	0.001

Regardless of the algorithm used to perform the ionic relaxations, a break condition must be set in the ionic relaxation loop to denote that the minimum energy configuration is obtained. This is done through the EDIFFG tag. The default setting for this tag considers a system to be relaxed if the change in total energy of the system between two consecutive atomic relaxation steps is less than some specified value, which is 1 meV by default. However, if a negative value is entered for this flag, the atomic relaxation is considered complete when the largest atomic force is smaller than the absolute value of the setting. For the (110) surface of TiO_2, the default energy stopping criterion corresponds to a force criterion of approximately 0.04 eV per Å. Tests for this and smaller force convergence criteria are summarized in table 3.2, where the change in energies and atomic positions are given with respect to those obtained for a force tolerance of 0.01 eV per Å. The position difference is the largest found for any of the 30 atoms in the system studied, and both the energy and position differences are comparable to other TiO_2 surface models that I used in my calculations. The results obtained for a force tolerance of 0.02 eV per Å, as listed in table 3.2, are converged well beyond the precision of my calculations, particularly for

larger systems. Additionally, this force tolerance is used for other comparable studies [11, 12], and as a result, all of my calculations set the EDIFFG tag to -0.02.

The final set of flags used involve the use of partial electron occupancies of bands. In general, each band can be occupied by two electrons of opposite spin, and for the ground state, the bands are filled, at each k-point, from the lowest energy level up until all electrons are used [56]. When this occurs, the energy of the highest occupied band is referred to as the Fermi energy. This provides an operational distinction between insulators (and semiconductors) and conductors, where insulators have filled bands at all k-points, and metals do not. Computationally, two aspects must be considered when performing calculations on systems that have partially filled bands.

First, the spin of the electron in the partially occupied band becomes important, thus requiring spin-polarized calculations. This is done in VASP using the ISPIN tag. TiO_2 is known to be a semiconductor, and computations of this material result in fully occupied bands. As a result both spin polarized and non-spin polarized calculations for the stoichiometric, bare surface are identical within computational errors. Since accounting for the electron spin doubles the number of electrons bands that must be considered, spin-polarized calculations take significantly longer. Therefore, all of my computations on both the bulk crystal structure of TiO_2 and the stoichiometric, bare surface of TiO_2 were not spin-polarized. When the surface is non-stoichiometric, or adsorbates are added, the bands might not remain filled, and thus all calculations for these cases were spin-polarized.

A second problem arises when attempting to evaluate the integral over the filled parts of the bands, as required to determine the energy of the system. Computationally, this integral must be evaluated using a sum over the discrete set of k-points specified by the user. At the Fermi level, the electron occupancies jump from one to zero, which is accounted for with a step function in the summation. This makes the summation converge very slowly with respect to k-point sampling unless the band

is completely filled, which results in the need for a much larger number of k-points for conductors than for insulators and semiconductors [9]. However, much faster convergence with respect to k-point sampling can be obtained without sacrificing the accuracy of the summation by replacing the step function with some smooth function. Physically this equates to allowing part of an electron to be in one band and the remainder in another band, i.e. partial electron occupancy or "electron smearing". While unphysical, this procedure is both possible and practical computationally.

Several methods have been proposed to solve this problem, and I made use of two of them, Gaussian smearing [9] and Methfessel-Paxton smearing [91], where the choice is governed by the ISMEAR tag. In general, the Gaussian scheme is recommended for insulators (and semiconductors) with large unit cells, whereas the Methfessel-Paxton [91] scheme is strongly encouraged for metals. Both cases require designating an allowed smearing width in eV, which is controlled by the SIGMA tag. The default value of SIGMA is 0.2 eV, and all of my spin polarized calculations were done with this smearing width. Since the relevant calculations in my research focused on the addition of metal atoms or defects to the surface, I had no way of knowing whether the system would remain a semiconductor or become a conductor. Thus it was not always clear which value of ISMEAR to use. The results of extensive testing showed that there was no difference (within the accuracy of my other approximations) between calculations performed with either method mentioned above. Therefore, since much of my work involves adding a metal, Cu, to the TiO_2 surface, I chose to use the Methfessel-Paxton [91] smearing scheme for the majority of my calculations.

Chapter 4

The Structure of TiO_2

4.1 Properties of the Bulk Rutile Structure

Initially, attention was placed on computing the bulk structural properties of TiO_2 in the rutile crystal structure. The structure is named "rutile" after the name of the mineral TiO_2 in the phase that has this crystal structure. Additionally, numerous other compounds of the form MO_2 (where M is a metal) have rutile structure. The properties of rutile TiO_2 are both experimentally known and have been precisely and accurately calculated using *ab-initio* methods. Even though new information was not gleaned from my calculations of the bulk structural properties, they are an important step for building a surface slab model. Furthermore, they were carried out to ensure the correct implementation of the VASP code [7, 8].

The rutile crystal structure of TiO_2 can be obtained by infinite repetition in all directions of a primitive tetragonal [92] unit cell as shown in figure 4.1. Each primitive unit cell is defined by the lattice constants a and c. It contains two Ti atoms, positioned at $(0,0,0)$ and $(\frac{1}{2},\frac{1}{2},\frac{1}{2})$, as well as four O atoms positioned at $\pm(u,u,0)$ and $\pm(u+\frac{1}{2},u-\frac{1}{2},\frac{1}{2})$, where u is an internal coordinate, and all positions are specified in lattice coordinates. Physically, the system consists of nearest-neighbor Ti-O bonds, where each Ti atom is bonded to six O atoms forming a distorted octahedron with the Ti atom at the center, and each O is bonded to three Ti atoms. However, the six Ti-O bonds are not all the same length, and can be further subdivided into axial (L_a) and equatorial (L_e) bonds where the four equatorial bonds lie in the $[\bar{1}10]$ plane and the two axial bonds are perpendicular to this plane, as can be seen in figure 4.1. Therefore,

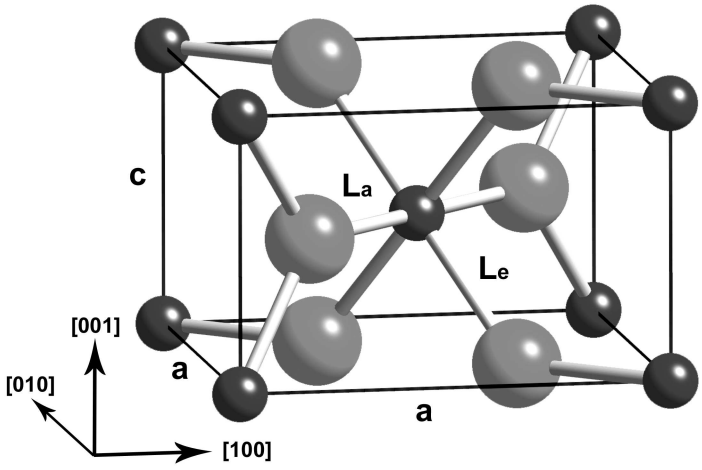

Figure 4.1: Primitive unit cell for bulk TiO_2 in the Rutile crystal structure. Ti (O) atoms are represented by small, dark (large, light) spheres. The lattice constants, a and c, as well as the axial (L_a) and equatorial (L_e) Ti-O bond lengths are labeled.

predicting the bulk structure amounts to the determination of 3 parameters, a, c, and u, which I found using two different approaches that are discussed below. For both cases, the calculations used a $4 \times 4 \times 6$ Monkhorst-Pack [84] k-point grid, for which the calculated energy difference between two distinct configurations is converged to within 0.2 meV. This level of precision is two orders of magnitude better than the expected accuracy of my calculations.

The first method used to obtain the bulk structure consisted of performing a large number of single total energy calculations for fixed structural parameters and using the data to interpolate the values of the lattice and internal parameters at the energy minimum. The specific procedure I followed was: (a) first transforming lattice constants a and c to unit cell volume, V, where $V = a^2c$, and dimensionless parameter, γ, where $\gamma = c/a$; (b) then conducting a series of calculations that minimized the internal parameter u with respect to the energy for fixed V and γ and then minimized

Table 4.1: Lattice parameters, bond lengths, and the bulk modulus for bulk TiO_2. The results of my calculations for two methods and three different computational approximations, as described in the text, are compared to and shown to be consistent with experimental data, as well as previously determined theoretical results. The volumes (V) are given per TiO_2 formula unit, and the remaining symbol definitions can be found in the text.

	Expt.	Previous Calculations		Present Calculation (GGA)			
Property	[19, 20]	LDA [21]	GGA [22]	Vγu	Normal	Acc. [32]	High
V (Å^3)	31.217	32.42	31.86	32.25	31.59	31.59	32.27
a (Å)	4.5936	4.653	4.641	4.643	4.611	4.611	4.652
c (Å)	2.9587	2.965	2.958	2.991	2.972	2.971	2.982
u	0.3048	0.305	0.305	0.303	0.304	0.304	0.305
γ	0.6441	0.637	0.637	0.644	0.644	0.644	0.641
L_a (Å)	1.9801	2.007	2.002	1.992	1.983	1.984	2.006
L_e (Å)	1.9485	1.961	1.956	1.976	1.960	1.959	1.968
B_o (GPa)	216	240	-	210	-	-	-

γ with respect to energy for each chosen volume; and (c) finally, minimizing the u- and γ-optimized values of V with respect to energy. Optimal values of γ and u at the energy minimizing volume were found by interpolation. Specifically, a total of 343 calculations where performed, where 7 values were chosen for each parameter. The data for each minimization were fitted using a third-order polynomial, where optimal values were then calculated at the energy minimum of the fitting function. The optimized parameters using this approach are shown in the column labeled $V\gamma u$ in table 4.1, and are in good agreement with both experiment [19, 20] and other theoretical calculations [21, 22]. Additionally, the data obtained in minimizing the volume with respect to energy allows for the calculation of the zero-pressure Bulk Modulus, B_o, for this structure, which as seen in table 4.1, is also found to be in good agreement with experiment [20].

All of the lattice parameters (but not the Bulk Modulus) can be obtained by allowing the built-in structural optimization feature of VASP [7, 8] to relax both the individual atomic positions as well as the unit cell size and shape. In this case, the optimal cell volume and shape are determined from relaxations based upon the calculated stress tensor. A potential problem arises since the number of plane waves in the basis set depends on the cutoff energy and cell volume. Therefore, in order to give the same computational precision, an increase in cell volume would require the inclusion of additional plane waves into the basis set. Since the number of plane waves does not change between atomic iterations, a small error, called the 'Pulay Stress' [9] (after the researcher who first identified the effect), occurs in the diagonal components of the stress tensor. However, if the energy cutoff is initially larger than what is required for a given precision, then the basis set will contain enough plane waves such that small increases in the volume of the unit cell will not effect the precision of the calculation. As a result, for this automated method, an increased cutoff energy must be used in order to correctly determine the optimal cell size and shape. This problem is avoided in the $V\gamma u$ method described above, but at significant computational cost, a large number of single total energy calculations.

As shown in table 4.1, I calculated the optimized parameters using the automated method under precision (PREC) settings of 'Normal', 'Accurate', and 'High' [9], which have increasingly larger basis sets, respectively. As expected, the calculations done with the largest plane wave basis set, 'High', both took the longest amount of time and gave answers that are close to those from the $V\gamma u$ method. It is also clear from table 4.1 that the calculated results are very close to the experimental values regardless of the precision setting used. The time required for these calculations is relatively small; however, as I expand the size of the unit cell for calculations involving the surface, the large number of plane waves used for the 'High' setting results in the calculations becoming computationally prohibitive. Therefore, in order to maintain consistency

in comparative calculations when proceeding to model the (110) surface, I used the structural parameters obtained under the 'Accurate' settings.

4.2 The Role of Symmetry

Both methods of calculating the lattice parameters discussed in the previous section use the tetragonal symmetry of the system [92]. However, construction of the structural model for the (110) surface requires the use of a non-primitive unit cell, as shown in figure 4.2, that does not possess these symmetries. This non-primitive unit cell has twice the number of atoms as the primitive unit cell and is of orthorhombic symmetry [92]. The lattice parameters of this non-primitive cell (labeled in figure 4.2) are related to those of the primitive cell (labeled in figure 4.1) by the multiplication of a constant. If the calculations were done for the full continuum of k-points in the Brillouin zone, the calculated values of a, c, and u would be independent of the unit cell that is used. However, since I only calculate the energy bands of the electrons for a discrete k-point set, there arises a small but finite difference in the lattice parameters calculated using the two different unit cells.

The a, c, and u values that correspond to the lattice parameters of this non-primitive unit cell are compared with the primitive unit cell lattice parameters, calculated with the 'Accurate' setting, and experimental values [19, 93] in table 4.2. The most significant difference is that the calculated bulk structure no-longer maintains all of the tetragonal symmetry operators of the rutile crystal structure. Specifically, the lengths of the unit-cell edges in the [110] and [$\bar{1}$10] directions are no longer rigorously the same, such that three distinct lattice constants are now required. As a result, when the non-primitive unit cell is used, two different values are obtained for a, as shown in table 4.2. Additionally, two internal coordinates are now needed to determine the positions of the O atoms, which results in multiple u values for the

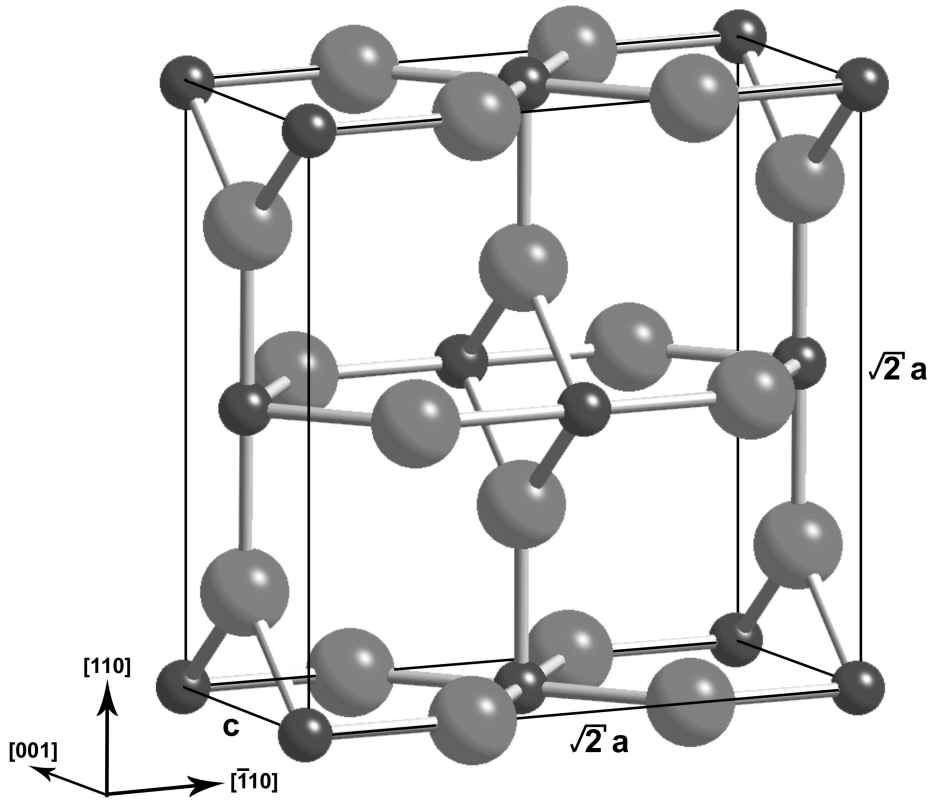

Figure 4.2: Non-primitive unit cell for bulk TiO_2 that has the same symmetry as the cell used to model the (110) surface. Ti (O) atoms are represented by small, dark (large, light) spheres. The lattice constants, as they relate to those of the primitive unit cell, are labeled.

Table 4.2: Comparison of lattice parameters and energies for unit cells that possess different symmetry. Specifically, results are shown for the primitive unit cell, and the non-primitive unit cell that has the same symmetry as the unit cell used to model the (110) surface. The cohesive energy (E) is given per TiO_2 formula unit, and other listed properties are explained in the text.

Property	Expt.[19, 93]	Primitive Unit Cell	Non-Primitive Unit Cell
a (Å)	4.5936	4.6114	4.6122 [$\bar{1}$10] 4.6125 [110]
c (Å)	2.9587	2.9715	2.9691
u	0.3048	0.3042	0.3039 0.3040
E (eV)	19.9	20.8671	20.8669

non-primitive unit cell in table 4.2. The largest observed difference between calculations using the primitive and non-primitive unit cells is 2.4 mÅ in the c parameter, which is an order of magnitude less than the accuracy, and of comparable order to the precision, in my calculations. Therefore, based only on the calculated values for the lattice parameters, there would be no need to factor the effects of the loss of symmetry that occurs when constructing the (110) surface structure into my model.

Table 4.2 also shows that the cohesive energy per TiO_2 formula unit, calculated using the two unit cells, differs by 0.2 meV, which is comparable to the precision of my calculations. Additionally, this difference is much smaller than the expected accuracy of the calculations, which is on the order 10 meV [9]. However, many computational studies involving the (110) surface of TiO_2 require structural models containing 50 or more TiO_2 formula units. Therefore, for these larger surface studies, the differences in cohesive energies between the two types of unit cells would be of the same order of magnitude as the expected accuracy. As a result, in order to avoid this systematic

error, I used the lattice parameters obtained from the non-primitive unit cell for all future calculations.

While the use of the lattice parameters from the non-primitive unit cell is a correct and precise choice, I would neither recommend that others take this additional step nor do so myself when performing similar calculations in the future. As explained above, the errors introduced into the energies can become significant for very large unit cells. However, as seen in later chapters and the references within, typical calculations focus on determining binding energies of an adsorbate or defect formation energies, which are both found by calculating energy differences. When calculating these energy differences, the systematic errors introduced by the differences in symmetry between the unit cells will cancel. Therefore, the accuracy of these calculations remains the same, within the precision of the calculation, whether or not the extra steps are taken to incorporate the effects caused by the imposition of different symmetries. However, this is only true as long as the k-point sets over which all of the calculations are performed remain well converged.

Chapter 5

Modeling the Stoichiometric Surface

5.1 Slab Approximation

The theoretical framework of the DFT calculations, as discussed in detail in Chapter 3, requires 3-D periodicity. So in order to model a 2-D surface, a slab approximation is used. Specifically, to model the stoichiometric (110) surface, I constructed a surface unit cell with dimensions of 2.97 Å in the [001] direction and 6.52 Å in the [$\bar{1}$10] direction. In the [110] direction, a slab of Ti and O atoms in the rutile crystal structure are surrounded above and below with vacuum. Therefore infinite repetition in all directions gives an infinite sequence of slabs which maintains the required 3-D periodicity. A ball and stick model of a surface unit cell that generates a four-trilayer-thick slab is shown in figure 5.1, where the labels of specific atoms and bonds will be referred to and discussed in detail in the following sections. A trilayer is so named since it contains atoms that lie in three distinct planes. For the surface unit cell shown in figure 5.1, the top (surface) trilayer consists of a central plane containing two Ti (I and II) and two O (2 and 2^*) atoms, surrounded by two planes, each containing one bridging O atom, above (1) and below (3) the central plane.

As in the bulk structure models, care must be taken to ensure converged sampling of the Brillouin zone. For an orthorhombic unit cell, such as the one used to generate the slab model of TiO_2 (110), the cell lengths in reciprocal space are proportional to the inverse of the cell lengths in real space [56]. Therefore, in order to maintain uniform sampling I sampled twice as many points in the Brillouin zone for the [001] direction in relation to the [$\bar{1}$10] direction since the cell edge parallel to [001] is half as

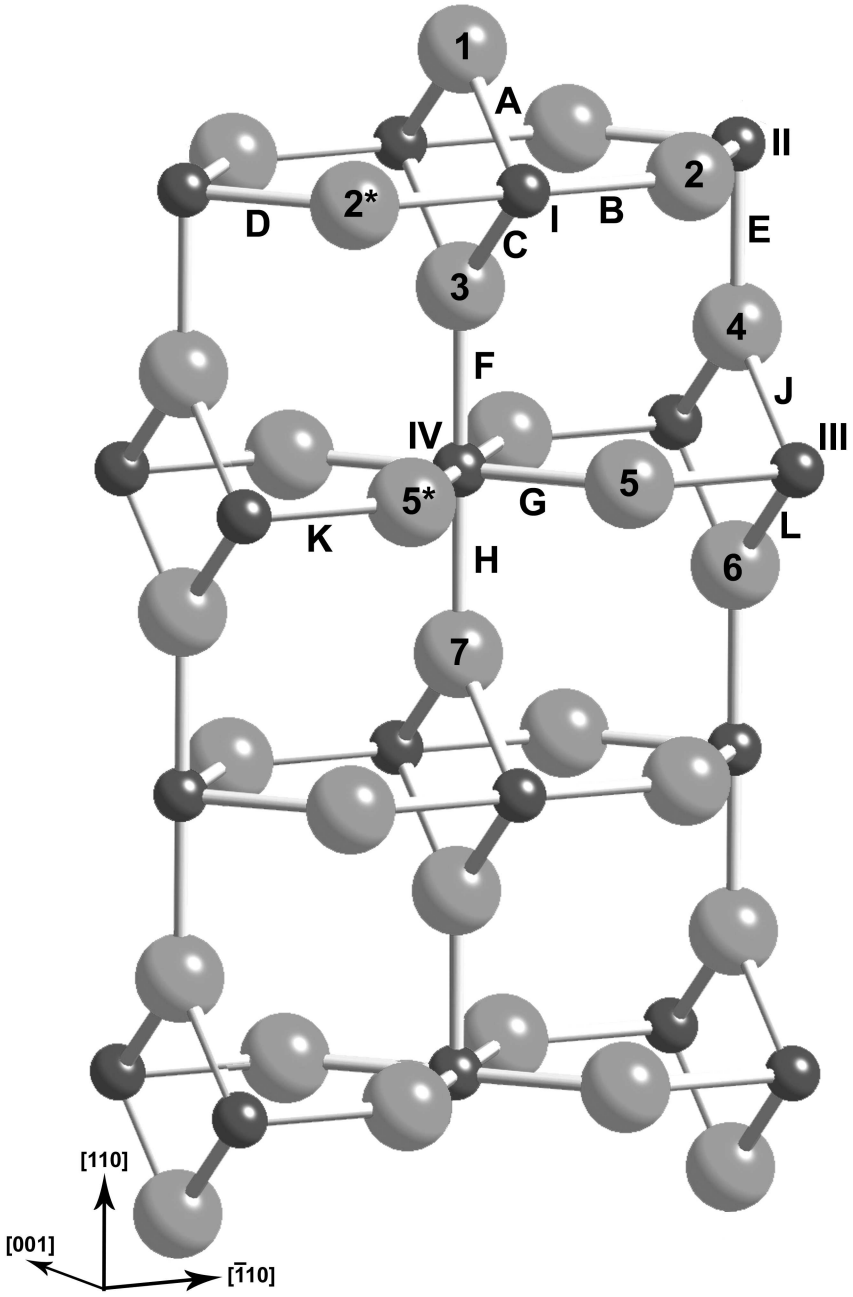

Figure 5.1: Model of the TiO_2 (110) surface unit cell containing 4 trilayers. Ti (O) atoms are represented by small, dark (large, light) spheres. Arabic and Roman numerals label specific O and Ti atoms respectively where an * denotes atoms that are paired via symmetry. Bonds are labeled by the letters A through L where I is omitted.

long as that parallel to [$\bar{1}$10]. The cell length in the [110] direction consists of the slab width plus the vacuum width and is significantly larger than the other dimensions. Therefore, the Brillouin zone width in the [110] direction is much shorter than other directions, and many fewer k-points need to be sampled in this direction to achieve uniform Brillouin zone sampling. Specifically, I sampled two points in the Brillouin zone along the [110] direction. For the stoichiometric surface with both the slab fixed at three trilayers and the vacuum thickness fixed at the length equivalent of three trilayers, I determined that a $2 \times 4 \times 2$ Monkhorst-Pack [84] k-point set was sufficient. This k-point set results in the convergence of the relaxation energy of the slab from bulk-like atomic position to optimal positions to within 0.01 eV.

In addition to k-point sampling, care must also be taken when using a slab approximation to ensure that two adjacent slabs of atoms are not appreciably interacting with each other. This involves increasing the vacuum thickness until important quantities converge. Moreover, since I plan to add additional atoms, such as Cu, CO, and O_2, I need to have sufficient vacuum width so that the added atoms will only interact with the slab surface they are placed on. Using the converged k-point set found previously and a symmetric slab containing three trilayers, I studied the effects of changing the vacuum thickness between slabs from the equivalent of 1 to 12 trilayers which corresponds to a thickness of 3.26 Å to 39.14 Å. Once again, I investigated the convergence of slab relaxation energy and found that a vacuum thickness of four trilayers (13.05 Å) results in a converged value to within 0.002 eV. In order to ensure that this amount of empty space always exists between slabs when additional atoms and molecules are added to the surface, I chose a vacuum thickness of 19.57 Å, which corresponds to six trilayers, in all of my future surface calculations.

The final convergence criterion that must be satisfied in order to use the slab approximation is the thickness of the slab itself. My initial investigations focused on the study of slabs that had a mirror plane through the center of the slab. This type of

model results in two surfaces for each slab, with bulk-like atoms in the center. For this case, I need to ensure not only that the atoms near the surface correctly model the experimentally determined surface structure, but also that the atoms in the center of the slab approach the correct bulk-like structure. As discussed in the next section, finding a converged slab thickness that contains a small enough number of trilayers to make later studies with larger in-plane surface unit cells computationally tractable is a complex problem in and of itself.

5.2 Slab Thickness

One way to ensure that the slab thickness is converged is by determining the surface energy. As shown in equation 5.1, the surface energy is calculated by subtracting the energy of the bulk structure from the slab energy. The bulk structure energy is found by multiplying the energy per TiO_2 formula unit for the bulk structure, E_{Bulk}, by the number of trilayers in the slab, N, and the number of formula units per trilayer, 2. The actual surface energy is then one half of this difference, since the model contains two surfaces, one on each side of the slab.

$$E_{Surface} = \frac{1}{2}(E_{Slab} - 2NE_{Bulk}) \tag{5.1}$$

Using the k-point set and vacuum thickness previously determined, I calculated the surface energy for slabs containing 3 to 15 trilayers. I only considered slabs with an odd number of trilayers in order to avoid so-called odd-even oscillations [35] and to maintain the mirror symmetry along the center plane of the slab such that computational efficiency was maintained. These data are plotted in figure 5.2, which also shows results from two other sets of calculations [10, 35]. My calculations are in good agreement with the previous calculations, as well as the experimentally determined surface energy, which was measured to be approximately 0.57 eV [94]. Additionally, I

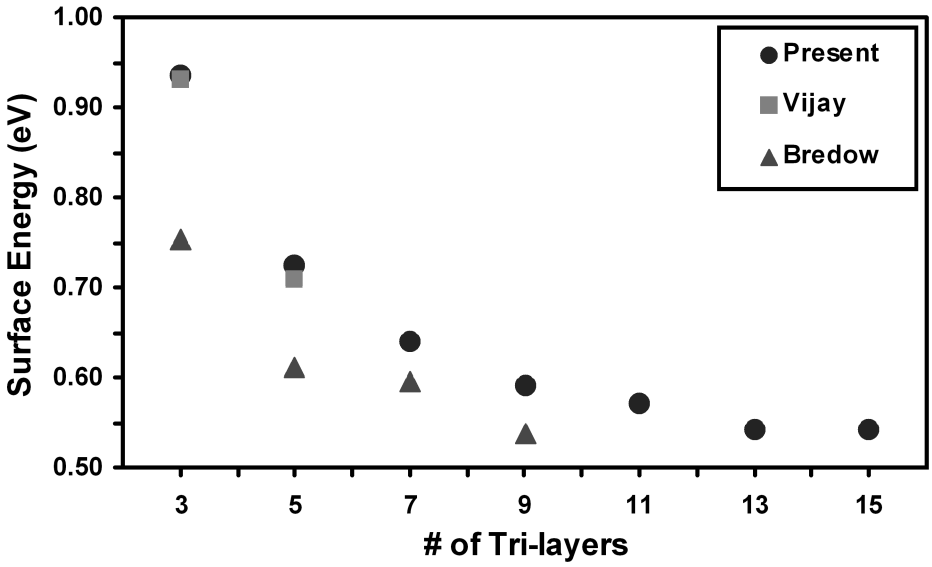

Figure 5.2: Surface energy vs. slab thickness as measured in trilayers. Results shown include my calculations [32], those of Vijay [10] carried out with the same method, and those of Bredow [35] performed with a somewhat different method.

observed that the surface energy does not converge to within my previously obtained precision of 0.01 eV until a 13-trilayer slab is used, which is also in good agreement with previous results [35]. Therefore, in order to maintain a precision in surface energy on the order of hundredths of an eV, calculations would need to be performed on a 13-trilayer slab, which means that the unit cell for each slab would have 78 atoms. As a result, modeling surfaces containing isolated defects or adsorbates, which require at least four in-plane surface unit cells, would not be currently achievable within as acceptable amount of computational time. However, the convergence of surface energy is a very stringent convergence criterion. Other criteria exist that are both physically acceptable and more rapidly convergent with respect to slab thickness.

One approach is to compare the calculated relaxed atomic structure of the surface atoms with the experimentally determined structure. This is often done in both theoretical [13, 24–31] and experimental [23, 34, 95] papers specifying atomic positions in terms of their displacements away from their bulk-terminated positions. In accordance with the atom labels given in figure 5.1, atomic displacements have been determined for slabs with an odd number of trilayers with a thickness ranging from 3 to 15 trilayers. The results [32, 33] are reported in table 5.1, using atom labels as given in figure 5.1, along with a typical result from previous theoretical work [27] and three experimental studies [23, 34, 95].

Three important results are illustrated in table 5.1. On the one hand, focusing only on my calculated results, it is apparent that the atomic displacements of the atoms converge faster than the surface energy. Specifically, the displacements are converged to within a few hundredths of an Å for slabs with a thickness of nine trilayers. By contrast, surface energy does not converge until 13-trilayer slabs are used.

Secondly, the previously calculations reported in table 5.1 were done with a 7-trilayer slab [27]. However, when compared to my results for the same slab thickness, significant differences are apparent. In particular, the displacements for three atoms

Table 5.1: Atomic displacements of atoms from their bulk-terminated positions are given in Å, where the displacement is in the (110) direction unless otherwise noted. Results from the present study [32, 33] are labeled by the number of trilayers in the slab. Additional values are shown from 3 experiments [23, 34, 95] and a previous DFT calculation [27]. Atom labels are taken from figure 5.1, which also specifies the coordinate axis that provides positive and negative senses for the displacements. The column labeled 7* has been designed to match the previous theoretical results, as explained in the text.

Atom Label	Displacement from bulk positions (Å)											
	SXRD[23]	MEIS[95]	LEED[34]	Calc.[27]	3	5	7	7*	9	11	13	15
Ti(I)	0.12±0.05	0.19±0.07	0.25±0.03	0.23	0.17	0.29	0.33	0.20	0.42	0.43	0.43	0.44
Ti(II)	-0.16±0.05	-0.09±0.09	-0.19±0.03	-0.11	-0.11	-0.10	-0.07	-0.14	-0.03	-0.03	-0.02	-0.01
O(1)	-0.27±0.08	0.13±0.16	0.10±0.05	-0.02	0.00	0.09	0.13	-0.02	0.23	0.23	0.23	0.24
O(2)	0.05±0.05	0.05	0.27±0.08	0.18	0.20	0.24	0.27	0.16	0.32	.032	0.33	0.35
O(2) [$\bar{1}$10]	0.16±0.08	0.00	0.17±0.15	0.05	0.07	0.06	0.05	0.05	0.05	0.05	0.05	0.05
O(2*) [$\bar{1}$10]	-0.16±0.08	0.00	-0.17±0.15	-0.05	-0.07	-0.06	-0.05	-0.05	-0.05	-0.05	-0.05	-0.05
O(3)	0.05±0.08	0.10±0.13	0.06±0.10	0.03	-0.03	0.07	0.11	0.00	0.19	0.19	0.20	0.21
Ti(III)	-0.09±0.04	-0.09±0.09	-0.09±0.07	-0.06	-	-0.04	-0.03	-0.09	0.00	0.00	0.01	0.02
Ti(IV)	0.07±0.04	-0.06±0.06	0.14±0.05	0.12	-	0.17	0.23	0.09	0.32	0.32	0.33	0.34
O(4)	0.00±0.08	-	0.00±0.08	0.03	0.02	0.06	0.09	0.00	0.13	0.13	0.15	0.16
O(5)	0.02±0.06	-	0.06±0.12	0.00	-	0.06	0.09	-0.02	0.15	0.15	0.16	0.17
O(5) [$\bar{1}$10]	0.07±0.06	-	0.07±0.18	0.02	-	0.03	0.02	0.02	0.01	0.01	0.01	0.01
O(5*) [$\bar{1}$10]	-0.07±0.06	-	-0.07±0.18	-0.02	-	-0.03	-0.02	-0.02	-0.01	-0.01	-0.01	-0.01
O(6)	-0.09±0.08	-	0.00±0.17	0.03	-	0.03	0.07	0.00	0.10	0.11	0.12	0.13
O(7)	-0.12±0.07	-	0.01±0.13	0.00	-	0.02	0.04	0.00	0.10	0.09	0.11	0.12

differ by at least 0.1 Å, well outside the precision of my calculations. The largest displacement is for the bridging O atom, which differs by 0.15 Å. Additionally, many previous calculations found the bridging O atom to displace towards the bulk [13, 24–31], whereas my results show a definite displacement *away* from the bulk. The reason for the differences in atomic relaxation from the previous calculation [27] and those of the present study can be found from a careful investigation of the parameters used in the DFT calculations. Table 5.1 also shows that atomic displacements in the column labeled 7* agree within a few hundredths of an Å to those of the previous calculation. The 7* results were obtained by reducing the k-point set to a $2 \times 2 \times 2$ Monkhorst-Pack grid [84], using a pseudopotential that classifies the 3p electrons as part of the core manifold instead of the valence manifold, using real-space projection operators, and allowing for a small degree of FFT wrap-around, which occurs for the 'Normal' precision setting in VASP [9]. Each of these four changes corresponds to a worsening of the computational approximations in the calculations. Therefore, the results for the 7-trilayer slab from the previous and current calculations would not be expected to agree within the precision of my calculations.

Finally, my calculated results can also be compared to experimental [23, 34, 95] values. However, table 5.1 shows that three different experiments disagree with each other considerably in atomic positions of atoms in the surface trilayer, and in particular the bridging O atom. In fact, the large *inward* displacement of this atom, as found in the Surface X-ray Diffraction (SXRD) experiment [23], has been a point of contention between theory and experiment for many years [41]. As described above, even though less precise calculations did show an inward displacement toward the bulk for the bridging O atom [27], the magnitude of the displacement differed significantly from experiment. Furthermore, current, more precise calculations show that the bridging O atoms relaxes outward, away from the bulk [32].

Comparing the errors listed for the experimentally determined atomic displacements in table 5.1 shows that the SXRD experiments are more precise for subsurface atoms, whereas the Low Energy Electron Diffraction (LEED) [34] results are more precise for atoms near the surface. This is consistent with the expectations for these two experimental methods [95]. The Medium Energy Ion Scattering (MEIS) results [95] are intermediate in sensitivity between the two diffraction techniques, and help support the LEED results over those of the SXRD method for the atoms on the surface trilayer.

Comparison with experimental results shows that the displacements found for my 5-trilayer slab are in very good agreement with the more precise LEED results [34] for the atoms in the surface trilayer, and agree well with both the SXRD [23] and LEED results for the displacements of atoms that are deeper into the surface. However, this close agreement is not seen for any other slab thickness, which brings two questions to mind. First, why does the 5-trilayer slab agree so well with experiment? And second, since the atomic displacements are not converged until a slab with a thickness of nine trilayers is used, do my calculated results agree at all with those found experimentally?

The answer to the first question comes from the nature of the data that has been shown in table 5.1. In order to determine a displacement for an atom, it is required to have an initial position for the atom. Experimentally, displacements are reported for atoms that are close to the surface, and the reference positions are those of the bulk structure. However, these displacement values require the assumption that atoms that are too deep below the surface to be observed experimentally are in their bulk-like positions, which, as shown by my calculations, is not the case [32]. Therefore, the experimental displacements are given relative to some arbitrary fiducial reference plane parallel to the surface. Specifically, for the experimental values listed in table 5.1, this fiducial reference plane coincides with the center plane of the third trilayer from the surface. Since my calculated displacements using a 5-trilayer slab are found

relative to the same fiducial plane, they compare well with the displacements found experimentally. While this agreement between my calculated results and experiment for this particular slab thickness is encouraging, the second question concerning the overall agreement between my calculations and experiment remains. This more complex issue is addressed in the next section.

5.3 Bond Lengths and Angles

If the surface structure is specified with more meaningful quantities such as bond lengths and bond angles instead of atomic displacements from the bulk terminated structure, the need for an arbitrary reference point is removed. Table 5.2 shows the theoretically [27] and experimentally [23, 34, 95] determined bond lengths for the same models for which displacements were reported in table 5.1. The specific bonds are labeled in accordance with figure 5.1. When comparing the bond lengths for my calculations with slabs of different thicknesses, it is observed that the results for the 5-trilayer slab are converged to within 1%. The worst performer is bond H, which is not too surprising since this bond links the central trilayer, which is fixed by symmetry in the 5-trilayer slab to the trilayer closer to the surface. The convergence for this bond improves for the 7-trilayer slab. Additionally, table 5.2 confirms the agreement of my results with experiment by showing that the bond lengths for all of the experimental an previously calculated theoretical results are in good agreement, both among themselves and with my calculated results for slabs containing at least five trilayers.

However, the results shown in table 5.2 raise an additional quandary since it is apparent that bond lengths converge faster, with respect to slab thickness, than do atomic displacements. In order to understand why this occurs, I investigated the role that the angles formed by adjacent bonds play on the surface structure as the slab thickness is varied [33]. Specifically, eight distinct bond angles exist for each trilayer,

Table 5.2: Relaxed bond lengths, given in Å, for pairs of atoms at and near the TiO_2 (110) surface. Results from the present study [32] are labeled by the number of trilayers in the slab. Additional values are shown from three experiments [23, 34, 95] and a previous DFT calculation [27], where the bond lengths were calculated from the displacement data, given with the exception of those from the SXRD experiment[23]. Figure 5.1 illustrates the bonds labeled $A - L$, where I is omitted. The column labeled 7* has been designed to match the previous theoretical results, as explained in the text.

Bond Label	Bond Length (Å)											
	SXRD[23]	MEIS[95]	LEED[34]	Calc.[27]	3	5	7	7*	9	11	13	15
A	1.71±0.07	1.91±0.15	1.85±0.05	1.80	1.85	1.84	1.84	1.82	1.84	1.84	1.84	1.84
B	2.15±0.09	1.99	2.15±0.15	2.04	2.05	2.04	2.04	2.04	2.04	2.04	2.03	2.04
C	1.99±0.09	2.01±0.14	2.08±0.09	2.09	2.10	2.11	2.11	2.08	2.12	2.12	2.12	2.12
D	1.84±0.05	1.95	1.90±0.12	1.95	1.92	1.92	1.93	1.92	1.93	1.92	1.93	1.92
E	1.84±0.13	-	1.79±0.11	1.85	1.86	1.83	1.82	1.86	1.82	1.82	1.81	1.82
F	1.97±0.12	2.14±0.19	1.90±0.15	1.90	-	1.89	1.86	1.90	1.86	1.86	1.85	1.85
G	1.99±0.05	-	2.00±0.13	1.97	-	1.98	1.97	1.97	1.97	1.97	1.97	1.97
H	2.18±0.11	-	2.11±0.18	2.11	-	2.13	2.17	2.08	2.21	2.21	2.21	2.21
J	2.00±0.08	-	2.01±0.10	2.02	-	2.02	2.04	2.01	2.05	2.05	2.05	2.05
K	1.92±0.06	-	1.92±0.20	1.97	-	1.96	1.96	1.97	1.97	1.97	1.97	1.97
L	1.94±0.06	-	1.89±0.16	1.90	-	1.91	1.90	1.91	1.90	1.89	1.89	1.89

Table 5.3: Angles formed when bond angles are projected onto the (001) plane. Results from the present study [33] are labeled by the number of trilayers in the slab, and compared with the angles calculated from the LEED data [34]. The angles are denoted by $(\alpha - \beta - \gamma)$ where the angle is between the $(\alpha - \beta)$ and $(\beta - \gamma)$ bonds, and the atom labels (α, β, γ) are shown in Figure 5.1.

Angle Label	Projected bond angles in degrees						
	LEED[34]	5	7	9	11	13	15
O(3)-Ti(I)-O(2)	90.5±2.9	88.6	88.1	87.0	87.0	87.2	87.4
O(2)-Ti(II)-O(4)	112.7±3.0	105.3	105.4	105.9	106.0	105.7	106.3
Ti(I)-O(2)-Ti(II)	156.7±4.9	166.0	166.5	167.1	167.0	167.1	166.3
O(6)-Ti(III)-O(5)	100.9±6.6	92.9	93.4	94.4	94.3	94.3	94.3
O(5)-Ti(IV)-O(7)	81.5±2.2	85.3	83.7	82.5	82.4	82.4	82.4
Ti(III)-O(5)-Ti(IV)	178.9±6.2	178.2	177.1	176.9	176.7	176.7	176.7

but only a small number play a role in the relaxation of the atoms in the (110) direction. Additionally, due to the symmetries of the surface unit cell, relaxation of the atoms into the surface structure will not yield atomic displacements in the [001] direction. Therefore, the role played by the bond angles can be observed in a much clearer fashion by projecting them onto the (001) plane. By performing this projection, the number of distinct angles is reduced from eight to three for each trilayer, and my values for these three projected angles are tabulated, along with those calculated from the LEED [34] experimental data, in table 5.3. As the data show, the projected bond angles do not converge until a slab thickness of nine trilayers is used, which is the same slab thickness that is required for the atomic displacements to converge. Additionally, the converged angles do not agree nearly as well as the converged bond lengths with the experimental results. This is perhaps not too surprising since bond angles are relatively soft degrees of freedom compared with bond lengths.

Together, the meaningful quantities of bond angles and bond lengths explain the relatively slow convergence of atomic displacements with respect to slab thickness. The close tracking of convergence of bond angles and atomic displacements show that displacements in slabs thicker than five trilayers, which is the slab thickness for which bond lengths are converged, are the result of two different effects. First, table 5.3 shows that as slab thickness increases up to nine trilayers, the projected angles for the surface layer change. Second, vertical-relaxation errors for deeper atoms result in additional small changes in the atomic displacements.

Surface atomic structures for this material and many other covalently bonded solids have typically been reported by specifying relaxed absolute atomic positions (as displacements from bulk positions), which requires specifying an artificial reference plane. However, one is unable simply to assume that the third TiO plane down from the surface has a bulk-like geometry and expect to obtain correct atomic displacements, due to the combination of vertical relaxation errors and the relatively slow convergence of the bond angles as discussed above. Additionally, I have shown that small changes in projected bond angles ($\approx 1^\circ$) can result in significant changes in atomic displacements without a simultaneous perceptible change in bond lengths. Therefore, only reporting atomic displacements has the potential to hide multiple different effects, and as a result, I believe that a different approach should be used for reporting surface structures. Specifically, bond lengths and bond angles should be specified either in addition to, or instead of, absolute atomic positions [32].

5.4 An Efficient Model for the (110) Surface

From the data and explanations in the previous sections, it is apparent that a 5-trilayer slab, with a symmetry plane at the TiO plane of the middle trilayer, is a reasonably well converged model for the TiO_2 (110) surface. However, this model has two surfaces, as do all of the slab models presented so far. There is another,

perhaps more efficient way, to model the surface. If a slab containing m-trilayers is used, and the bottom n-trilayers are fixed in their bulk positions, the resulting model has only a single surface, and the opposite side of the slab is assured of having bulk-like properties. This $m(n)$ model is commonly used to model surfaces [11, 12, 32] since it has the potential to reduce the number of atoms and degrees of freedom in the calculations, and therefore require significantly less computational time. However, convergence issues still remain.

Table 5.4 shows my calculated bond lengths for six different slabs with fixed lower trilayers. In each case, at least the bottom two trilayers were fixed, in order to minimize any relaxations that would result due to the vacuum below the slab. The remaining $m-n$ trilayers were allowed to relax fully, and their bond lengths are found to agree well with both experiment [23, 34, 95] and the previously modeled symmetric, double-surfaced 7-trilayer slab [32], which is well converged. Since a 5-trilayer slab is converged with respect to the bond lengths, only the two trilayers nearest the surface show significant relaxation from the bulk-like structure. Therefore, the atoms in both the central trilayer and the third trilayer from the surface for a 7-trilayer slab are very near a bulk-like structure. Fixing the atoms in these trilayers to a bulk-like structure and then only modeling a single surface results in a slab that has a 4(2) configuration. Therefore, the two surfaces modeled by the 7-trilayer slab translates very well into a single surface model using a 4(2) slab. This explains the good agreement seen between this slab and the 7-trilayer slab in table 5.4.

However, in order to be useful in future investigations, my slab model must not only accurately reproduce a bare, stoichiometric surface, but also be capable of precisely evaluating additions to or defects in the surface. Specifically, since I will be adding Cu atoms and nanoclusters to the surface, I have calculated the adsorption energy that results when a Cu atom is placed above the bridging O atom. I will also be studying the effect of defects, particularly bridging O vacancies, so the vacancy

Table 5.4: Relaxed bond lengths, given in Å, for pairs of atoms at and near the TiO_2 (110) surface. Results from the present study are labeled by $m(n)$ where m is the number of trilayers in the slab, and n in the number of trilayers at the bottom that are fixed in their bulk-like positions. Additional values are shown from the symmetric, double-surface 7-trilayer slab previously reported, as well as the LEED experimental values [34]. Figure 5.1 illustrates the bonds labeled $A - L$, where I is omitted. Additionally, the calculated adsorption energy for a single Cu atom and the formation anergy of a bridging O vacancy are provided for comparison.

Bond Label	Bond Length (Å)							
	LEED[34]	7	4(2)	5(2)	6(2)	6(3)	7(2)	7(3)
A	1.85±0.05	1.84	1.84	1.84	1.84	1.84	1.83	1.84
B	2.15±0.15	2.04	2.04	2.04	2.04	2.03	2.04	2.04
C	2.08±0.09	2.11	2.11	2.11	2.12	2.12	2.11	2.12
D	1.90±0.12	1.93	1.92	1.92	1.92	1.93	1.93	1.93
E	1.79±0.11	1.82	1.82	1.82	1.82	1.82	1.82	1.82
F	1.90±0.15	1.86	1.87	1.87	1.85	1.86	1.85	1.86
G	2.00±0.13	1.97	1.97	1.97	1.97	1.97	1.97	1.97
H	2.11±0.18	2.17	2.19	2.17	2.21	2.20	2.18	2.21
J	2.01±0.10	2.04	2.04	2.04	2.05	2.05	2.05	2.05
K	1.92±0.20	1.96	1.97	1.96	1.97	1.97	1.97	1.97
L	1.89±0.16	1.90	1.90	1.90	1.89	1.90	1.90	1.89
E_A of Cu (eV)		1.68	1.68	1.72	1.67	1.68	1.69	1.68
E_F of O_B vacancy (eV)		4.52	4.51	4.46	4.54	-	4.52	-

formation energy, as defined and explained in the following chapter, is also given for the majority of slab models. As illustrated by the energies in table 5.4, both energies are nearly identical among themselves and to the values obtained for the symmetric 7-trilayer slab. However, it is also apparent that while these energies for the 4(2) slabs are not necessarily converged, they are representative of the converged values to within 0.02 eV. This is shown by the significant difference in the energies for the 5(2) slab from the other values. Further evidence for additional vacancy configurations, shown in the following chapter, confirms that the energies obtained when using the 4(2) slab are consistently representative of the converged values. The 4(2) slab also contains the fewest number of atoms, and degrees of freedom for those atoms, which is essential for modeling relatively large surfaces with maximal efficiency. As a result, the 4(2) model for a single surface unit cell has been shown to be the most computationally efficient surface model [11, 32], and will be the basis for the remaining surface calculations presented in this dissertation.

Chapter 6

Defects on the (110) Surface

6.1 Bridging Oxygen Vacancies

To this point, only the stoichiometric (110) surface has been considered. However, real applications involving TiO_2 surfaces will not have this perfect, ideal structure, due to the presence of defects in the surface. As discussed in chapter 2, defect sites play an important role in the catalytic process, since they effect the electron-hole recombination rate [62, 63]. Additionally, defective sites on the surface have been shown to play an active role in both the absorption of co-catalysts and reactants [38, 39, 47, 96, 97]. In particular, the point defect caused by the removal of the surface bridging O atom (denoted as atom number 1 in figure 5.1) has been shown to require the least amount of energy to form, and is, therefore, the most likely defect to occur, either at [36] or near [37] the surface. In the remainder of this dissertation, the term "vacancy" will always refer to a bridging O vacancy.

Experimentally, these vacancies have been observed in a variety of arrangements on the surface, including isolated point defects [38, 39], small clusters along bridging O rows [46], and 2-D ordered configurations [47, 48]. While there have been numerous investigations on the effects of bridging O vacancies on the electronic and structural properties of TiO_2 [24, 28, 29, 36, 37, 40–45], the adsorption of co-catalysts such as Au and Pt [10–16], and the adsorption of O_2 and molecules such as CO [65, 98–101], they have all primarily focused on the role of isolated defects. However, the effects of clusters of vacancies are significantly different from those of an isolated vacancy (as discussed in detail in later chapters). Attempts have been made by others

to investigate the vacancy-vacancy interactions that are responsible for the diverse arrangements of these defects. However, until this point, theoretical studies have only succeeded in explaining the occurrence of isolated point defects by demonstrating that isolated bridging O vacancies are energetically favorable [10, 14].

Determining interactions between vacancies and predicting vacancy arrangements on surfaces that are comparable to experiment require the calculation of the total energy of both stoichiometric and defective surfaces. The difference between these two energies can then be used to determine the vacancy formation energy, E_V, shown in equation 6.1. The remaining term in equation 6.1 accounts for the O atoms present in the stoichiometric but not the defective surfaces. Since it is assumed that any O atoms that leave the surface go on to form O_2, one half the energy of an O_2 molecule must then be added to determine the formation energy of a single vacancy.

$$E_V = E_{def} - E_{st} + \frac{1}{2}E_{O_2} \tag{6.1}$$

Therefore, determining the vacancy formation energy requires that the energy of molecular O_2 be calculated using DFT, which I found to be -9.81 eV. While this value cannot be compared to experimental results as is, the atomization energy (for which experimental values are available) can be determined by performing an additional calculation for the O atom. Care must be taken when modeling the O atom, since spherically symmetric calculations of an O atom result in the four 2p electrons being evenly distributed among the three degenerate p orbitals [102]. However, the correct ground-state electron configuration has integer fillings for each orbital. In order to correctly model the ground-state electron configuration of O, this degeneracy must be removed. This can be done in VASP [7–9] by performing the atomic O calculation in an orthorhombic supercell, which results in a converged energy of -1.96 eV.

Therefore, the atomization energy is 2.94 eV which is similar to comparable theoretical results (which range from 2.95 to 3.02 eV for GGA and 3.58 to 3.74 eV for LDA calculations) [102] but does differ noticeably from the experimental value of 2.56 eV [103]. Such overestimation is a known shortcoming of DFT calculations. It is expected that accuracy for vacancy formation energies will be much better than for O_2 atomization energy.

My previous calculations have focused on ensuring very precise determination of both energies and bond lengths. While bond lengths are important in this case as well, the fact that the vacancy formation energy is found by taking the *difference* between two DFT calculated energies means that some of the parameters used can be changed to less stringent criteria, since energy differences result in error cancelations. While care must be taken to ensure that the new calculated vacancy formation energies are comparable to those determined under the more computationally stringent settings, the computational time can be significantly reduced. Specifically, when the PREC flag is set to Normal (instead of Accurate) and real space projection operators (instead of reciprocal space projection operators) are used [9], the calculated vacancy formation energies are found to be within 0.1 % (smaller surface unit cells) to 0.4% (larger surface unit cells) of the more precisely calculated values. Even though both of these changes correspond to a worsening of the computational approximations used, comparable vacancy formation energies are obtained because the errors introduced by the changes in these flags are both small and approximately constant for nearly identical systems [9]. Since this small difference is comparable to other approximations made, such as the finite sampling of the Brillouin zone, and since the time required for the calculations under these conditions is significantly less, all of my calculations used to determine vacancy formation energies are done with these settings.

While the changes made above shorten the computational time required for my calculations, the inclusion of surface defects, such as bridging O vacancies, can sig-

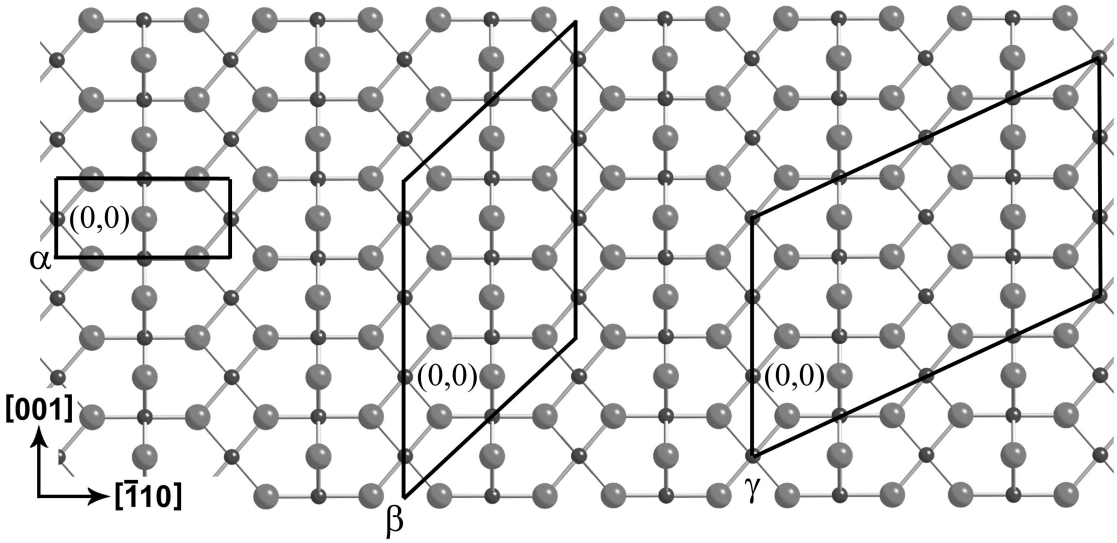

Figure 6.1: A ball and stick model of an overhead view of the TiO_2 (110) surface. Unit cells for an orthogonal (1 × 1) primitive surface unit cell (α), a non-orthogonal (1 × 4) cell (β), and a non-orthogonal (2 × 3) cell (γ) are shown, were the (A×B) cell is constructed by forming a cell that has a length of A primitive unit cells in the [$\bar{1}$10] direction and B in the [001] direction. Additionally, the bridging O sites on the surface can be labeled in coordinate form, ($x_{[\bar{1}10]}$,$x_{[001]}$), where integer values of x denote the position of a bridging O site in the [$\bar{1}$10] and [001] directions, relative to an origin (0,0) site. By convention, the origin is chosen to be the bridging O site in the lower left-hand corner of the unit cell, as labeled (to the left of the bridging O atom) above.

nificantly alter the physical and electronic structure of the surrounding atoms. This may result in the need to modify the model used to study the surface, and therefore may require additional computational resources. Specifically, the $2\times4\times2$ Monkhorst-Pack [84] k-point set does not yield a converged vacancy formation energy, within the desired precision, for the primitive (1×1) surface unit cell, labeled as α in figure 6.1. Therefore, I retested k-point convergence and determined that a $4\times8\times2$ Monkhorst-Pack [84] k-point set is required in order to obtain vacancy formation energies that are precise to within approximately 20 meV. When larger unit cells are used, I systematically reduced the k-point set in the reciprocal space direction by the same factor that the unit cell is increased for the corresponding directions labeled in figure 6.1. For example, the (2×4) orthogonal cell is constructed by forming a cell that has a length of 2 primitive unit cells in the $[\bar{1}10]$ direction and 4 in the [001] direction. Thus the appropriate, well converged k-point set is $\frac{4}{2}\times\frac{8}{2}\times2 = 2\times2\times2$. The one exception to my method of reducing the k-point sampling as the unit cell size increases is for a (2×3) orthogonal cell, since $\frac{8}{3}$ is not an integer. Therefore, I used a $2\times2\times2$ Monkhorst-Pack [84] k-point set, which gave well converged results.

With the necessary modifications to the computational parameters made, the investigation of how bridging O vacancies interact with each other and with the surface can begin. This requires examining many distinct vacancy arrangements on the surface, which means that very large surface unit cells will be needed. In fact, one possible reason that theoretical investigations have not yet yielded additional defect arrangements, beyond isolated point defects, is due to the very large number of atoms needed for slabs with large enough surface unit cells to accurately model the defective surface. The 4(2) slab, discussed previously, has been shown to give efficient, accurate surface calculations, and its use allows for the study of a multitude of defect arrangements in significantly less time than would otherwise be achievable. Care must be taken, however, in using the 4(2) slab for surfaces with vacancies, since

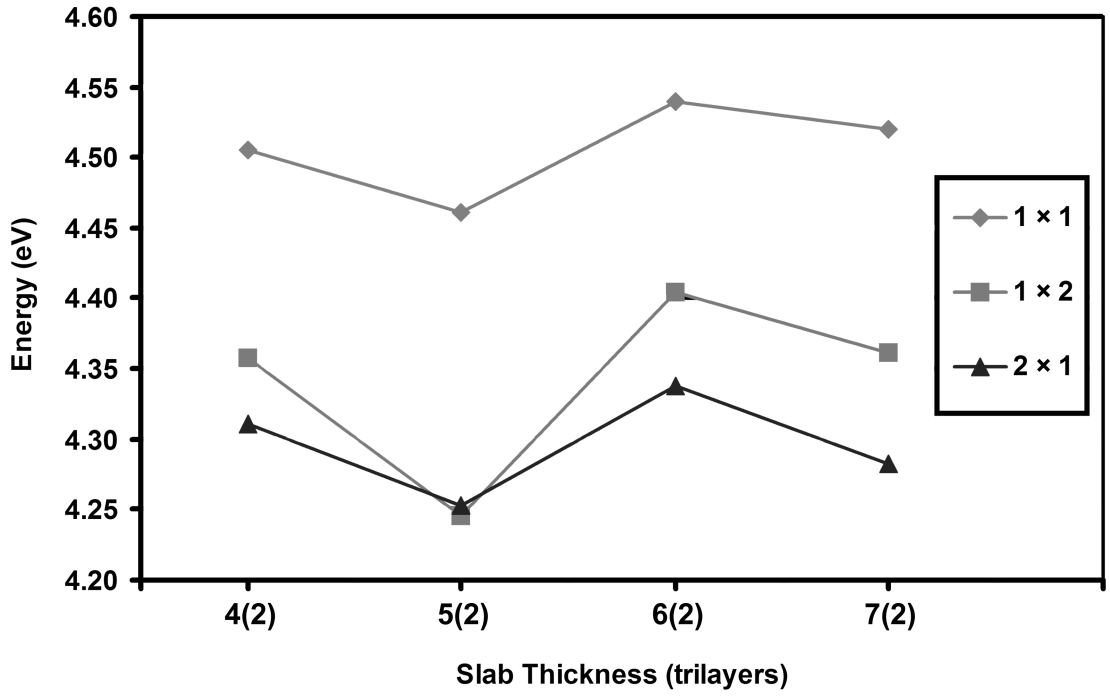

Figure 6.2: The convergence of the vacancy formation energy with respect to slab thickness is shown for orthogonal 1×1, 1×2, and 2×1 unit cells as defined in the text and illustrated in figure 6.1.

it was originally tested only for defect free surfaces. Since bridging O vacancies result in significant relaxations that penetrate into the slab, additional testing is required to ensure that the 4(2) slab is suitable for modeling defective surfaces.

To do this, I calculated the vacancy formation energies, equation 6.1, for the three smallest unit cells giving distinct vacancy arrangements on the (110) surface, for slabs ranging from a thickness of 4(2) to 7(2) trilayers. Specifically, one bridging O atom was removed for the 1×1, 1×2, and 2×1 orthogonal cells. This corresponds to a surface devoid of bridging O atoms for the 1×1 cell, and 50% vacancy concentration for the two remaining cells, where either an entire [001] rows of bridging O atoms are missing (2×1) or alternating vacancies are present along the [001] bridging O rows (1×2).

The convergence of the vacancy formation energy with respect to slab thickness is shown in figure 6.2. For each unit cell, the vacancy formation energy of the 4(2) slab is comparable to that found for the thicker 6(2) and 7(2) slabs. Additionally, the trends in vacancy formation energy with respect to the defect arrangements on the surface is comparable for the 4(2), 6(2), and 7(2) slabs. While the effects of the surface defect do penetrate further into the slab than the second trilayer, figure 6.2 demonstrates that use of a 4(2) slab results in a good approximation for the vacancy formation energy. Furthermore, while it would be more accurate to use thicker slabs when surface defects are included, the additional computational resources required would prohibit the study of 2×3 and 2×4 cells, which are necessary to develop a good model of vacancy-vacancy interactions.

6.2 Predicting Vacancy Formation Energies

Using a 4(2) trilayer slab, I investigated how the effects of a bridging-O vacancy extend along the TiO_2 (110) surface and how multiple vacancies interact which each other. Specifically, I performed DFT total energy calculations in order to determine the average vacancy formation energy (equation 6.1) for 21 distinct arrangements of bridging O vacancies, as listed and described in table 6.1. For each arrangement, the vacancy location is specified in a coordinate form, $(x_{[\bar{1}10]},x_{[001]})$, where integer values of x denote the position of a bridging O site in the $[\bar{1}10]$ and [001] directions, relative to an origin (0,0) site. By convention, the origin is chosen to be the bridging O site in the lower left-hand corner of the unit cell, as shown in figure 6.1. In each case, I estimate the precision of the average vacancy formation energy found using DFT to be 1-2%. The largest contributors to this uncertainty are the 4(2) trilayer slab model, finite sampling of the Brillouin zone, and the specific computational parameters mentioned in detail in the previous section.

Table 6.1: Arrangements of bridging O vacancies on the specified periodic unit cells. The vacancy locations are specified in a ($x_{[\bar{1}10]}$,$x_{[001]}$) form, as descried in the text and figure 6.1. All of the unit cells are built from the orthogonal primitive unit cell (labeled α in figure 6.1) except the 1×4* cell, which is labeled β in figure 6.1. Additionally, vacancy formation energies, calculated using DFT and the vacancy interaction model are given, as is the % error which is determined by assuming the DFT values are correct.

Unit Cell	Vacancy Location	DFT E_V (eV)	Model E_V (eV)	% Error (%)
1×1	(0,0)	4.47	4.42	1.05
1×2	(0,0)	4.26	4.19	1.67
1×4	(0,0)	3.46	3.51	1.45
1×4	(0,0),(0,1)	3.88	3.86	0.44
1×4	(0,0),(0,1),(0,2)	4.27	4.27	0.01
2×1	(0,0)	4.31	4.30	0.26
2×2	(0,0)	4.13	4.07	1.48
2×2	(0,0),(1,1)	4.23	4.23	0.07
2×3	(0,0)	3.44	3.45	0.17
2×3	(0,0),(1,0)	3.58	3.57	0.36
2×3	(0,0),(0,1)	4.12	4.11	0.15
2×3	(0,0),(1,1)	3.57	3.53	1.07
2×3	(0,0),(1,0),(0,1)	4.00	4.00	0.18
2×3	(0,0),(1,1),(1,2)	4.00	4.00	0.04
2×3	(0,0),(1,0),(0,1),(1,1)	4.23	4.23	0.05
2×3	(0,0),(1,0),(0,1),(0,2)	4.18	4.19	0.18
2×3	(0,0),(1,0),(0,1),(1,2)	4.23	4.25	0.50
2×3	(0,0),(1,0),(0,1),(1,1),(0,2)	4.35	4.35	0.05
2×4	(0,0)	3.34	3.39	1.41
1×4 *	(0,0)	3.44	3.39	1.34
1×4 *	(0,0),(0,1)	3.88	3.82	1.47

Figure 6.3 shows the average vacancy formation energy for all 21 configurations studied, plotted versus concentration of bridging O vacancies on the surface. Also plotted in figure 6.3, previously published vacancy formation energies [10, 12, 36, 101], calculated using comparable approximations. All previous calculations are in good agreement with my results. Two main conclusions can be drawn from these results. First, as a bridging O vacancy becomes more isolated, i.e. the vacancy concentration gets smaller, the energy required to form that vacancy decreases. This is consistent with the experimental observations of isolated point defects [38, 39], and is in agreement with the conclusions of previous theoretical investigations [10, 14].

The second conclusion is not as obvious, but is extremely important for successful modeling of isolated vacancies. When combined with the specific arrangements detailed in table 6.1, it is apparent that a significant, although small, difference in vacancy formation energy is obtained for the cases of a single vacancy on the 2×3 and 2×4 cells, which correspond to vacancy concentrations of 16.7% and 12.5% respectively. This suggests that a bridging O vacancy at some position (0,0) on the surface has a non-negligible interaction with another vacancy located at (0,3). While this alone does not imply that longer range interactions are negligible, it does indicate that the range of vacancy interactions extends at least 9 Å along the [001] bridging O rows. As a result, in order to model isolated bridging O vacancies with orthogonal unit cells, a large 2×4 cell or, if lower precision is acceptable, a somewhat smaller 2×3 cell is required. Due to the large volume and relatively high number of atoms involved, current investigations using these unit cells are very computationally intensive.

Additional conclusions regarding vacancy-vacancy interactions are not readily apparent from figure 6.3. However, the data listed in table 6.1 can be used to develop a vacancy-vacancy interaction Hamiltonian, which is constructed by summing terms of increasing interaction order, i.e. on-site, 2-body, 3-body, etc. interactions, as shown in equation 6.2. In this equation, a single index k (l,m) is used to count over all bridging

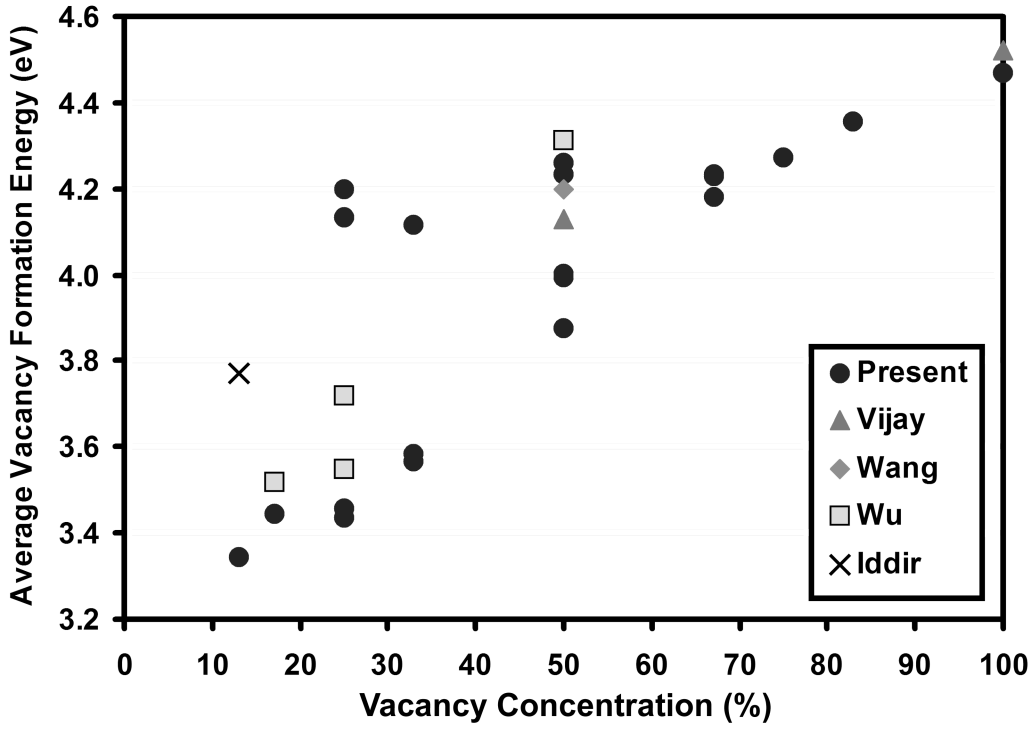

Figure 6.3: The average vacancy formation energy is plotted versus the vacancy concentration on the TiO_2 (110) surface for the arrangements listed in table 6.1. Additionally, theoretical results are shown for Vijay [10], Wang [36], Wu [101], and Iddir [12], which were done using comparable approximations.

O lattice sites ($N_{[\bar{1}10]} \times N_{[001]}$) on the 2-D surface. The binary variable, σ_k, is defined to be 1 if a bridging O vacancy exists at the k^{th} site on the surface, and 0 otherwise. The coefficient "c" corresponds to the isolated vacancy formation energy (interaction order 1), and the remaining coefficients (a,b,d,...) describe terms of higher interaction order. These multi-body interaction coefficients are functions of the orientation of the bridging O vacancies included in the corresponding term. The parameters α_{kl}, β_{klm}, etc. label distinct vacancy cluster arrangements for vacancy pairs, triples, etc., respectively. Since the lattice constants for the TiO_2 (110) surface are different in the $[\bar{1}10]$ and [001] directions, the relative distances of neighboring bridging O sites are not immediately obvious. Figure 6.4 delineates the neighboring bridging O sites, up to the 10^{th} nearest neighbor, for a bridging O vacancy at the position labeled 0. This neighbor number can then be used to specify the multi-body interaction coefficients in equation 6.2. Specifically, for 2-body interactions, $\alpha_{kl} = 1$ corresponds to a vacancy pair in which sites k and l are nearest neighbors, $\alpha_{kl} = 2$ denotes a second-nearest-neighbor pair, and so on. Describing the 3-body interaction coefficients is a little more difficult, but can also be done using neighbor numbers. For example, three vacancies located at the origin (0,0), site (0,1), and site (1,0), can be mapped to the site labels 0, 1, and 3, respectively, from figure 6.4. The 3-body interaction coefficient is then specified by β_{klm} = 1,3, where all vacancy arrangements equivalent by symmetry are also given this value of β_{klm}. While higher-order multi-body interaction terms can be expressed in a similar manner, these terms will not be needed in the development of a vacancy-vacancy interaction model for TiO_2, and therefore, are not included in this discussion.

$$H_{int} = \sum_k c\sigma_k + \frac{1}{2}\sum_{k,l} a(\alpha_{kl})\sigma_k\sigma_l + \frac{1}{6}\sum_{k,l,m} b(\beta_{klm})\sigma_k\sigma_l\sigma_m + \ldots \tag{6.2}$$

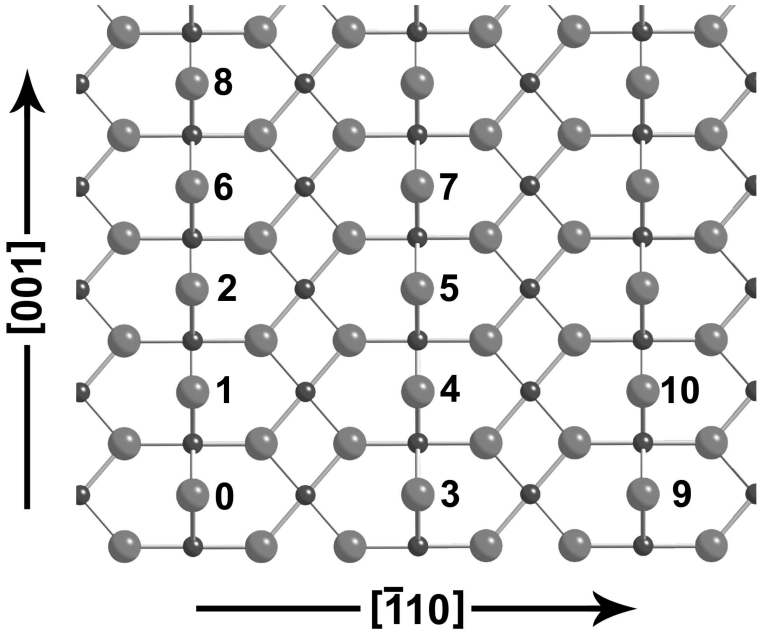

Figure 6.4: Relative locations of bridging O sites on a ball and stick model of the TiO_2 (110) surface are shown. Specifically, for a vacancy located at the site labeled 0, the neighboring bridging O sites, up to the 10^{th} nearest neighbor, are numbered according to their relative distances.

Before discussing how this vacancy interaction model can be tailored to study the TiO_2 (110) surface, it is worthwhile to compare this method to similar ones that are more commonly used. Significant research has been performed on interactions between gaseous atoms adsorbed on a surface (e.g., a lattice gas) [104, 105], and interatomic interactions in alloys [106]. In a manner similar to the vacancy interaction model developed above, theorists in both of these areas have constructed an interaction Hamiltonians similar in form to equation 6.2. However, the study of vacancy-vacancy interactions is subtly, but importantly, different from the comparable, more commonly used, lattice gas model. For the vacancy interaction model, the focus is placed on the bridging O vacancies instead of adsorbed O atoms, as done in the lattice gas model. This is done through the designation of σ_k in equation 6.2, where a value of 1 corresponds to the focus of investigation, i.e. a vacancy (as designated above for the vacancy interaction model) or adsorbed atom (in the lattice gas model). While the focus of study in the vacancy-vacancy interaction and lattice gas models is different, the models themselves are equivalent. For example, the vacancy interaction model can be recast as a model of interacting bridging O atoms. In this case, the system is thought of as the completely vacant surface (no bridging oxygens) containing M primitive unit cells, with some number, N, of O atoms added to the surface at the bridging sites. The result is a surface containing M-N vacancies. While this picture does not represent how actual defective surfaces are formed, it does provide an equivalent description for a partially vacant surface, and it lends itself to the lattice gas model [104, 105]. As discussed later in this chapter, this transformation aids in understanding particular aspects of the wide variety of vacancy arrangements.

Determining a vacancy-vacancy interaction Hamiltonian requires that the number of terms in equation 6.2 be truncated for both the interaction order and the range of the interactions. Previous attempts, using significantly fewer vacancy arrangements and considering only single and 2-body interactions, were unsuccessful at accurately

Table 6.2: The energy coefficients for vacancy-vacancy interaction model composed of isolated, 2-body, and 3-body interactions, as specified in equation 6.2 and described in the text, are listed in units of eV. The statistical errors for the fitting procedure are given in parenthesis.

Energy Coefficients (eV)		
c		3.39(5)
α_{kl}	1	0.64(5)
	2	0.68(3)
	3	0.12(3)
	4	0.08(1)
	6	0.06(2)
β_{klm}	1,2	-0.47(3)
	1,3	-0.04(1)

predicting additional vacancy arrangements [10]. Therefore, I chose to include 3-body interactions as well. The specific range of the 2- and 3-body interactions is limited by the periodicity of the unit cells used in my DFT calculations. For example, in order for the model to include a 2-body interaction between a vacancy at (0,0) and another at (1,0), which corresponds to $\alpha_{kl} = 3$, a $(2\times N_{[001]})$ surface unit cell, with integer $N_{[001]} \geq 1$, is required. As a result, the unit cells used in table 6.1 allow for the consideration of interactions that depend on first to seventh nearest neighbors, which corresponds to a range of approximately 11.5 Å. As discussed below, these limits are more than sufficient to include all significant interaction terms.

Having truncated the model Hamiltonian such that a manageable number of possible 2- and 3-body interactions remain, I used the vacancy arrangements and formation energies listed in table 6.1 to determine the best-fit energy coefficients of equation 6.2, which are listed in table 6.2. For c, the energy required to form an

isolated vacancy, I averaged the vacancy formation energies for the single vacancy located at (0,0) on the 2×4 orthogonal and 1×4 non-orthogonal (see figure 6.1, cell β) unit cells. The associated error, shown in parenthesis in table 6.2, is the difference between the average and individual values, and is comparable to the errors present in my DFT calculations. I then used a least squares fitting routine to obtain best-fit values for the 2- and 3- body interaction coefficients, listed in table 6.2, from the remaining 19 configurations shown in table 6.1. Coefficients for additional interaction terms were found to be statistically insignificant (i.e., smaller than the statistical errors of the fit). This implies that all relevant vacancy-vacancy interactions, within the precision of my DFT calculations, are included in my model. It is interesting to note that a non-negligible value exists for the $\alpha_{kl} = 6$ two-body interaction, but the $\alpha_{kl} = 5$ interaction is negligible. This occurs because the removal of a bridging O atom results in a more significant relaxation of surface atoms along the [001] bridging O row than atoms on adjacent rows. Therefore, as seen in figure 6.4, a vacancy at 0 would have a greater effect on the sixth nearest neighbor than the fifth, which results in the $\alpha_{kl} = 5$ coefficient being statistically insignificant while the $\alpha_{kl} = 6$ coefficient is not.

As seen in table 6.1, the vacancy formation energies calculated using the interaction Hamiltonian agree with the values obtained from my DFT calculations to within 1.7%. As discussed previously, this level of precision is comparable to the statistical errors in the fitting for each coefficient in the interaction Hamiltonian and that of my DFT calculations. While the agreement between DFT and model vacancy formation energies demonstrates the quality of the fit and corresponding interaction Hamiltonian, it does not illustrate the ability to predict average vacancy formation energies for vacancy arrangements not included in the fitting routine. In order to test the predictive properties of this interaction model, I performed additional calculations on 10 vacancy arrangements that are distinct from each other and from those used in

Table 6.3: Bridging O vacancy arrangements for calculations done on a 2×3 non-orthogonal (see figure 6.1 cell γ) unit cell are listed. The vacancy locations are specified in a ($x_{[\bar{1}10]}$,$x_{[001]}$) form, as descried in the text and figure 6.1. Additionally, vacancy formation energies, calculated using DFT and the vacancy interaction model are given, as is the % error which is determined by assuming the DFT values are correct.

Unit Cell	Vacancy Location	DFT E_V (eV)	Model E_V (eV)	% Error (%)
2×3	(0,0)	3.45	3.45	0.06
2×3	(0,0),(1,1)	3.56	3.53	0.95
2×3	(0,0),(0,1)	4.09	4.11	0.46
2×3	(0,0),(0,1),(1,3)	3.99	4.00	0.09
2×3	(0,0),(0,1),(1,1),(1,2)	4.22	4.25	0.71
2×3	(0,0),(0,1),(0,2),(1,1)	4.18	4.19	0.25
2×3	(0,0),(0,1),(0,2),(1,1),(1,2)	4.34	4.35	0.32
2×3	(0,0),(1,2)	3.57	3.55	0.53
2×3	(0,0),(0,1),(1,1)	3.99	4.00	0.29
2×3	(0,0),(0,1),(1,1),(1,3)	4.22	4.24	0.47

the fitting of interaction coefficients. Details for these arrangements, generated using a 2×3 non-orthogonal (see figure 6.1, cell γ) unit cell, are given in table 6.3.

Table 6.3 shows that the interaction Hamiltonian model is adept at predicting vacancy formation energies to within the expected 1.7% error. As mentioned above, when mapped onto the (110) surface, the vacancy arrangements listed in tables 6.3 and 6.1 are distinct. However, when applying the vacancy interaction model, in order for these arrangements to remain distinct from one another, the interaction range must include a ninth-nearest neighbor term. Since I found that all vacancy interactions further than sixth-nearest neighbor interactions are negligible, the first seven arrangements listed in table 6.3 are actually equivalent to arrangements listed in table 6.1. Therefore, since equivalent arrangements are used to fit the interaction model,

these seven arrangements cannot be used to demonstrate any predictive abilities of the interaction model. However, because the DFT calculated vacancy formation energies are found to be equivalent (within the expected precision), these arrangements do support the argument that all statistically relevant interactions are included in the model. Good agreement is also observed for the final three arrangements listed in table 6.3, which are distinct from those used in the fitting procedure both within and outside of the range of vacancy-vacancy interactions included in my model. As a result, the good agreement between DFT and model vacancy formation energies demonstrate that this interaction Hamiltonian model is complete with respect to interaction range and can be used to predict average vacancy formation energies.

6.3 Monte Carlo Simulations

While the interaction Hamiltonian as developed above, allows for the prediction of vacancy formation energies, the energetically preferred vacancy arrangements for different vacancy concentrations are not readily apparent. Fortunately, the lattice-gas model lends itself to use in Monte Carlo simulations of vacancy patterns on the surface at different vacancy concentrations. Additionally, Monte Carlo simulations allow for the study of relatively large systems, compared to DFT calculations. Therefore, it will be possible to simulate surfaces that are of a size comparable to those observed experimentally [46–48].

The interaction Hamiltonian in equation 6.2 is appropriate for Monte Carlo simulations in the canonical ensemble, where the temperature and number of bridging O vacancies are the independent values. However, it is important to allow for the desorption (creation of a vacancy) as well as the adsorption (removal of a vacancy) of O atoms on the bridging sites, such that the surface is considered to be in thermal and chemical equilibrium with an O_2 gas reservoir (e.g., the atmosphere above the

surface). Moreover, it is the partial pressure of this gas reservoir which is under experimental control. Since the surface and gas reservoir are in chemical equilibrium, the chemical potentials, μ, are equal, and as a result, transforming the system to one in which the independent variables are temperature and chemical potential is preferable [104]. This can be accomplished by conducting the Monte Carlo simulations in the grand canonical ensemble, which requires that a term corresponding to the chemical potential times the number of intact bridging O atoms on the surface is subtracted from equation 6.2 [104].

The grand canonical interaction Hamiltonian is shown in equation 6.3, Since a bridging O vacancy at site k corresponds to a σ_k value of 1, a summation over the entire lattice ($N_{[\bar{1}10]} \times N_{[001]}$) counts the number of vacancies. The number of intact bridging O atoms, then, is the total number of lattice sites minus the number of vacancies. Note that, care must be taken when making the change to the grand canonical ensemble, since under this notation, where the vacancies are the subject of interest, the form of the resulting Hamiltonian differs from that of the usual lattice gas model [104, 105].

$$H_{int}^{gc} = H_{int} - \mu \left[N_{[\bar{1}10]} N_{[001]} - \sum_k \sigma_k \right] \tag{6.3}$$

I then performed Monte Carlo simulations on this model Hamiltonian using the shift-register [107] R1279 [108] random number generator and Metropolis importance sampling [49, 109]. For a Monte Carlo step in the Metropolis importance sampling scheme, a change is proposed for the arrangement of vacancies on the surface lattice, and the resulting change in energy of the system is determined using the grand canonical interaction Hamiltonian. If the energy of the proposed arrangement is less than the current arrangement, the change is made. Otherwise, a random number (r) is generated and compared to the exponential of the ratio of the calculated change

in energy to k_BT, where T is the temperature of the system, as shown in equation 6.4. If this inequality is satisfied for the proposed arrangement, then the change is made. The process is then repeated for another arrangement until the system reaches equilibrium, where energy fluctuations are due to the finite temperature specified in the simulation. Further sampling is then performed until the desired amount of data has been obtained [49].

$$r \leq \exp(\frac{-\triangle E}{k_BT}) \tag{6.4}$$

For my Monte Carlo simulation, I randomly selected a site (0,0) on the surface, and then considered one of four different methods of changing the vacancy arrangement. Two of the considered arrangement changes allowed for a change in the number of vacancies present on the surface. The first of these either formed ($\sigma_k \rightarrow 1$) or removed ($\sigma_k \rightarrow 0$) a vacancy at the (0,0) site. The second allowed for the formation or removal of a nearest neighbor pair, site (0,0) and site (0,$\pm$1), of vacancies. The remaining two methods resulted in a change in the arrangement of the vacancies, but did not change the overall number. Specifically, I allowed either a vacancy (bridging O) at site (0,0) to swap positions with a bridging O (vacancy) at one of the four neighboring sites, (0,$\pm$1) and ($\pm$1,0). Similarly, the final arrangement change consisted of allowing a pair of vacancies or bridging O atoms to hop one site along a [001] bridging O row in either direction, i.e. vacancies at (0,0) and (0,+1) are moved to (0,+1) and (0,+2) or (0,-1) and (0,0).

Each Monte Carlo simulation began with a randomly arranged ($N_{[\bar{1}10]} \times N_{[001]}$) surface, a random vacancy concentration, and a fixed surface chemical potential. The temperature was then reduced from 500 K to 100K in five equal steps. For each temperature, I conducted 20,000 Monte Carlo sweeps, where one sweep is composed of $4N_{[\bar{1}10]}N_{[001]}$ Monte Carlo steps, with each of the four above mentioned methods

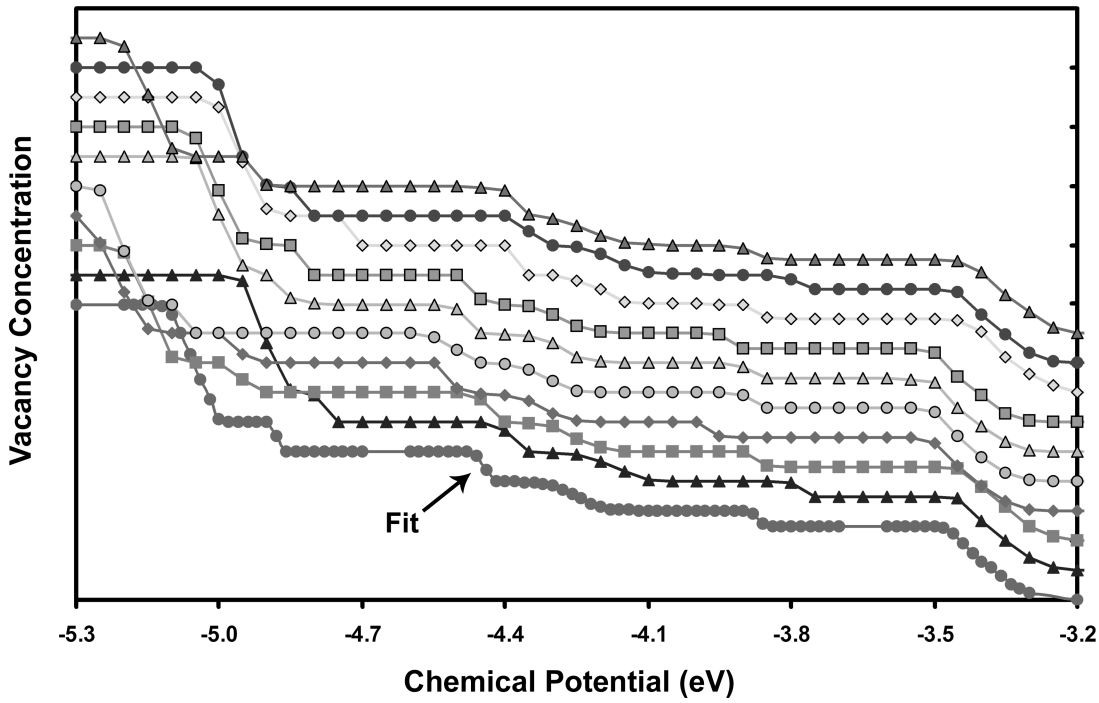

Figure 6.5: Monte Carlo results from Hamiltonians with coefficients varied within their respective error bars are shown on a vacancy concentration versus surface chemical potential plot. For comparison, each curve (representing a different Hamiltonian) is offset in the y-axis, and runs from a completely vacant surface at the left to a fully stoichiometric at the right. Statistical error bars are smaller than the plotted points.

for changing the vacancy arrangement being attempted $N_{[\bar{1}10]}N_{[001]}$ times. Testing ensured that an equilibrium vacancy concentration and arrangement was obtained for each temperature. The exact number of steps needed to reach an equilibrium vacancy concentration depends on the cell size and the chemical potential, and typically varied between 500 and 5,000 Monte carlo steps for my simulations. Statistical averages and errors where then obtained by conducting 25 distinct simulations for each chemical potential.

In order to robustly predict specific structural phases, it is important that the vacancy concentrations and patterns obtained from my Monte Carlo simulations are not sensitive to the specific numerical values of the model coefficients listed in table 6.2. Therefore, I conducted a series of nine tests, where the coefficients were randomly varied within their respective error bars. For each test, I performed 25 Monte Carlo simulations on a relatively small 6×20 cell. The results are shown in figure 6.5, where for comparison, each curve (representing a different Hamiltonian) is offset in the y-axis. The horizontal axis is chemical potential and runs from fully stoichiometric at the right to a completely vacant surface at the left. The bottom curve, labeled Fit, corresponds to the best-fit model coefficients, as listed in table 6.2. When compared to the other nine curves, it is apparent that the same trends in average vacancy concentration occur for similar ranges of surface chemical potential. Specifically, the vacancy concentration is seen to remain constant at values of 25% and 50% over two relatively wide (∼0.4 eV each) ranges of chemical potential. Other similar features of the ten curves primarily reflect finite size effects, as discussed below. Overall, figure 6.5 demonstrates that the predictions of vacancy structural phases are insensitive to small variations of the model coefficients within their error bars.

Having demonstrated the robustness of my model Hamiltonian, I proceeded to perform simulations on larger lattice sizes, using surface cells of size 6×20, 18×60, and 90×200. The largest cell, 90×200, corresponds to a 587 Å × 594 Å surface region and is comparable in size to experimentally observed terrace regions for the (110) surface of TiO_2 [46–48]. Figure 6.6 shows a plot of vacancy concentration vs. chemical potential for room temperature (300 K) simulations. As the chemical potential is increased, the surface progresses from completely vacant at the left of figure 6.6(a) to fully stoichiometric at the right of figure 6.6(b). Comparison of the three simulation cells reveals that finite size effects are almost completely absent in the 18×60 simulation cell.

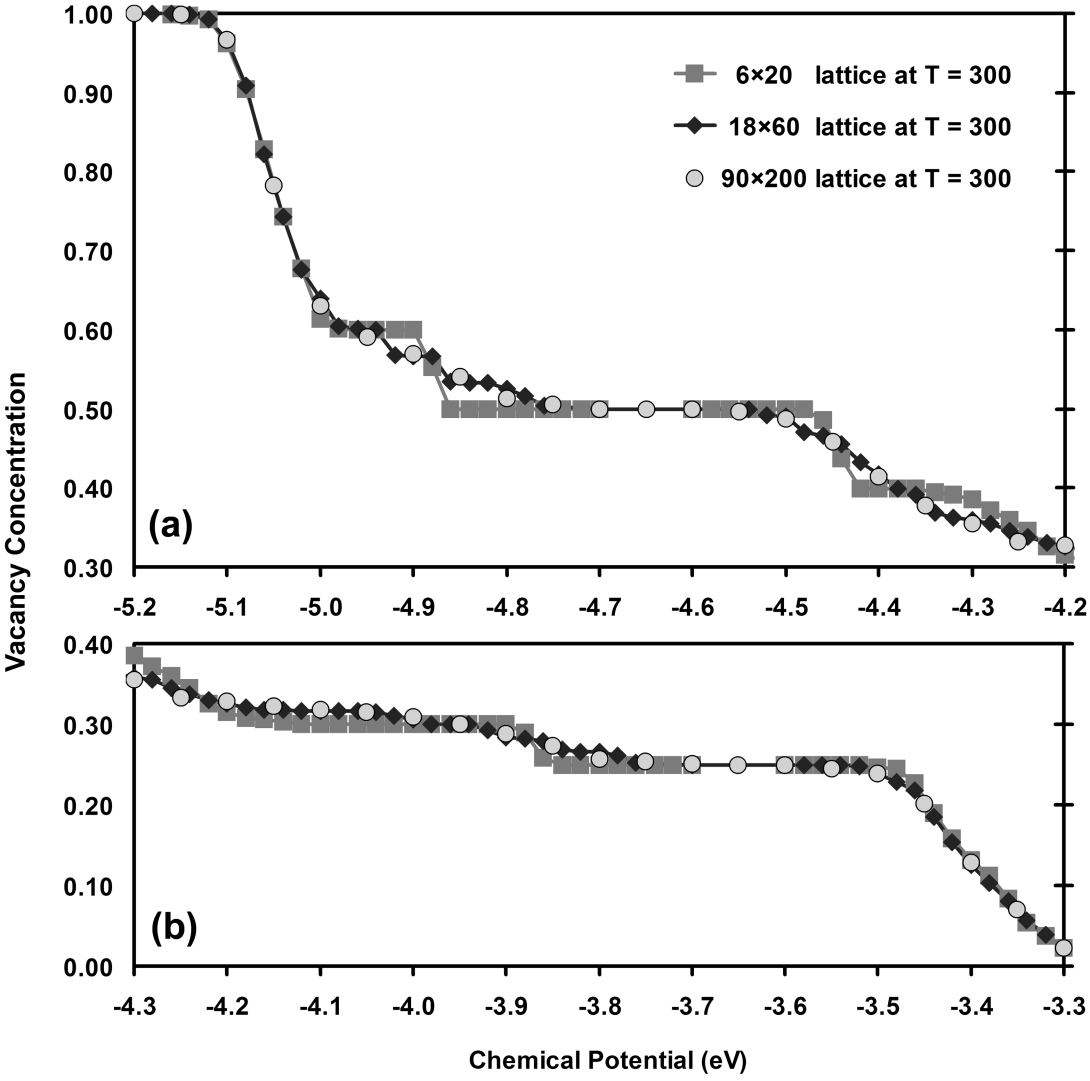

Figure 6.6: Plot of the concentration of bridging O vacancies vs. chemical potential of the surface for three different simulation cell sizes at a simulated temperature of 300 K. As the chemical potential is increased, the surface progresses from completely vacant at the left of (a) to fully stoichiometric at the right of (b), where a small overlap of chemical potential is included in the two plots. The statistical error bars are smaller than the points in each curve.

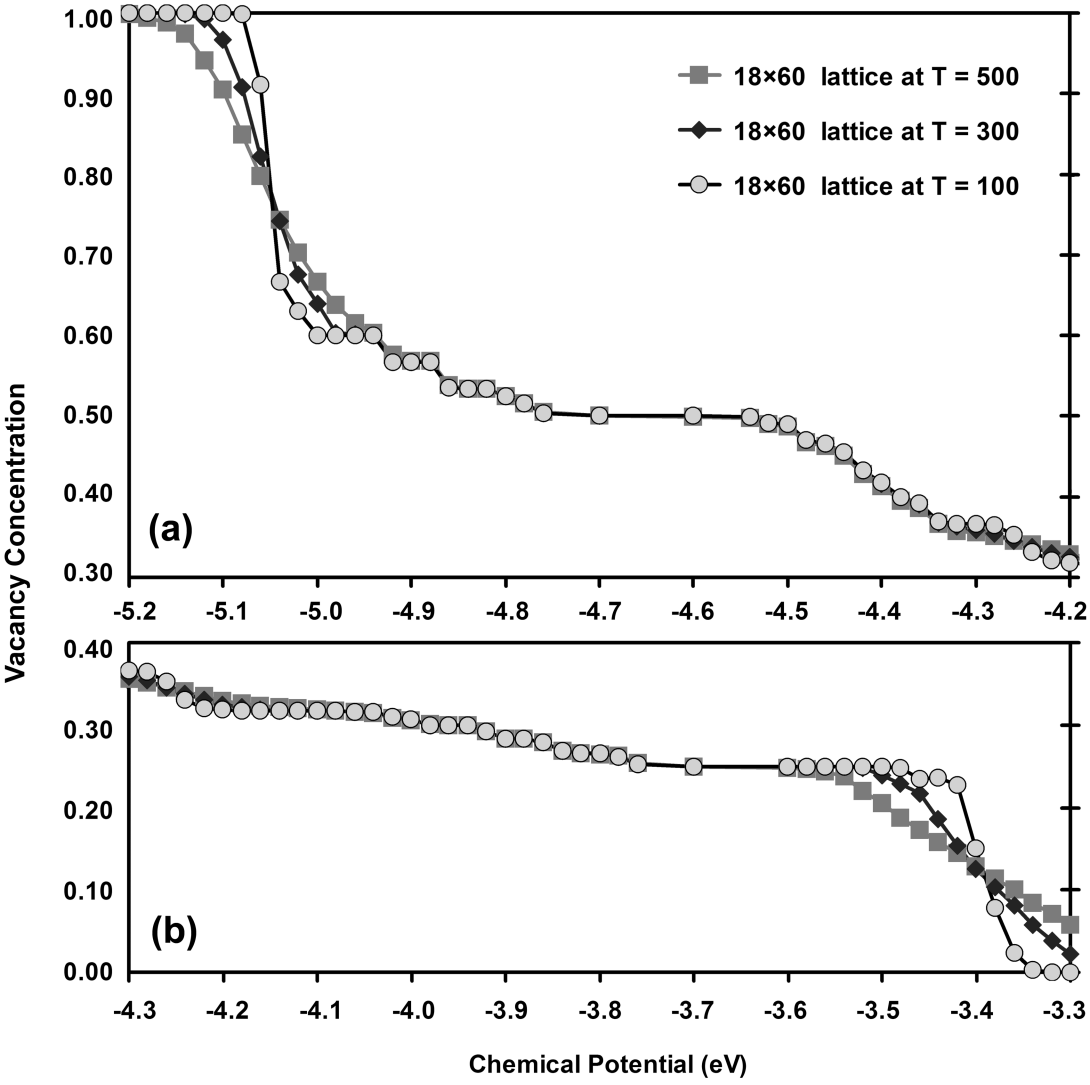

Figure 6.7: Plot of the concentration of bridging O vacancies vs. chemical potential of the surface for three different simulated temperatures using an 18×60 simulation cell. As the chemical potential is increased, the surface progresses from completely vacant at the left of (a) to fully stoichiometric at the right of (b), where a small overlap of chemical potential is included in the two plots. The statistical error bars are smaller than the points in each curve.

A similar plot, figure 6.7, for three different temperatures, using the 18×60 simulation cell, demonstrates that the trend in vacancy concentration over the interesting range of chemical potentials shown is essentially independent of temperature (for the range studied in my simulations). Only the transitions from the fully stoichiometric surface (no vacancies) to approximately 25% vacancy concentration (the right of figure 6.7(b)) and approximately 60% vacancy concentration to the completely vacant surface (the left of figure 6.7(a)) have significant different temperature dependencies over the temperature range investigated. In both cases, the change in vacancy concentration with respect to chemical potential resembles a step function for the low temperature transitions. When the temperature increases, this step function smears out, resulting in a more gradual transition in vacancy concentration.

Both figure 6.6 and 6.7, show that bridging O vacancy concentrations of 25% and 50% are stable over relatively wide ranges (greater than 0.2 eV) of chemical potential, independent of simulation cell size and temperature. As discussed in the following section, these stable phases correspond to ordered vacancy structures on the TiO_2 (110) surface. In addition, two flat regions in vacancy concentration vs. chemical potential are found at low temperature for concentrations of 60% and just under 33%. As discussed in the following section, these correspond to 'quasi-stable' phases.

6.4 Prediction of Ordered Vacancy Configurations

In order to gain insight into the specific types of vacancy patterns that occur over the range of surface chemical potentials studied, I examined representative configurations for the 90×200 simulation cell. As seen in figure 6.6, beginning at a high chemical potential of slightly more than -3.3 eV at 300K, the stoichiometric TiO_2 (110) surface starts to develop more and more bridging O vacancies until a stable 25% concentration is reached at a surface chemical potential of -3.5 eV. Over this range of surface chemical potential, new bridging O vacancies appear on the surface at locations that

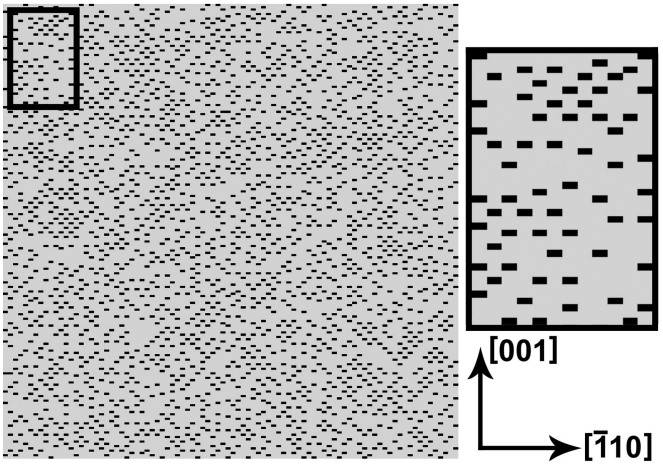

Figure 6.8: A representative image of the TiO_2 (110) surface for a 90×200 cell with a chemical potential of -3.40 eV and a temperature of 300 K. The outlined 12×40 portion is magnified at the right, where dark cells denote the presence of a vacancy.

are isolated from the vacancies already present. This behavior can be seen in figure 6.8, which depicts a sample vacancy arrangement for a chemical potential of -3.40 eV at room temperature. The callout box in figure 6.8 (as well as figures 6.9 - 6.12) shows a magnified 12×40 portion of the surface. A black rectangle denotes a primitive TiO_2 (110) unit cell containing a bridging O vacancy.

Careful study of figure 6.8 reveals that bridging O vacancies do not typically occur in adjoining sites (directly or diagonally) on adjacent [001] bridging O rows, or within less than three sites of each other along a [001] bridging O row. Recall that when fitting the interaction Hamiltonian, I determined that non-negligible pairwise interactions along a [001] bridging O row exist to third-nearest neighbors ($\alpha_{kl} = 6$), and that, for pairs of vacancies in neighboring rows, only first ($\alpha_{kl} = 3$) and second ($\alpha_{kl} = 4$) neighbors have non-negligible interactions. The remaining longer-ranged interactions were found to be either less than or comparable to the error in my DFT calculations

and fit, and are thus negligible in the model. Therefore, in figure 6.8, nearly all bridging O vacancies are isolated from each other (according to the interaction model). This corresponds to the presence of isolated vacancies observed experimentally [38, 39], and predicted theoretically in the previous sections and references [10, 14]. From this point forward, a bridging O vacancy will be referred to as 'isolated' if there are no other vacancies near enough to interact with it according to the model Hamiltonian. Therefore, all other vacancies are either at fifth-nearest neighbor sites or further than sixth-nearest neighbor sites.

Decreasing from a chemical potential of -3.50 eV, the bridging O vacancy concentration remains at 25% until the chemical potential becomes smaller than approximately -3.75 eV. This stable concentration is independent of cell size and temperature, as shown in figures 6.6 and 6.7 respectively. Figure 6.9 shows a set of images of the TiO_2 (110) surface at a chemical potential of -3.65 eV, which is near the center of this stable range. These images clearly indicate that the stable phase at 25% vacancy concentration corresponds to a long-range ordered vacancy pattern on the surface. While defects are seen in these ordered structures, they are due to the finite temperature of the simulations, and diminish in number as the temperature is decreased. Point defects in the ordered vacancy structure are caused by a shift in a vacancy position along the [001] bridging O row or by the absence of a vacancy at a particular site. These defects are fairly abundant at high temperature (500 K), figure 6.9(a), much rarer at room temperature (300 K), figure 6.9(b), and generally nonexistent at low temperature (100 K), figure 6.9(c). Extended defects are also observed at higher temperature. Figure 6.9(a) shows walls between otherwise ordered domains, which differ from each other by a relative shift in the [001] direction.

As observed for cases of lower vacancy concentration, each bridging O vacancy in the 25% ordered arrangement is isolated from all others according to the interaction model. Specifically, the 25% structure spaces vacancies along [001] rows as close as

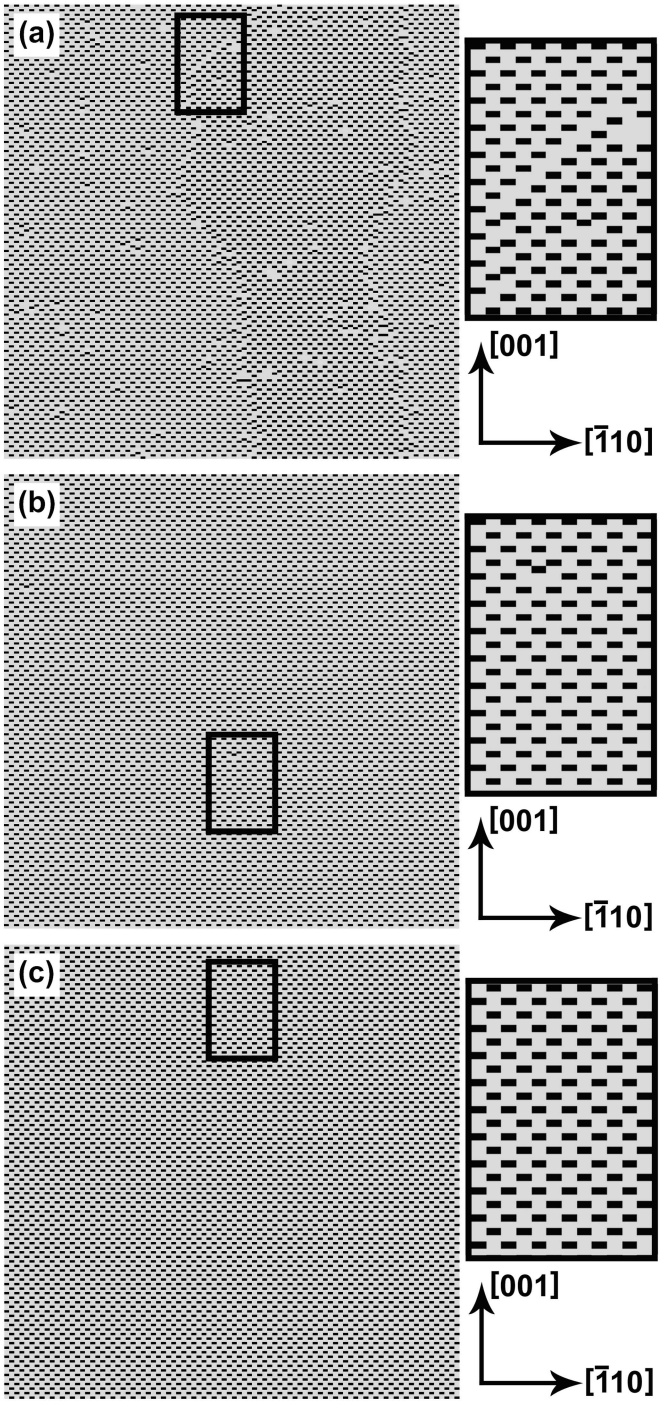

Figure 6.9: Representative images of the TiO_2 (110) surface for a 90×200 cell at 500 K (a), 300 K (b), and 100 K (c). The chemical potential of -3.65 eV yields an ordered arrangement, with a vacancy concentration of 25%, for all three temperatures depicted.

possible without interacting, and staggers adjacent [001] rows so that the vacancies are just out of interaction range. Therefore, this ordered arrangement can be viewed as the closest packed arrangement of effectively non-interacting vacancies.

In addition to predicting the occurrence of an ordered structure of effectively isolated vacancies, the existence of this specific arrangement has major implications for future theoretical studies involving isolated vacancies. The main reason for this is that the ordered vacancy configuration shown in figure 6.9(c) can be described using a 1×4 unit cell with non-orthogonal lattice vectors along the [001] and [$\bar{1}$12] directions, denoted as β in figure 6.1. Previous theoretical investigations modeled isolated vacancies on either a 2×4 orthogonal cell or a smaller 2×3 orthogonal cell [10, 11, 101]. As discussed previously, while smaller and therefore computationally faster than a 2×4 cell, calculations using a 2×3 cell would introduce a small error due to vacancy interactions along [001] bridging O rows. Using the 1×4 non-orthogonal cell to model isolated bridging O vacancies is advantageous since it has a smaller volume and half to two-thirds the number of atoms of the more commonly used unit cells. This allows for a savings of nearly 50% in computational time when modeling isolated vacancies on the (110) surface of TiO_2. Additionally, this unit cell enables the simulation of isolated vacancies on a wider variety of computational platforms, since these calculations require less memory and are able to be completed in a more reasonable time frame. It is interesting to speculate that the use of simulation cells of different symmetry than the primitive unit cell, while not currently a common practice, may enable more efficient modeling for many other systems besides TiO_2 (110), as well.

When the chemical potential drops below -3.75 eV, the stable 25% vacancy arrangement, consisting of staggered rows of vacancies separated by three bridging oxygens along the [001] direction, gradually transforms into a similar configuration where vacancies are separated by two bridging oxygens along the [001] direction, as

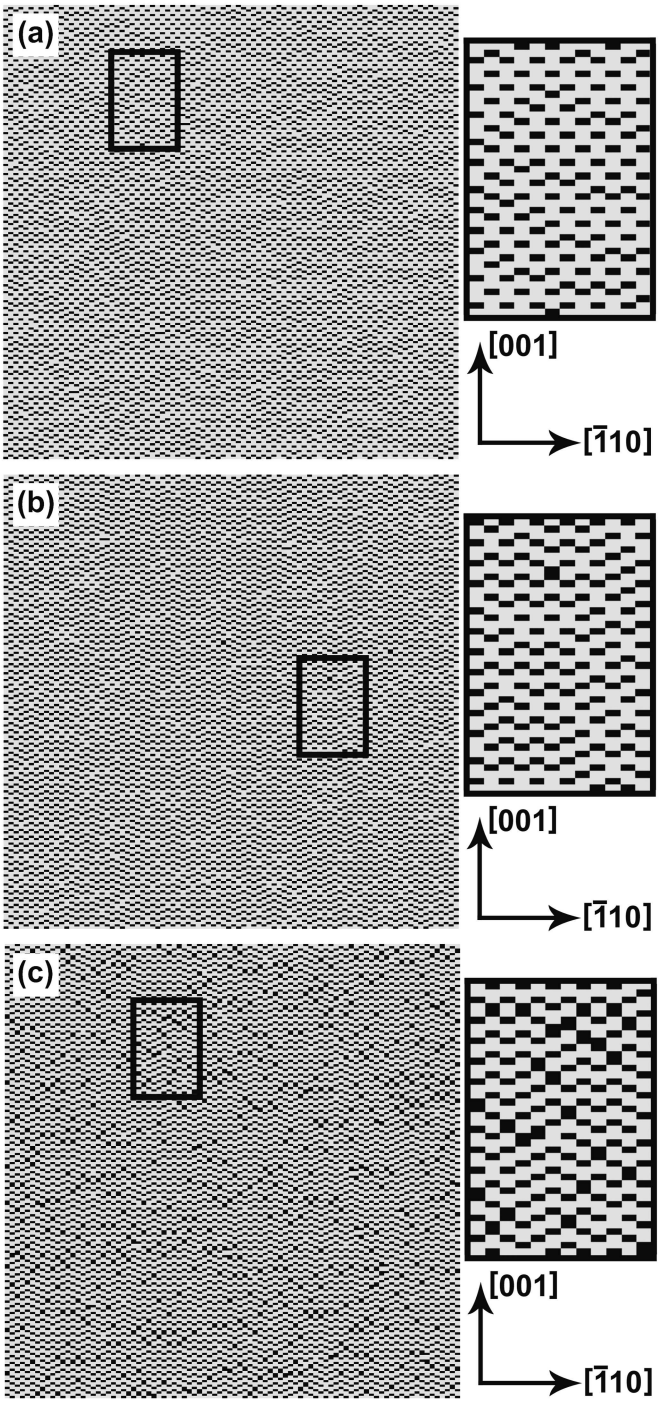

Figure 6.10: Representative images of the TiO_2 (110) surface for a 90×200 cell at a temperature of 300 K. The chemical potentials of -3.90 eV (a), -4.10 eV (b), and -4.30 eV (c), demonstrate how the vacancy pattern changes as vacancy concentration goes from 25% to 50%

shown in figure 6.10(a). While figure 6.6 shows that a seemingly stable concentration is achieved near 33%, an ordered arrangement for this concentration is not obtained, figure 6.10(b). The lack of a long-range ordered pattern for this concentration can be understood by noting that vacancies on adjacent [001] rows can be arranged in two energetically degenerate configurations. Specifically, arrangements with neighboring rows shifted by a site in the positive [001] direction ($N_{[001]} \rightarrow N_{[001]}+1$) are energetically equivalent to those where neighboring rows are shifted by a site in the negative [001] direction ($N_{[001]} \rightarrow N_{[001]}-1$). Therefore, long range order in the [$\bar{1}$10] direction is precluded for this situation. Given the lack of energetic preference in the relative arrangement of adjacent [001] rows, entropic effects dominate, even down to low temperatures. Additionally as the chemical potential is decreased, it becomes energetically favorable for vacancies to arrange themselves such that a small number of vacancy pairs are observed, as seen in figure 6.10(b). Vacancy pairing occurs prior to the surface reaching a vacancy concentration of 33%, and disrupts the order along the [001] direction. As a result, a partially ordered, quasi-stable arrangement is not observed for a vacancy concentration of 33%. As the chemical potential is decreased further still, the pairing of vacancies becomes more frequent, as shown in 6.10(c).

The trend of vacancies pairing together along [001] rows continues until a chemical potential of approximately -4.55 eV is reached, which coincides with the high end of the 0.2 eV range for which the vacancy concentration is stable at 50%. Similar to the stable 25% case, the stable 50% concentration is also independent of cell size and temperature, according to figures 6.6 and 6.7 respectively. Figure 6.11 shows a set of images of the TiO_2 (110) surface at a chemical potential of -4.60 eV, which is within this range. These images clearly indicate that the stable phase at 50% vacancy concentration corresponds to another long-range ordered vacancy pattern on the surface. In this case only point defects, and not extended defects, are observed in this ordered phase, over the range of temperatures studied. As in the 25% ordered phase, these

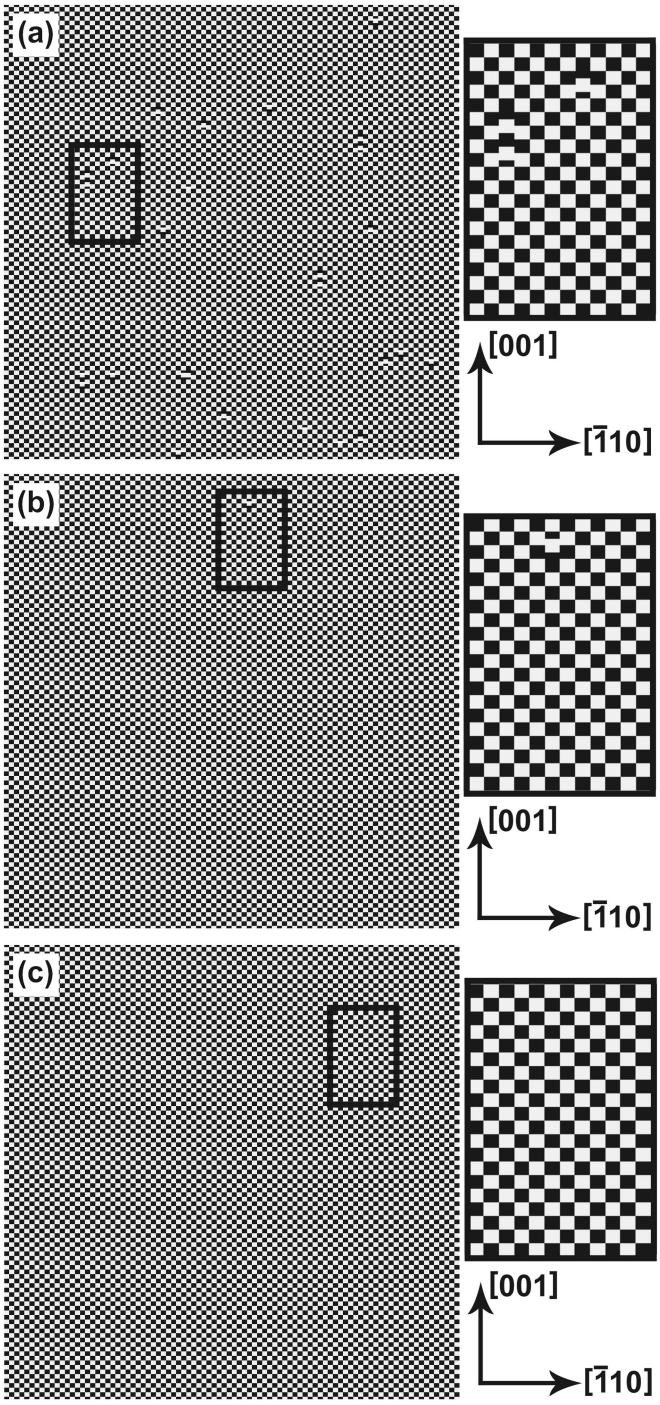

Figure 6.11: Representative images of the TiO_2 (110) surface for a 90×200 cell at 500 K (a), 300 K (b), and 100 K (c). The chemical potential of -4.60 eV yields an ordered arrangement, with a vacancy concentration of 50%, for all three temperatures depicted.

point defects are more abundant at high temperature (500 K), figure 6.11(a), much rarer at room temperature (300 K), figure 6.11(b), and generally nonexistent at low temperature (100 K), figure 6.11(c).

The long-range ordered 50% vacancy structure consists of pairs of vacancies alternating with pairs of bridging oxygens along [001] rows, where adjacent rows are again staggered. This results in the checker-board pattern seen in figure 6.11. This structure can also be explained by referring to the energy coefficients of the interaction Hamiltonian in table 6.2. However, the explanation is not as simple as in the isolated vacancy arrangements. Notice that the first ($\alpha_{kl} = 1$) and second ($\alpha_{kl} = 2$) nearest neighbor pairwise coefficients along [001] rows are both repulsive and similar in magnitude, and the third-nearest neighbor ($\alpha_{kl} = 6$) coefficient along [001] rows is repulsive and much weaker. The pairwise interactions on adjacent [001] rows ($\alpha_{kl} = 3$ and $\alpha_{kl} = 4$) are also repulsive. However, the magnitude of the second-nearest neighbor interaction between vacancies on adjacent [001] rows ($\alpha_{kl} = 4$) is smaller. This suggests that an arrangement of vacancies along [001] rows consisting of a pair of vacancies alternating with a pair of bridging O atoms is nearly equivalent in energy to an arrangement consisting of a single vacancy alternating with a single bridging O, where in both cases, vacancies on adjacent rows are shifted in the [001] direction. This is consistent with the shifting of vacancies on adjacent rows along the [001] direction seen for the 33% vacancy concentration pattern, figure 6.10. Therefore, since the arrangements are energetically similar with respect to the [001] direction, the lowest energy arrangement is the one that minimizes the number of repulsive second nearest neighbor interactions between adjacent [001] rows. The arrangement where vacancies are paired instead of alternating has half the number of these repulsive interactions, so the resulting lowest energy arrangement is the checker-board pattern.

This predicted ordered arrangement has not yet been experimentally observed. However, certain aspects, such as the clustering of vacancies along [001] rows [46] and

ordered configurations at a high vacancy concentration [47, 48], have been observed, and are in qualitative agreement with my predicted structure. Like the ordered 25% arrangement, the 50% ordered vacancy configuration shown in figure 6.11(c) can also be described using the 1×4 non-orthogonal unit cell labeled β in figure 6.1. Therefore, the computational advantages described in the isolated vacancy case also apply when studying the interesting effects of multiple vacancies. For example, as discussed in later chapters, pairs of vacancies significantly effect Cu adsorption on the surface.

These vacancy pairs also have an effect on CO adsorption. Previous theoretical results have shown that CO prefers to bind to the Ti atoms between bridging O rows on the stoichiometric surface, and at the vacant site for a surface containing isolated vacancies [101]. In both cases, the carbon end of the molecule binds to the surface and the CO bond is perpendicular to the (110) plane. My calculations, as discussed below, also find this orientation to be the most energetically favorable. Using the 1×4 non-orthogonal unit cell, I obtain a binding energy of 0.33 eV for CO bound either to the Ti atom between bridging O rows on the stoichiometric surface or the vacancy site on the 25% vacant surface. These results are in reasonably good agreement with those of the previous study, which used an orthogonal 2×2 unit cell to calculate binding energies of 0.29 eV and 0.37 eV respectively [101]. However, on the 50% vacant surface, CO prefers to bind either over one of the vacant sites or directly above the Ti atom between the vacancy pair. In this case, my calculations result in a larger binding energy of 0.67 eV for both locations. Experiments have observed an increase in the desorption temperature for a fraction of the adsorbed CO molecules when in the presence of O vacancies on the surface [99]. The higher binding energy of CO to the surface in the presence of the vacancy pair supports this, as does the much higher calculated binding energies, as large as 1.9 eV, for CO adsorption on surfaces with missing bridging O rows [101].

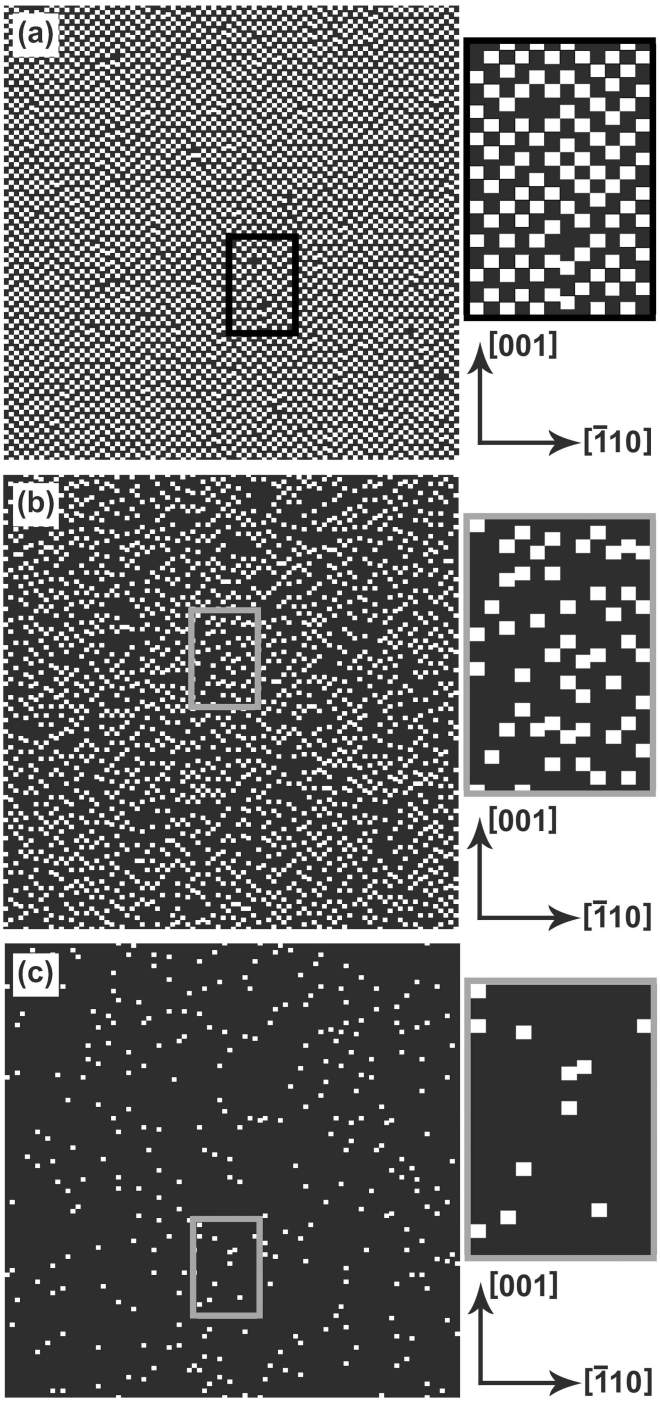

Figure 6.12: Representative images of the TiO_2 (110) surface for a 90×200 cell at a temperature of 300 K. The chemical potentials of -4.95 eV (a), -5.05 eV (b), and -5.10 eV (c), demonstrate how the vacancy pattern changes as vacancy concentration goes from 50% to 100%

The transition from the 50% ordered phase to the completely vacant surface is depicted in figure 6.12. As the chemical potential decreases to -4.95 eV, a second quasi-stable phase is reached. Near a vacancy concentration of 60%, figure 6.12(a), vacancies are seen to group into triplets along the [001] direction. The combination of paired bridging oxygens followed by three vacancies along the [001] direction would lead to a semi-ordered configuration of 60% vacancy concentration. However, similar to the 33% case, such a [001] row pattern is equally favored to be shifted up two sites as down two sites, relative to adjacent [001] rows, thus preventing long-range order in the $_{[\bar{1}10]}$ direction. Additionally, the 60% configuration is only achieved at low temperatures and over a very small (0.02 eV) range of chemical potential, since a small drop in chemical potential results in the grouping of additional vacancies in excess of three along the [001] rows, as seen in figure 6.12(b).

A second interesting feature, as seen in figure 6.12, is that the bridging oxygens remain paired together along [001] rows. In fact, even at a chemical potential of -5.10 eV, figure 6.12(c), where the surface is almost completely vacant, unpaired bridging oxygens are not observed for any of the configurations. To understand this, let's examine the interaction coefficients in table 6.2. The coefficient for the 3-body interaction involving a triplet of vacancies along the [001] bridging O row ($\beta_{klm} = 1{,}2$) is attractive and substantial in magnitude. This suggests that the vacancies would prefer to group together along rows when the vacancy concentration is high. However, this does not completely describe the pairing of the few remaining bridging O atoms. Recall that the present model Hamiltonian was developed from the point of view of interacting bridging O vacancies, and therefore, is not expected to easily describe the behavior of the bridging O atoms themselves. However, as mentioned in the previous section, this interacting-vacancy model is equivalent to a lattice gas model of bridging O atoms relative to a fully vacant surface. While direct application of this lattice gas

model [104, 105] is unphysical for TiO_2 (110), it does provide insight into the pairing behavior of bridging O atoms, as mentioned above.

Using the same DFT data (table 6.1) used to parameterize the vacancy interaction Hamiltonian, I can parameterize a bridging O interaction Hamiltonian, treating the bridging O atoms as if they were adsorbates on the otherwise fully vacant surface. In this case, σ_k in equation 6.2 is now 1 for an adsorbed bridging O and 0 for a vacancy, and the binding energies of O atoms on the 100% vacant surface are calculated using equation 6.5. A least-squares fit of these average O binding energies are used to parameterize the bridging O interaction Hamiltonian, where the resulting energy coefficients are listed in table 6.4. The energies calculated using this interacting bridging O model were found to be in good agreement (within 1.2%) with the DFT calculated values, as expected, since the equivalent models were formed in the same fashion.

$$BE_V = E_{100\%vac} - E_{def} + \frac{1}{2}E_{O_2} \tag{6.5}$$

While no truly new information is provided in this representation, the pairing of bridging oxygens along [001] rows on an otherwise vacant surface can easily be explained from the coefficients listed in table 6.1. Other than the one-body on-site term (c), the coefficient for nearest-neighbor ($\alpha_{kl} = 1$) interactions along the bridging O rows is the only attractive term. This explains why bridging O atoms are observed to pair together along [001] rows for all vacancy concentrations as seen in figures 6.8 - 6.12. Additionally, this result agrees with experimental observations of an ordered 67% configuration in which all bridging O atoms were paired [47, 48].

In general, the trends in vacancy concentration and patterns with decreasing chemical potential, shown in figures 6.6 - 6.12, can be described in two ways. On the one hand, the system can be viewed in terms of the vacancies, which are isolated at low

Table 6.4: The coefficients for a lattice gas model of interacting bridging O atoms composed of isolated, 2-body, and 3-body interactions, as specified in equation 6.2 and described in the text, are listed in units of eV. The statistical errors for the fitting procedure are given in parenthesis.

Energy Coefficients (eV)		
c		-4.93(1)
α_{kl}	1	-0.30(2)
	2	0.21(2)
	3	0.04(1)
	4	0.04(1)
β_{klm}	1,2	0.42(2)

concentrations. As the chemical potential decreases, the corresponding increase in vacancy concentration results initially in the pairing and eventually higher-order clustering of vacancies until a surface devoid of bridging oxygen atoms is achieved. Alternatively, one can view the system from the perspective of the bridging oxygen atoms, which show a consistent preference to be surrounded by other bridging oxygen atoms within their local neighborhood. As the concentration of vacancies increases, the bridging oxygen atoms remain clustered together in pairs (at a minimum) for as long as possible, until eventually 100% vacancy concentration is approached. Both of these views are equivalent and consistent with previous theoretical [10, 14, 24, 36, 38, 43–45, 101] and experimental [38, 39, 46–48] work.

Chapter 7

Adsorption of Copper on the TiO_2 (110) Surface

7.1 Isolation of Adsorbed Cu on the Periodic Surface

As discussed in Chapter 2, experiments have shown that the catalytic properties of TiO_2 are often greatly enhanced when a metal (such as Pt, Ag, Au, and Cu) is adsorbed on the (110) surface [1, 3, 4]. While significant theoretical work has been done regarding the effects of adsorbed Pt and Au atoms [10–14, 16, 64], as well as Au nanoclusters [15, 65], fewer studies have focused on the addition of Cu to the surface and the role that it may play in catalysis [14, 64, 66]. Cu adsorption on TiO_2 is of particular interest due to the wide variety of experimentally observed formations that appear on the (110) surfaces. Specifically, Cu atoms have been shown to cluster together into trimers at very low concentration [50] and 3-D islands at higher concentrations [47, 48, 51–55]. Moreover, experiments suggest that the growth modes and maximum size of these Cu islands depend on the structure of the TiO_2 surface, and, in particular, the presence of bridging O vacancies [47, 52, 54, 55]. In order to develop an understanding of Cu nanocluster formation and island growth, it is important to first have a detailed understanding of the binding and diffusive characteristics of Cu atoms when adsorbed on the TiO_2 (110) surface.

In some ways, investigating the interactions of Cu atoms (and clusters) with the TiO_2 (110) surface is similar to studying bridging O vacancies. In particular, a primary focus of the calculations involving Cu is determining the binding energy, which, like the vacancy formation energy, is found by calculating an energy difference. As

described in the previous chapter, when focusing on energy differences, certain computational parameters can be modified to reduce the time required for the calculation while maintaining the precision of the calculated energy difference. In particular, these calculations can also be done using a PREC setting of Normal and real space projection operators [9]. The binding energy of Cu is determined (in eV) using equation 7.1, which involves the difference in energy between the bare TiO_2 surface and a surface with an adsorbed Cu atom. When calculating the binding energy of Cu to the TiO_2 surface, Cu is assumed to exist in atomic form (instead of nanoclusters or crystals) so that individual atoms are freely available to adsorb on the surface without having to first dissociate from a Cu structure. Therefore, the binding energy of Cu would only depend on the energy difference mentioned above, if the calculational method used did not require a correction term. However, to account for the energy difference between the electronic configuration of the Cu atom used to generate the pseudopotential (electron spin not included) and the actual experimental ground-state electronic configuration of Cu, a correction factor of magnitude 0.22 eV per atom is required. Further explanation can be found in reference [9].

$$BE_{Cu} = E_{bare\ surface} - (E_{Cu\ on\ surface} + 0.22N_{Cu}) \tag{7.1}$$

Recall that when calculating the formation of bridging O vacancies, additional sampling of the Brillouin zone beyond that used for the bare TiO_2 (110) surface was required. Therefore, the energy convergence related to the k-point grid used was retested for CU adsorption. Unlike the vacancy investigations, I determined that (for the primitive 1×1 surface unit cell) a $2 \times 4 \times 2$ Monkhorst-Pack [84] k-point set continued to give well converged energy values for the adsorption of Cu atoms to many high symmetry sites on the surface. A reduction of the size of the Brillouin zone as the unit cell increases allowed me to use a smaller $2 \times 2 \times 2$ Monkhorst-Pack

[84] k-point set for all larger unit cells. The resulting error due to finite Brillouin zone sampling is on the order of 10 meV, which is comparable to the errors from the other computational approximations mentioned previously.

The adsorption of Cu (or any other adsorbate) has a penetrating effect on structure of the TiO_2 surface. While experiments suggest that Cu has a weak interaction with the TiO_2 (110) surface [54, 68], care must be taken to ensure that the calculations remain converged with respect to slab thickness. As shown in table 5.4, the binding energy of Cu is well converged with respect to slab thickness for the 4(2) slab. This is expected, since the penetrating effects of Cu on the surface structure are much less significant than those that result from the formation of a bridging O vacancy. Therefore, a 4(2) slab can be used to study the adsorption of Cu

Unlike the formation of a bridging O vacancy, which only occurs at specific location (bridging O sites) on the (110) surface, Cu can, in principle, be adsorbed at any point on the surface. Experimental and theoretical results indicate that Cu atoms prefer to bind to bridging O atoms [14, 50, 64]. To ensure that my simulations give comparable results before proceeding to the study of Cu diffusion and clustering, I investigated the binding energy of Cu at four high symmetry position on the surface for a variety of unit cells. Specifically, I placed a Cu atom above the bridging O atom (labeled 1 in figure 5.1), the six-coordinated Ti atom (labeled I in figure 5.1), the five fold coordinated Ti atom (labeled II in figure 5.1), and between the planer O atoms (labeled 2 and 2^* in figure 5.1). In each case, the atoms in the TiO_2 slab and the position of the Cu were allowed to relax to the lowest energy configuration. However, the symmetries of the model precluded the Cu atoms from moving in the [001] or $[\bar{1}10]$ direction, i.e., along the (110) surface. Calculations, for the Cu locations listed above, were performed on several different unit cells to study the effect of Cu-Cu interaction. The resulting binding energies are listed in table 7.1, where the trends of the energies with respect to Cu location and the separation of Cu from its periodic

Table 7.1: The binding energies of Cu atoms (in eV) have been calculated, using equation 7.1, for the adsorption of Cu at the listed high symmetry sites on the TiO_2 (110) surface. All unit cells are built from the primitive orthogonal surface unit cell (α in figure 6.1) except the 1×4 non-orthogonal cell* (β in figure 6.1).

Binding Energy of Cu atom (eV)				
	Location on Surface			
Unit Cell	6-Fold Ti	Bridging O	5-Fold Ti(5)	Between Planer O's
1×1	1.46	1.62	1.20	1.24
1×2	1.61	1.01	0.41	0.43
1×3	1.73	1.10	0.45	0.51
1×4	1.76	1.13	0.44	0.50
2×3	1.79	1.14	0.45	0.52
1×4*	1.76	1.13	0.43	0.50

images (unit cell size) are in agreement with experimental and theoretical findings [14, 50, 64].

In addition to demonstrating general agreement with experimental and theoretical work, the results listed in table 7.1 provide information on an aspect that is important to the general study of adsorbates on a surface using periodic unit cells. Specifically, when Cu atoms are adsorbed on the (110) surface, two types of interactions must be accounted for. First, there are direct interactions between adsorbed Cu atoms, either due to the periodicity of the unit cell, or the adsorption of multiple atoms on a single unit cell. Second, there is an overlap of successive interactions between the adsorbed Cu atoms and the surface. This second type of interaction occurs because an adsorbed Cu atom has a local effect on the structure of the TiO_2 surface. The range of this effect depends on where the Cu atom is adsorbed, and can extend further than any direct Cu-Cu interactions. When multiple Cu atoms are adsorbed such that these

Cu-surface interactions overlap, the structure of the surface changes, relative to the structure seen for the adsorption of an isolated Cu atom. Therefore, the calculated Cu binding energies for multiple Cu adatoms would differ from those where the Cu atoms are truly isolated from each other. The nearly identical binding energies of Cu (within the errors of the DFT calculations) on the orthogonal 1×3, 1×4, and 2×3 unit cells demonstrate that a single Cu atom adsorbed on any of these cells is effectively isolated from its periodic image in neighboring cells. Therefore, the different binding energy for the smaller unconverged unit cells is due to some combination of the above mentioned interactions. Additionally, in agreement with the results for isolated bridging O vacancies discussed in the previous chapter, an isolated Cu adatom can also be modeled using the 1×4 non-orthogonal unit cell.

Table shows that when Cu atoms are adsorbed on the 1×2 unit cell, the binding energy at a given location is similar in magnitude to that calculated for larger unit cells with the same location of Cu on the surface. In this case, the highest binding energy is found for a Cu adatom located over a six-fold coordinated Ti atom. This occurs since the Cu is located in between and bound to two bridging O atoms on a [001] bridging O row. For this unit cell, the Cu adatom is separated from its closest periodic image by 5.94 Å. This relatively large Cu-Cu separation suggests that the interaction between adsorbed Cu atoms is largely due to the overlap of successive interactions between the adsorbed Cu atoms and the TiO_2 surface.

When a 1×1 primitive unit cell is used, the Cu-Cu separation due to the periodicity of the unit cell is reduced to 2.97 Å, which is not much larger than the experimental 2.55 Å Cu-Cu bond length for bulk fcc Cu [56]. Therefore, both the Cu-Cu interactions and the overlap of Cu-surface interactions are present for this relatively small unit cell. The Cu-Cu interactions account for the significantly higher Cu binding energies for this unit cell for the two binding sites between [001] bridging O rows (over the five-fold coordinated Ti atom and between the planer O atoms), as seen in table 7.1.

While a preference for Cu adsorption along the [001] bridging O rows is still observed, the highest binding energy for this unit cell now occurs when Cu is adsorbed over a bridging O atom. This behavior is largely due to the overlap of Cu-surface interactions. Specifically, for this small unit cell, there is one bridging O atom for each adsorbed Cu atom, whereas the larger unit cells listed in table 7.1 have at least two bridging O atoms along a [001] row for each Cu atom. Therefore, a single bond Cu-O bond, where Cu sits over and binds to the bridging O atom, is energetically favorable in this small unit cell.

The results listed in table 7.1 indicate that an isolated Cu adatom (i.e., in larger unit cells) prefers to bind between two bridging O atoms, over the six-fold coordinated Ti atom. However, this location may not be the absolute preferred binding site for a Cu adatom. For example, studies on Au and Pt have shown that these metals prefer to bind to both the bridging O atom and the five-fold coordinated Ti atom [10–14, 16]. In particular, the preferred location for Au and Pt is in the so-called four-fold hollow location, which is approximately in the center of a rectangle formed by two six-fold coordinated Ti atoms and two planer O atoms, such that the adsorbed atom is between the bridging O and the five-fold coordinated Ti. On the other hand, studies on Cu and Ag indicate that the preferred binding site is, as indicated in table 7.1, between two bridging O atoms [14, 64]. To ensure that I have found the optimal binding site for Cu on TiO_2 (110) requires additional calculations that sample more surface sites. Additionally, the data in table 7.1 tell us nothing about Cu adatom diffusion or substrate structural relaxations as a function of Cu position. Both of these factors are needed to study and explain the clustering of Cu atoms and the growth modes of Cu islands.

7.2 Potential Energy Surfaces for Cu on TiO_2

In order to address the three issues mentioned at the end of the last section, I fully mapped out the Cu-TiO_2 interaction energy as a function of in-plane Cu position. I did this for each of the three unit cells, 1×1, 1×2, and 2×3, with the last one included to ensure that Cu-Cu interactions due to periodicity are truly negligible. At this point, it is convenient to redefine the origin of the primitive unit cell to be at the six-fold coordinated Ti atom, as shown in figure 7.1, for visualization of the Cu-TiO_2 potential energy surface. Obtaining a good representation of this potential energy surface requires sampling many different locations on the surface. A single potential energy value is obtained by fixing the coordinates of the Cu adatom parallel to the surface and performing a total-energy DFT calculation, allowing the substrate atoms and the position of the Cu atom perpendicular to the surface to relax into their lowest energy configurations. The interaction potential energy is just the negative of the binding energy, equation 7.1. Generating a detailed map of the potential energy surface requires numerous total energy calculations, each of which is a very time consuming process. Fortunately, the symmetries of the unit cells can be used to minimize the number of total energy calculations.

Two mirror planes perpendicular to the (110) surface permit me to restrict the sampling region to $\frac{1}{4}$ of the primitive 1×1 unit cell, in mapping out the Cu-TiO_2 potential energy surface. As shown in figure 7.1(a), one mirror is perpendicular to [001] and passes through five-fold coordinated Ti atoms. The other, figure 7.1(b), is perpendicular to $[\bar{1}10]$ and passes through five-fold coordinated Ti atoms. Therefore, a single total energy calculation for a Cu atom placed in one representative quadrant of the unit cell will provide a potential energy value at points in the three other quadrants. Due to the combination of the above mentioned symmetries with the allowed translations of the crystal, calculations on larger unit cells can also be confined to this small area of the surface. As a result, a single total energy calculation typically

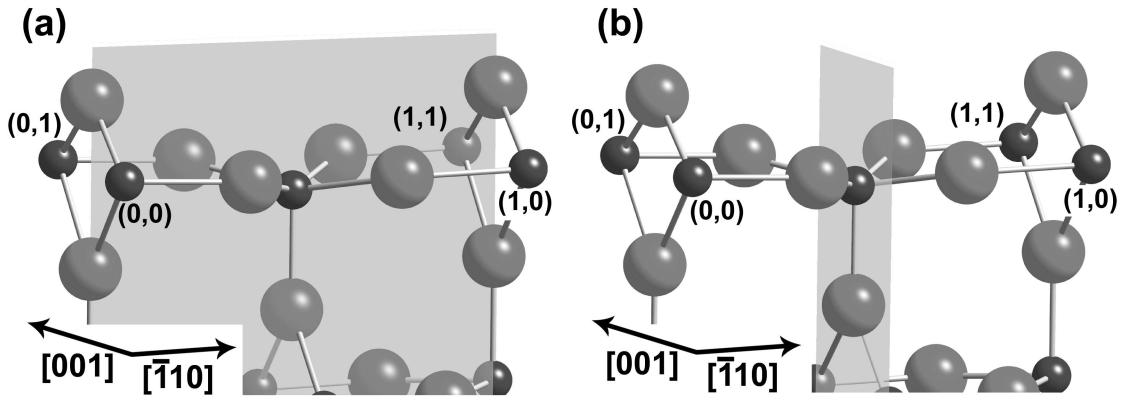

Figure 7.1: A ball and stick model of the primitive surface unite cell defined such that the surface six-fold coordinated Ti atom is at the origin. O (Ti) atoms represented by large, light (small, dark) spheres. The mirror planes used to reduce the computational cost of producing the Cu-TiO_2 potential energy surface are shown in parts (a) and (b).

gives potential energy values for 8 and 24 locations on the 1×2 and 2×3 unit cells respectively.

In this manner, I computed potential energy surfaces by performing 77 (66) DFT calculations for evenly spaced points between 0 and 0.5 in both the [$\bar{1}$10] and [001] directions on the 1×1 (1×2 and 2×3) unit cell. Unfolding this data to the full unit cell gives the potential energy at a total of 273, 441, and 1271 evenly spaced grid points on the 1×1, 1×2, and 2×3 unit cells respectively. Even though the potential energy has been computed for a large number of points in the unit cell, on the atomic scale, the spacing between the points where calculations were done is still relatively large (on the order of 0.25 Å). To obtain a smooth potential energy surface, I fitted these data to a functional form.

The periodicity, mirror symmetries, and choice of cell origin all suggest a 2-D Fourier cosine series for the functional form of the Cu-TiO_2 potential energy surface,

shown in equation 7.2. In this equation the position of the Cu atom on the surface is specified by x, and L corresponds to the lattice constants of the primitive unit cell. For each of the three unit cells studied, a good fit (errors on the order of the DFT precision) of the calculated energies was obtained when the summations were truncated after a small number of terms. Specifically, the summations were truncated when the magnitude of the fitted coefficients became smaller than the precision of my DFT energy calculations, 10 meV. In all cases, the statistical error of the energy coefficients due to the fitting procedure, are an order of magnitude smaller. The values of the energy coefficients for the non-truncated terms are listed in table 7.2 for three unit cells studied.

$$U(x_{[\bar{1}10]}, x_{[001]}) = \sum_{n,m=0}^{\infty} a_{nm} \cos(\frac{2\pi n x_{[\bar{1}10]}}{L_{[\bar{1}10]}}) \cos(\frac{2\pi m x_{[001]}}{L_{[001]}}) \tag{7.2}$$

Potential energy surfaces for Cu atoms adsorbed on TiO_2, plotted using equation 7.2 with the coefficients listed in table 7.2, are shown in figures 7.2, 7.3, and 7.4 for the 1×1, 1×2, and 2×3 unit cells respectively. For each surface, the labeled positions on the $[\bar{1}10]$ and [001] axis are given in lattice coordinates, where (0,0) corresponds to the position of a six-fold coordinated Ti atom. Additionally, a density plot is shown below the surface, and the color coded energy scale (to the right) applies to both the density plot and the 3-D surface. Figures 7.2-7.4 show that specifying the surface by a small number of basis functions (cosine products) provides a smooth potential energy surface for all locations on the TiO_2 (110) plane that is in good agreement with the DFT total energy calculations, as discussed above.

These Cu-TiO_2 potential energy maps make it possible to address the issues raised near the end of the previous section. Specifically, information is now available to definitively identify the preferred binding site of Cu atoms, obtain a detailed understanding of the diffusion of Cu atoms for high and low concentrations of adsorbed Cu,

Table 7.2: The coefficients for equation 7.2, of the fitted Cu-TiO_2 potential energy surface are given for adsorption onto the 1×1, 1×2, and 2×3 periodic unit cells. The statistical fitting errors are on the order of 1 meV.

Energy Coefficients (eV)			
	Unit Cell		
Coefficient	1×1	1×2	2×3
a_{00}	-1.37	-0.97	-1.09
a_{10}	-0.15	-0.34	-0.41
a_{20}	0.03	0.16	0.20
a_{30}	-0.02	-0.05	-0.04
a_{40}	-	-0.01	-0.04
a_{01}	0.06	-0.12	-0.13
a_{02}	-	-0.02	-0.03
a_{11}	0.06	-0.18	-0.18
a_{21}	-0.04	-0.04	-0.06
a_{31}	0.01	0.05	-0.07
a_{12}	-	-0.07	-0.04
a_{22}	-	-0.02	0.06

and provide insights into the interactions between the TiO_2 surface and an adsorbed Cu atom.

These three figures show that the preferred high symmetry sites identified in table 7.1 are indeed the globally preferred sites. Specifically, figure 7.3 and 7.4 clearly show that the lowest potential energy (highest binding energy) occurs when Cu atoms are in between two bridging O atoms along the [001] bridging O row. Both of these unit cells represent a relatively low concentration (25% for the 1×2 unit cell and 8% for the 2×3 unit cell) for adsorbed Cu, where the concentration is determined by the number of Cu atoms per TiO_2 formula unit. For a larger (50%) coverage of Cu, as shown in figure 7.2 for the 1×1 cell, the lowest potential energy is achieved for Cu atoms directly above the bridging O atoms. The results from all three unit cells agree with experiments, which indicate a preference for Cu to bind to the bridging O atoms [50]. At low concentrations Cu binds to two bridging O atoms, and at high concentration to one. Additionally, my calculations confirm previous theoretical results showing that Cu, like Ag, prefers to bind along the [001] bridging O rows [14, 64], instead of four-fold hollow sites like Au and Pt [10–14, 16].

Figures 7.2-7.4 show that, for all three Cu concentrations studied, there is a large potential energy barrier for Cu diffusion between adjacent [001] bridging O rows. While the height of this barrier, as measured relative to the potential energy minimum, does vary in magnitude, it remains significant for all three Cu concentrations. Low concentrations (8% and 25%) of adsorbed Cu have a larger diffusion barrier of approximately 1.2 eV, as shown in figures 7.4 and 7.3. Increasing the Cu concentration ultimately reduces the barrier to approximately 0.5 eV, as seen in figure 7.2 for a Cu coverage of 50%. This reduction is due to the significant Cu-Cu interactions present on the 1×1 unit cell, where the periodic adsorbed Cu atoms are only 2.97 Å apart.

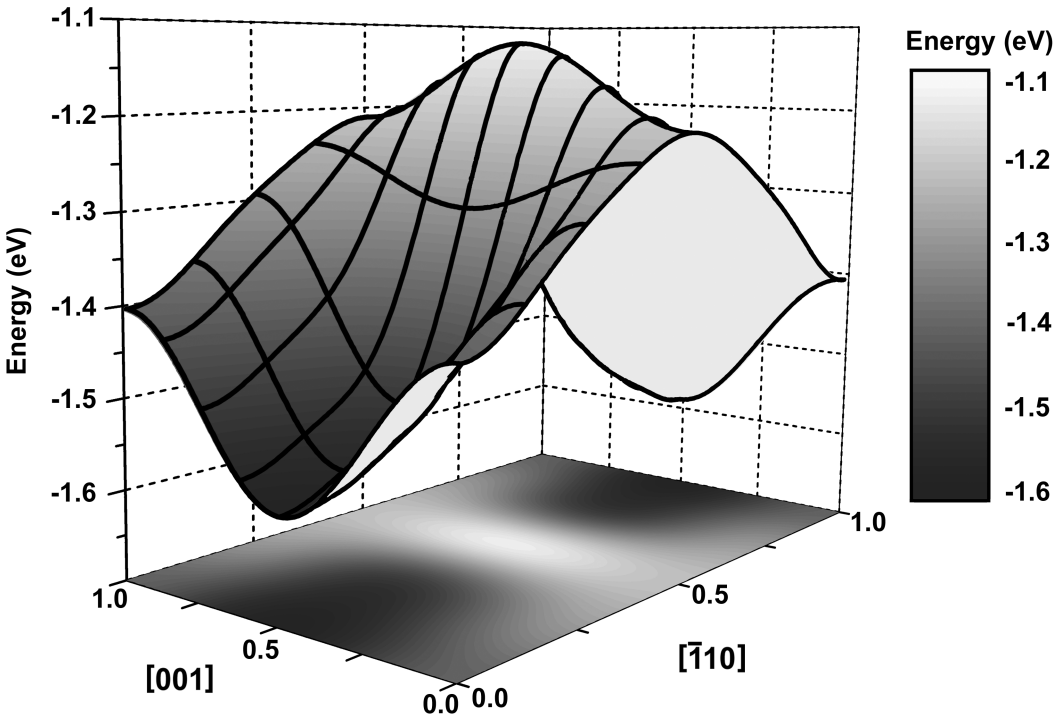

Figure 7.2: The Cu-TiO_2 potential energy surface for the primitive 1×1 unit cell. The (0,0) location corresponds to a six-fold coordinated Ti atom, and in-plane axis are given in lattice coordinates. A density plot is shown below the 3-D representation of the surface. The color coded energy scale, on the right, applies to the density and 3-D plots.

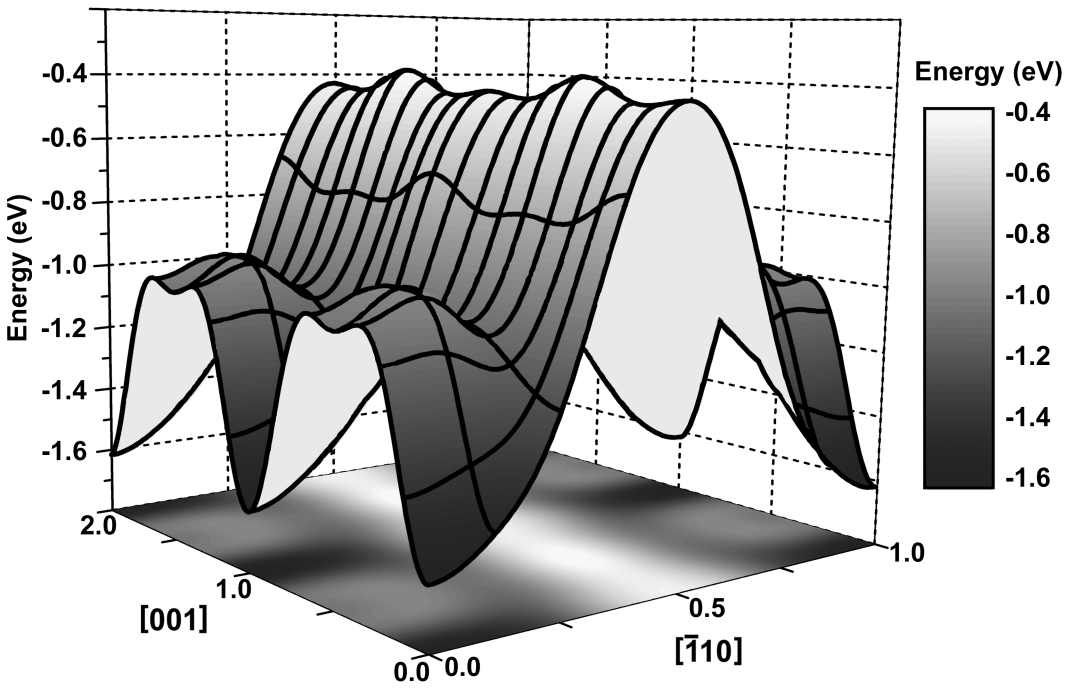

Figure 7.3: The Cu-TiO_2 potential energy surface for the 1×2 unit cell. The (0,0) location corresponds to a six-fold coordinated Ti atom, and in-plane axis are given in lattice coordinates. A density plot is shown below the 3-D representation of the surface. The color coded energy scale, on the right, applies to the density and 3-D plots.

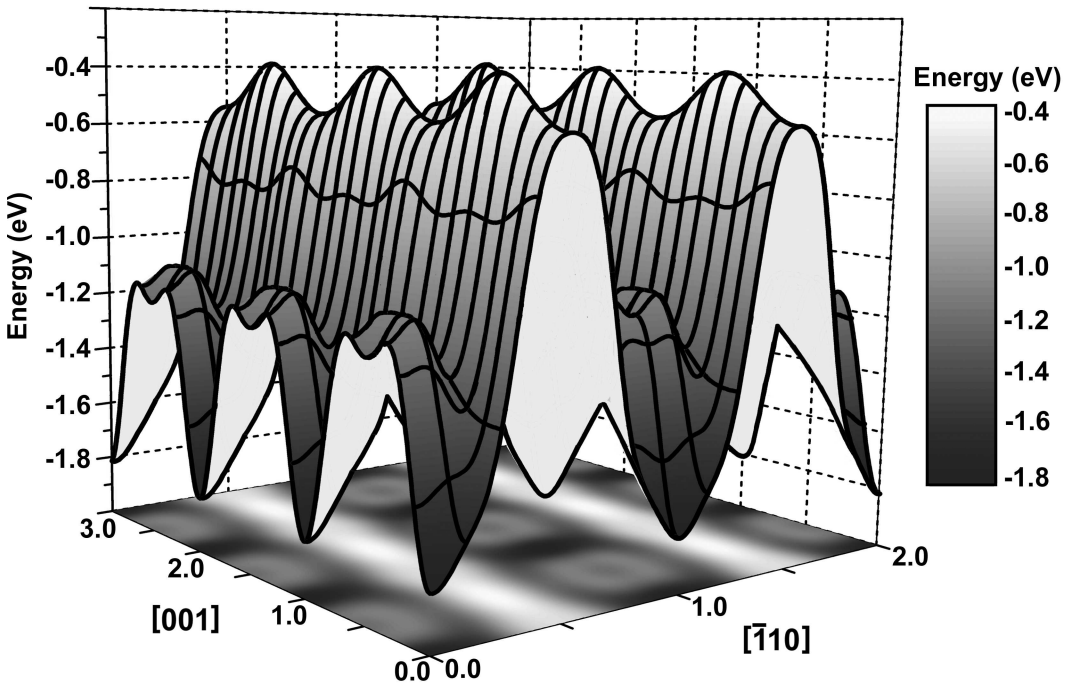

Figure 7.4: The Cu-TiO_2 potential energy surface for the 2×3 unit cell. The (0,0) location corresponds to a six-fold coordinated Ti atom, and in-plane axis are given in lattice coordinates. A density plot is shown below the 3-D representation of the surface. The color coded energy scale, on the right, applies to the density and 3-D plots.

The large magnitudes of all of these energy barriers demonstrate that it is unlikely for adsorbed Cu atoms to diffuse along the surface in the [$\bar{1}$10] direction, i.e., between adjacent bridging O rows. Therefore, diffusion of Cu ad on TiO_2 (110) is primarily along the [001] bridging O rows. As seen in figures 7.2-7.4, the likelihood for Cu atoms to diffuse along these rows is largely dependent on the concentration of Cu. For low concentrations of Cu ($\leq 25\%$), Cu atoms prefer to bind to two bridging O atoms, and any diffusion (or transport) along the [001] rows results in the breaking of one of these bonds. This results in a significant potential energy barrier of approximately 0.6 eV along the [001] direction. Thus, Cu diffusion in this direction is effectively precluded for both the 25% (figure 7.3) and 8% (figure 7.4) Cu concentrations at experimentally relevant temperatures. When the concentration of adsorbed Cu is increased to 50%, due to the periodicity of the unit cell, each Cu atom prefers to bind to only a single bridging O atom. In this case, as seen in figure 7.2, the potential energy barrier for the diffusion of the resulting chain of Cu atoms along the [001] bridging O rows is much smaller, only 0.2 eV.

As discussed above, adsorbed Cu atoms are confined to diffuse in the [001] direction, which is similar to the diffusion characteristics of Ag and Pt [12, 14]. While the potential energy barriers that restrict Cu transport in all directions are nearly identical to those seen by Ag [14], they are significantly higher than the barrier seen by Au or Pt adatoms [11, 14]. Calculations show that Pt has a 0.95 eV barrier to diffusion in the [$\bar{1}$10] direction, but a much smaller 0.13 eV barrier for diffusion in the [001] direction [11]. Whereas Au possesses a much flatter potential energy surface, with calculated barriers of only 0.17 eV and 0.2 eV for diffusion in the [$\bar{1}$10] and [001] directions respectively [11]. Therefore, the diffusion of Au and Pt adatoms on the (110) surface of TiO_2 is much more favorable than for Cu and Ag adatoms.

In addition to providing information on the potential energy barriers that restrict the mobility of adsorbed Cu atoms, the shapes of the potential energy surfaces give

insights into the relative strength of interactions between Cu and the TiO_2 surface. Experimentally, adsorbed Cu atoms have been shown to interact weakly with the surface [54, 68], and this is confirmed by the results shown in figures 7.2-7.4. Specifically, I will focus on the potential energy surfaces in figures 7.3 and 7.4, since the surface obtained using the 1×1 primitive unit cell (figure 7.2) includes the large effects of direct Cu-Cu interactions due to the periodicity of the unit cell.

The first indication that the Cu-surface interactions are relatively week is obtained by comparing the potential energy surfaces in figures 7.3 and 7.4. While the potential energy surface shown in figure 7.4 is obtained using a much larger (2×3) unit cell (smaller concentration of Cu), the shape is nearly identical to the one obtained using the smaller (1×2) unit cell, figure 7.3. This demonstrates that relaxations of the surface atoms are primarily confined to the vicinity of the adsorbed Cu atom, and do not extend significantly outward along the surface. For example, when a Cu atom is adsorbed between two bridging O atoms on the 1×2 and 2×3 unit cells, significant structural relaxations are only observed for the six-fold coordinated Ti atom and two bridging O atoms nearest the Cu adatom. Outside of this local vicinity, the relaxed surface bonds differed by less than 0.02 Å, which is on the order of the precision of the calculations.

Another indication of the interaction strength between the TiO_2 surface and a Cu adatom can be found in the characteristics of the minima of the potential energy surface. Assume that the adsorbed Cu atom is once again in it preferred location, along the [001] bridging O row, between a pair of bridging O atoms. As seen in figures 7.3 and 7.4, the sides of this potential energy well in the [001] direction are very steep. Even a small, 0.15 Å, displacement of the Cu atom along the [001] bridging O row results in a relatively large, 0.1 eV, increase in the potential energy. Calculations further show that a small displacement of the Cu atom in the [001] direction, parallel to a bridging-O row, causes the two bridging O atoms to which it is bound to displace

with it in an effort to maintain the Cu-O bond length. As the displacement of the Cu atom along [001] continues, the bond between the surface and the bridging O atoms does not allow them to continue following the Cu atom, which results in the breaking of one of the Cu-O bonds. This provides two pieces of information regarding the interactions between Cu and the surface. First, it is apparent that the bonds between the bridging O atoms and the six-fold coordinated Ti atoms in the surface are much stronger than the bonds between the bridging O atoms and the adsorbed Cu atom. Second, even small displacement of a bridging O atom in the [001] direction introduces a significant stress on the surface.

A similar result occurs for the displacement of a Cu atom in the $[\bar{1}10]$ direction, perpendicular to a bridging-O row. When the Cu adatom is displaced from its preferred position, the bridging O atoms that are bound to it displace with it in order to maintain Cu-O bond lengths. However, as seen in figures 7.2-7.4, the corresponding potential energy minima are much broader along the $[\bar{1}10]$ direction. In contrast to the results discussed above regarding displacements in the [001] direction, small displacements of the bridging O atoms in the $[\bar{1}10]$ direction do not introduce as large of a stress on the surface. Specifically, for the same 0.1 eV drop in binding energy, the Cu atom can be displaced up to 0.8 Å in the $[\bar{1}10]$ direction. Once again, as the displacement of the Cu atom increases, the eventual result is the breaking of the Cu-O bonds. This also demonstrates the relative strength of the O-Ti bonds compared to the Cu-O bonds.

7.3 Cu Adsorption in the Presence of Bridging Oxygen Vacancies

As discussed above, adsorbed Cu atoms prefer to bind to the bridging O atoms, along the [001] bridging O row. Therefore, it is reasonable to wonder whether the removal of one or more of these bridging O atoms would significantly affect the binding and diffusive characteristics of adsorbed Cu atoms. Moreover, since real TiO_2 (110)

surfaces under experimental conditions have bridging O vacancies, as discussed in the previous chapter, it is important to investigate their impact on Cu adsorption. I investigated the adsorption of Cu on the isolated (25%) and interacting (50%) ordered bridging O vacancy structures discussed in Chapter 6. Both structures are described using the same 1×4 non-orthogonal unit cell. Once again, the Cu atoms and top two trilayers of the surface were allowed to fully relax.

For a single Cu adatom on the partially vacant surfaces, I mapped out the Cu-surface interaction only along the [001] bridging O rows. One reason for this is that previous results for the stoichiometric surface show that Cu is more likely to bind along these rows [14, 64]. Additionally, even when binding somewhere between [001] bridging O rows, the Cu adatom prefers to bond to the bridging O atoms on a [001] row. Since the surface defects in question are caused by the removal of these bridging O atoms, it seems likely that bonding between rows is much less favorable. Second, due to the large number of atoms in the necessarily large unit cells required to model a surface with defects, each DFT total-energy calculation is computationally expensive. Moreover, the creation of a bridging O vacancy destroys the symmetry of the unit cell, so many more points would be required to map a potential energy surface of comparable quality to those discussed previously. Therefore, generating the full potential energy surface would have been prohibitively costly and of limited scientific value.

Figure 7.5 shows the binding energy of the Cu adatom along the [001] bridging O rows for the 25% and 50% ordered vacancy configurations, as well as the stoichiometric surface. Data for the stoichiometric surface were obtained using a 2×3 orthogonal unit cell. Note that figure 7.5 plots the binding energy for this unit cell, whereas figure 7.4 shows the interaction potential energy (i.e., the negative of the binding energy). Symbols indicate the DFT total-energy calculations, and solid lines through the points are smooth spline fits to guide the eye. Additionally, a ball-and-stick model

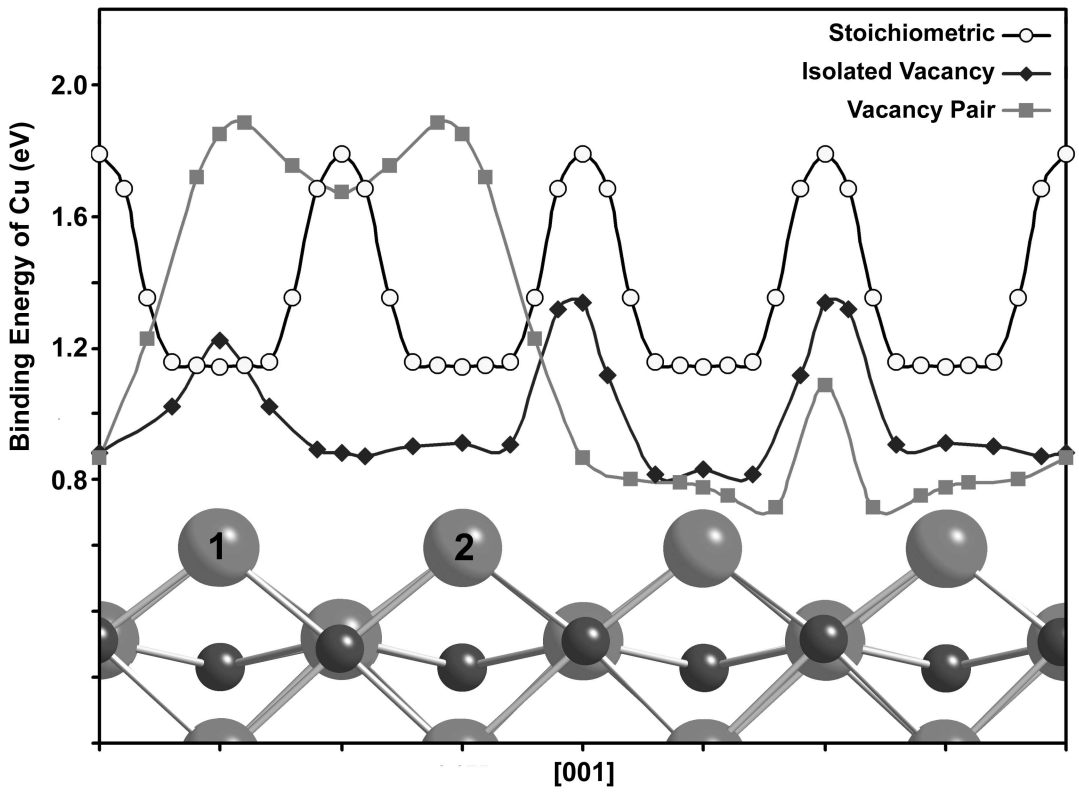

Figure 7.5: The binding energy is plotted in eV for Cu atoms adsorbed along the [001] bridging O row on stoichiometric and defective TiO_2 (110) surfaces. Plotted points represent DFT total energy calculations, where a smooth curve is drawn through the points for each case. A ball-and-stick model of the surface is superimposed below the curves, where the 25% ordered vacancy phase corresponds to removing the bridging O atom labeled 1, and the 50% ordered vacancy phase has the bridging O atoms labeled 1 and 2 both removed

of the surface is superimposed below the curves, where the 25% ordered vacancy phase corresponds to removing the bridging O atom labeled 1, and the 50% ordered vacancy phase has the bridging O atoms labeled 1 and 2 both removed.

As discussed previously, the preferred location of Cu atoms adsorbed on the stoichiometric surface is over the six-fold coordinated Ti atom such that the Cu atom can bind to the two adjacent bridging O atoms on the [001] row. In this arrangement, analysis of the electronic charge density reveals that the adsorbed Cu atom donates charge to the bridging O atoms in a similar manner to that which has been seen and discussed in previous studies on the binding of Au, Ag, and Cu to the bridging O atoms [10, 64]. This type of behavior is also observed for the isolated (25%) vacancy configuration. However, as shown in figure 7.5, the binding energy is significantly less for a Cu atom that is adsorbed near a bridging O vacancy than far from one. Note that anywhere on the 25% vacant 1×4 non-orthogonal unit cell is considered near a vacancy, so that the study of Cu adatoms far from a vacancy refer adsorption on the stoichiometric surface. When binding between two bridging O atoms that are near the isolated vacancy, the binding energy is 1.34 eV, which is 0.42 eV less than the binding energy for Cu adsorbed on the stoichiometric surface. This drop in binding energy can be understood by the change in the charge density caused by the creation of the nearby bridging O vacancy. Removing a bridging O atoms results in an increase in the charge density for both nearby Ti atoms on the [001] bridging O row, as well as the nearby Ti atoms located between the [001] bridging O rows. This transfer of charge to all the Ti atoms near the surface agrees with other theoretical calculations [10], and is further supported by my calculations, which show that the binding energy for Cu to the five-fold coordinated Ti atoms that are located between [001] bridging O rows is 0.88 eV and 0.91 eV on the 25% and 50% vacant surfaces respectively. This is a two-fold increase over the same Cu-surface bond on the stoichiometric surface, as listed for the 2×3 unit cell in table 7.1. The electron density transfer to the sur-

face effects the likelihood of the bridging O atoms adjacent to the vacancy to accept charge donated from the Cu atoms. This explains the observed decrease in the binding energy for Cu atoms adsorbed near these bridging O atoms.

As shown in figure 7.5, the binding energy for Cu on the stoichiometric surface is larger than for Cu on a surface with an isolated vacancy at all locations except one, the vacancy site. At this location, the two Cu-Ti bonds are 0.09 eV more favorable than the Cu-O bond that would occur on the stoichiometric surface. This can be understood by looking at the change in charge density caused by the adsorption of Cu. As discussed above, when the vacancy is formed, the surface Ti atoms gain electronic charge. When Cu is adsorbed in the vacant site, this excess charge on the Ti atoms redistributes such that it is shared between the Cu and Ti atoms. Previous studies have shown that this redistribution of charge, and the corresponding binding energy, depends on the electronegativity of the adsorbate [10]. Since the electronegativity of Cu is similar to that of Ti, the charge redistributes between the atoms, resulting in a pair of energetically weak bonds, with a length of 2.60 Å, to the Ti atoms on the bridging O row. These results are in agreement with previous investigations on Cu and Ag [64], as well as the larger charge transfer and corresponding higher binding energy for adsorption of the more electronegative Au atoms [10].

Figure 7.5 also shows that an isolated bridging O vacancy poses a barrier for Cu diffusion along the [001] bridging O row. Additional testing of Cu adsorption near the vacancy, but between the [001] bridging O rows reveals that the barrier over the planar O atoms remains essentially the same as for the stoichiometric surface, with only a 0.03 eV increase in binding energy. However, when compared to the stoichiometric surface, adsorption over the five-fold coordinated Ti atoms is found to be energetically more favorable by 0.45 eV, largely due to the increase in charge density on all surface Ti atoms near the vacancy, as discussed previously. While this significantly reduces the barrier between [001] bridging O rows, Cu diffusion along

any surface direction near a bridging O vacancy remains unlikely. These results are in qualitative agreement with other theoretical results for Cu and Ag [14]. However, differences are observed in the shape of the barrier along the [001] bridging O row. In particular, the previous studies found that the diffusion barrier along the [001] row to be relatively constant, i.e., they did not observe the potential energy minima (binding energy maxima) between bridging O atoms shown in figure 7.5. These differences can be explained by the vacancy-vacancy interactions that occur for the orthogonal 2×3 unit cell used in the previous theoretical investigations, but not in the 1×4 non-orthogonal unit cell. Specifically, for a 2×3 unit cell, all bridging O atoms along a [001] row containing a vacancy are adjacent to the vacancy or its periodic image. As discussed above, these bridging O atoms are less likely to bind to Cu. Therefore, the relatively constant diffusion barrier along the [001] row containing the vacancies, that was seen in previous studies [14], is due the close proximity of the bridging O vacancies. Using a 1×4 non-orthogonal unit cell eliminates both the vacancy-vacancy interactions and periodic effects of the vacancies on the Cu adatoms that are present for the 2×3 unit cell. Similar changes are expected for Ag adsorption on a 1×4 cell, since the potential energy surfaces and binding characteristics have been shown to be nearly identical to those of Cu [14, 64]. However, no significant changes are expected for adsorbed Au and Pt atoms, since both show a strong preference to bind in place of the bridging O vacancy [10, 12].

The effects of vacancy pairs on metal adatoms have not received nearly as much attention as the effects of isolated vacancies. The 50% concentration ordered vacancy phase discussed in Chapter 6 provides an ideal testing ground for studying metal-adatom/vacancy-pair interactions. As figure 7.5 shows, pairs of vacancies along the [001] bridging O row significantly alter the adsorption characteristics of Cu atoms compared to Cu on the stoichiometric surface and surfaces containing isolated vacancies. There still is a local peak in Cu binding energy between the remaining two

bridging O atoms. However, compared with the stoichiometric surface, the binding of Cu at this location on the 50% vacant surface is energetically much less likely by 0.67 eV. This occurs because, similar to the isolated vacancy case, bridging O atoms near a vacancy are less likely to accept charge from the Cu atom.

The Cu adatom binds most strongly to one of the vacancy sites on the 50% vacant surface. The bond energy of 1.88 eV is 0.12 eV higher than the peak Cu bond energy on the stoichiometric surface. In this case, the Cu bonds to the Ti atoms on the [001] bridging O row by pulling the excess charge on the Ti atoms (due to the vacancies) closer to itself. The formation of the vacancy pair results in a larger transfer of charge to the Ti atom between the vacancies, as compared to the charge transfer seen for a Ti atom near an isolated vacancy. This results in the ability for the Ti atom between the vacancies to share more charge with Cu than the other Ti atoms on the surface. As a result, the Cu adatom is bound tighter to this Ti atom between the vacancy pair, with a bond length of 2.53 Å, and has a weaker bond with one of the other Ti atoms on the [001] row, with a larger bond length of 2.74 Å. The stronger interaction with the Ti atom between the vacancies also explains the relatively small, 0.21 eV, energy barrier that is observed between vacant sites along the [001] row, figure 7.5. Additionally, similar to Cu adsorption near an isolated vacancy, a barrier reduction of approximately the same magnitude is observed between adjacent [001] bridging O rows near the pairs of vacancies.

In general, the likelihood of Cu diffusion on the TiO_2 (110) surface has been shown to be relatively small, except at high temperatures. The primary pathway for the diffusion of adsorbed Cu atoms is roughly along [001] bridging O rows. However, the presence of isolated bridging O vacancies increases the energy barrier along these rows near the vacancy. When the bridging O vacancies are no longer isolated, the effect on Cu diffusion is very different. In particular, the small 0.21 eV barrier shown for the oscillation of a Cu atom between a pair of vacant sites on the 50% surface suggests the

an easy diffusion pathway exists for Cu adsorbed along a chain of adjacent vacancies. Furthermore, the presence of bridging O vacancies (isolated or paired) reduces the energy barrier between adjacent [001] bridging O rows. Therefore, the significant differences between the stoichiometric and vacant surfaces for the adsorption and diffusion of Cu atoms suggests that bridging O vacancies will play an important role in the formation of Cu clusters and islands on the TiO_2 surface.

Chapter 8

Growth of Cu Clusters

8.1 Experimental Observations

Experimentally, Cu has been observed to form small three and six atom nanoclusters [50] as well as 3-D islands [47, 48, 51–55] on the TiO_2 (110) surface. The adsorbed Cu nanoclusters are observed to form in a precursor to a fcc structure, where the Cu-Cu bond lengths of 2.44(2) Å [50] are slightly smaller than the bulk fcc Cu-Cu bond length of 2.55 Å [56], and the Cu trimer plane is inclined at an angle of -30° with respect to the (110) surface [50]. As additional Cu atoms are adsorbed on the surface, the Cu nanoclusters grow to form 3-D islands where the Cu atoms in the island are also seen to adopt an fcc structure [47, 48, 54, 55, 68]. However, different orientations of the Cu island fcc structure relative to the TiO_2 (110) surface have been observed. Specifically, faceted islands with base width ranging from 260-780 Å and heights of 200 Å have been seen where the Cu (110) plane is parallel to the TiO_2 (110) surface [47], as illustrated in figure 8.1(a). On the other hand, Cu islands with the Cu (111) plane parallel to the TiO_2 surface, figure 8.1(b), are observed to have a more hemispherical arrangement with diameters ranging from 33-60 Å, and a heights of 5-12 Å [52].

The relative size difference of these Cu islands can be understood by looking at the lattice mismatch between the fcc structure of the Cu island and the rutile structure TiO_2 (110) surface. The lattice mismatch is determined by taking the difference between the lattice constants for the interfacing Cu and TiO_2 crystal planes, and then dividing by the appropriate TiO_2 lattice constant. In addition to the orientations, the

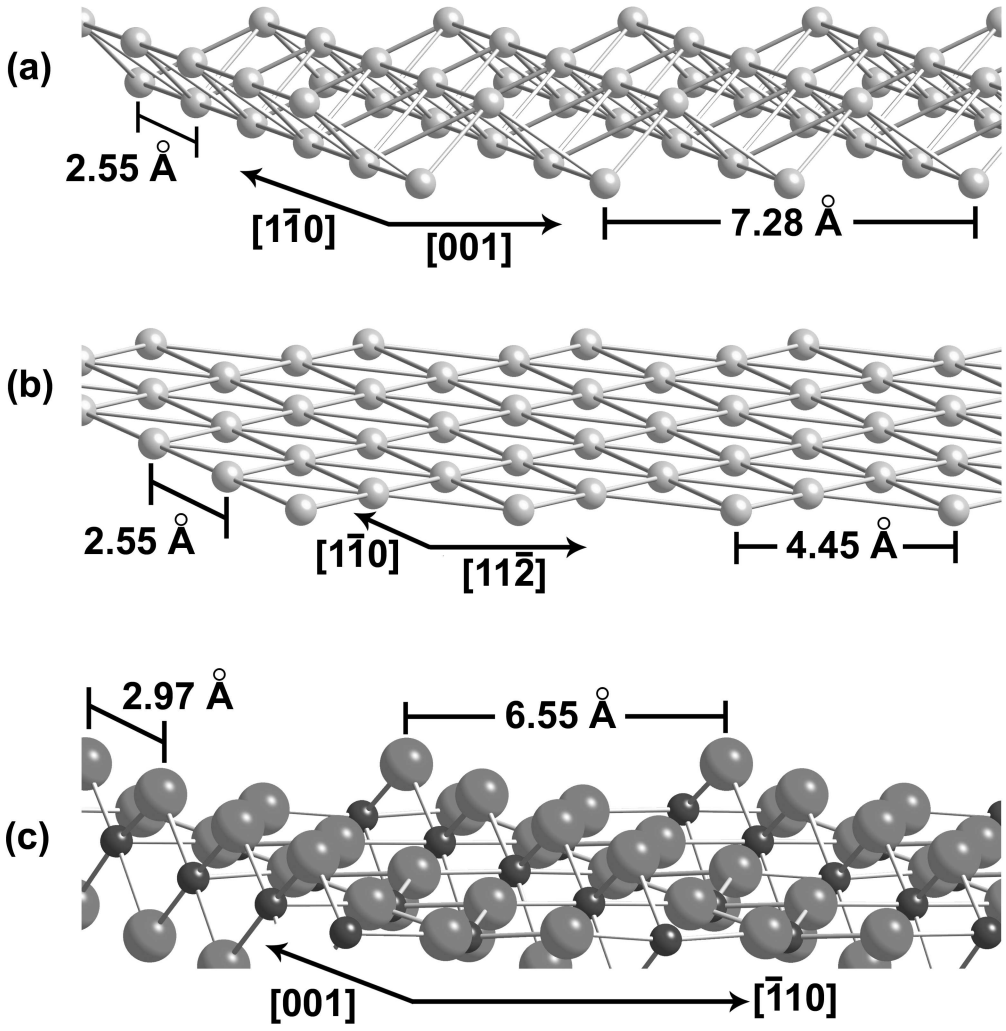

Figure 8.1: Experimental growth patterns for Cu islands on the TiO_2 (110) surface. As discussed in the text, large Cu islands have been observed such that the fcc Cu (110) plane (a) is parallel to the TiO_2 (110) surface (c), whereas small Cu islands are oriented such that the fcc Cu (111) plane (b) is parallel to the TiO_2 surface (c). The specific orientations and lattice constants ($\times\frac{1}{2}$ for the [001] direction in (a)) are labeled.

lattice constants are labeled in figure 8.1 for both Cu island arrangements (a and b) and the TiO_2 surface (c). The alignment of the Cu island's fcc structure to the [001] bridging O row is the same for both island orientations, where the calculated lattice mismatch is 13%. However, alignment of the two Cu island arrangements with the $[\bar{1}10]$ direction on the TiO_2 surface is significantly different. The larger islands have a smaller lattice mismatch of 11%, whereas the smaller islands have a much larger 32% lattice mismatch.

For both of these Cu island orientations, the lattice mismatch is relatively high, which gives rise to 3-D island growth for Cu instead of a more even wetting of the TiO_2 surface [47, 48, 51–55, 68]. Additionally, the experimentally observed reduction in the Cu-Cu bond length that occurs when Cu nanoclusters are adsorbed on TiO_2 [50] would lead to an even larger lattice mismatch along the [001] direction of the TiO_2 surface for both island orientations. While the relative magnitudes of lattice mismatches along the $[\bar{1}10]$ direction of the TiO_2 surface can partially explain the significant difference in observed Cu island sizes, it does not explain the why two different growth modes are observed for the Cu islands. Numerous experimental studies have observed growth of small Cu islands where the fcc Cu (111) plane is parallel to the surface, all of which support the specific island dimensions specified above [51–55]. Comparison of these studies with those that show the formation of Cu islands that are an order of magnitude larger reveal two main differences [47, 48]. The experiments showing larger island formation where done at a higher temperature of 473 K, as compared to the others, which were conducted at or below room temperature, 300 K. In Addition, the TiO_2 surface was highly non-stoichiometric (66% vacancy concentration) for larger Cu islands [47, 48], whereas the surface was nearly stoichiometric for the remaining experiments [51–55]. Based on the energy barriers for Cu diffusion that are discussed in the previous chapter, the small difference in temperature would not be expected to have much of an effect. On the other hand, the presence of bridging

O vacancies significantly impacts Cu diffusion [14]. As discussed in the following sections, the presence of vacancies also has a large impact on the relative orientation of two- and three-atom Cu nanoclusters (dimers and trimers), which form the basis for the eventual growth into Cu islands.

Theoretical modeling the experimentally observed clustering of Cu into small nanoclusters [50] and Cu islands [47, 48, 51–55, 68] requires the absorbtion of additional Cu atoms on the surface. To ensure that the resulting Cu dimers and trimers remain isolated from one another, a relatively large unit cell is needed. Similar to the study of a bridging O vacancy formation, the adsorption of the first Cu atom destroys the symmetries otherwise present on the bare, stoichiometric surface. Therefore, constructing potential energy surfaces for the absorbtion of additional Cu atoms would be highly computationally inefficient. Furthermore, a complete study involving the absorbtion of multiple Cu atoms would require the construction of potential energy surfaces for multiple locations of the first Cu adatom. Taking all of these factors into account, my investigations of Cu clustering are confined to a small number of scenarios that make use of information on the preferred binding sites [14, 64] and characteristics of Cu diffusion [14] on the stoichiometric and defective surfaces. The surface is modeled using a 1×4 non-orthogonal unit cell (denoted as β in figure 6.1) that is constructed by defining the origin to be at a six-fold coordinated Ti atom and including one primitive unit cell in the $[\bar{1}12]$ direction and four in the [001] direction. Investigations are conducted using surfaces that represent stoichiometric, isolated vacancy (a single vacancy per unit cell corresponding to a concentration of 25%), and interacting vacancy (a nearest-neighbor pair of vacancies per unit cell corresponding to a concentration of 50%) configurations. In each case, the substrate atoms and the adsorbed Cu atoms are allowed to relax to their minimum energy configurations.

Table 8.1: Average binding energies and bond lengths are listed for the adsorption of Cu dimers on the stoichiometric TiO_2 (110) surface. The orientation of the dimer is specified by the direction in which the Cu-Cu bond lies with respect to the surface, and the label refers to the specific dimer descriptions found in the text. Bond lengths are further specified with atom labels (when necessary) that can be found in the figure corresponding to the appropriate Cu dimer.

Cu Dimer Orientation	Label	Fig.	Avg. Binding Energy (eV)	Bond Lengths (Å)	
				Cu-Cu	Cu-O
[110]	1	-	1.66	2.24	1.87
[110]	2	-	1.65	2.28	2.01
[001]	3	8.2(a)	1.56	2.73	1.94 O(1) 2.00 O(2)
[001]	4	8.2(b)	1.70	2.32	1.90
$[\bar{1}10]$	5	8.2(c)	2.10	2.38	2.05

8.2 Clustering on the Stichometric Surface

Starting with the stoichiometric surface, I assumed that the first Cu adatom is located at a potential energy minimum. Investigation of the initial formation of Cu clusters (Cu dimers) is then carried out by considering the approach of a second Cu atom from three different directions. Specifically, I assumed the initially adsorbed Cu atom is located either above a single bridging O atom $(0,\frac{1}{2})$, or between a pair of bridging O atoms (0,0) along [001], where the locations (in lattice coordinates) given in parenthesis refer to the primitive unit cell shown in figure 7.1. I then consider scenarios that account for a second Cu adatom approaching from the [110] direction (above the first Cu atom), the [001] direction (diffusing along the same bridging O row that the first Cu atom is adsorbed on), and a combination of the [001] and $[\bar{1}10]$ directions (diffusing along a bridging O row that is adjacent to the one in which the first Cu atom is adsorbed).

Initial investigations focus on the formation of Cu dimers where the Cu-Cu bond is oriented in the [110] direction, i.e., the second Cu atom approaches from a location that is above the first. The resulting energetic and structural properties of the two Cu dimers that correspond to this arrangement are listed in table 8.1. In these two cases, the first Cu atom was either adsorbed above a bridging O atom (labeled 1) or between two bridging O atoms (labeled 2), and the second Cu was place on top of the first. The average Cu binding energies, which are calculated using equation 7.1 divided by the number of Cu atoms in the cluster, for both configurations are identical (within the precision of my total-energy calculations) at 1.66 eV and 1.65 eV respectively. Similarly, the Cu-Cu bond lengths are nearly identical at 2.24 Å and 2.28 Å respectively. In both cases, the adsorption of the second Cu atom results in an increase of the Cu to bridging O bond length for the Cu atom nearest the surface. When Cu is bound to a single bridging O, the bond length increased by 0.05 Å to a length of 1.87 Å, and when bound to a pair of bridging O atoms, the two identical Cu-O bonds increased by 0.13 Å to a length of 2.01 Å. The formation of two nearly identical Cu dimers, adsorbed at distinct locations on the surface, indicates a preference for Cu-Cu interactions over Cu-surface interactions. This is consistent with experimental observations of a relatively weak Cu-surface interaction [54, 68].

The next set of Cu dimers studied are formed by the adsorption and diffusion of a second Cu atom along the same [001] bridging O row upon which the initial Cu atom is adsorbed. In this scenario, a Cu dimer with the Cu-Cu bond oriented in the [001] direction of the TiO_2 surface is found to adsorb at two locations along the [001] bridging O row, where the details are listed in table 8.1. In both cases, a displacement of the adsorbed Cu atoms off of the bridging O row, in order to break the symmetry of the unit cell, results in restoring forces on the Cu atoms. This indicates that the minimum energy orientation of these Cu dimers is along the [001] bridging O row. The first location, listed as dimer 3 in table 8.1 and shown in figure 8.2(a),

consists of the Cu dimer centered above a single bridging O atom. In this case the average binding energy for Cu is 1.56 eV and the Cu-Cu bond length of 2.73 Å is large compared to the bulk value. The second configuration, listed as dimer 4 in table 8.1 and shown in figure 8.2(b), occurs when the Cu dimer is centered above a six-fold coordinated Ti atom linking two nearest-neighbor bridging O atoms. The average binding energy and Cu-Cu bond length for this arrangement are 1.70 eV and 2.32 Å respectively. The similar binding energies for these two dimers further support the preference of Cu-Cu interactions over Cu-surface interactions. While the Cu atoms forming dimer 3 have a larger number of Cu-O bonds than those in dimer 4, the Cu-Cu bond length is significantly smaller for dimer 4 since the additional Cu-O bonds in dimer 3 prevent the Cu atoms from coming as close to each other. This results in the larger calculated average binding energy for dimer 4, and shows that the Cu-Cu interaction is energetically more important than the Cu-surface interactions.

Of all the possible Cu dimer orientations discussed so far, the preferred arrangement occurs when the dimer is adsorbed above a six-fold coordinated Ti atom linking two nearest-neighbor bridging O atoms and the Cu-Cu bond is aligned with the [001] direction on the TiO_2 surface. The locations of the Cu atoms agree relatively well with those seen experimentally (for two of the three atoms in a Cu trimer) [50], and previous theoretical investigations on the adsorption of multiple Cu atoms [66]. However, in each of the four orientations for the Cu dimers mentioned above, the average binding energy per Cu atom is *less than* the binding energy for an isolated Cu atom between a nearest-neighbor pair of bridging O atoms (1.76 eV). Therefore, assuming that Cu atoms are able to diffuse into the lowest energy arrangement, dimer formation in any of the above mentioned orientations would not be expected. Rather, the Cu atoms would prefer to remain isolated. At this point, it is worthwhile to note that the experiment showing Cu trimer formation used chemical reactions to deposit Cu instead of vapor deposition (which is closer to the approach taken in my total

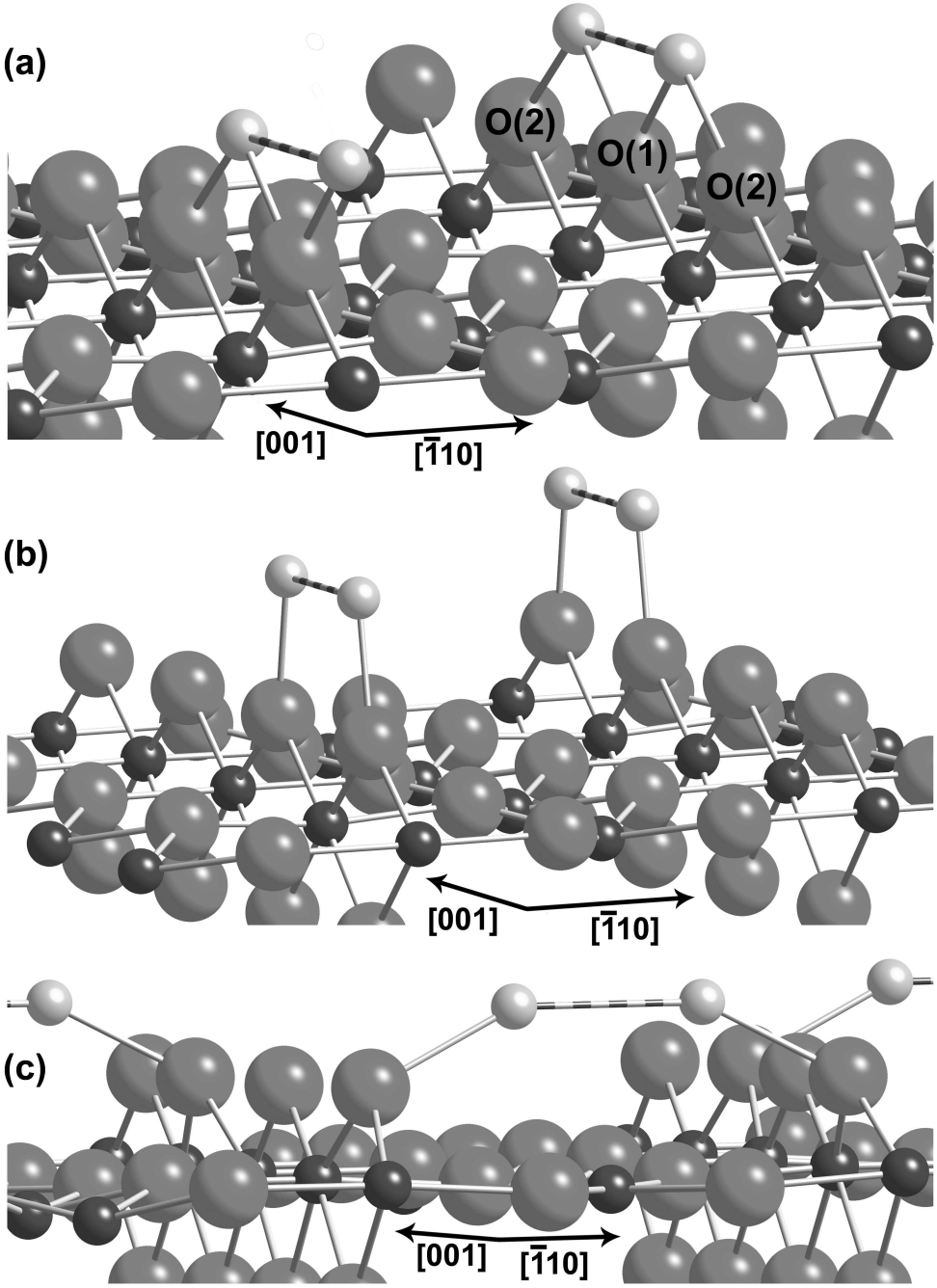

Figure 8.2: Cu dimer formation for adsorption on the stoichiometric TiO_2 (110) surface is shown using ball and stick models. The large-light, small-dark, and small-light spheres represent O, Ti, and Cu atoms respectively. Dimer arrangements 3 and 4 have the Cu-Cu bond oriented along the [001] direction and are shown in (a) and (b) respectively. Panel (c) illustrates dimer 5, which is oriented in the [$\bar{1}$10] direction. The numbers correspond to those in table 8.1 and the descriptions in the text.

energy calculations) and was carried out at 363 K (low temperature compared to the diffusion barriers for Cu adatoms, as discussed in the previous chapter) [50].

One additional approach mode still remains for the formation of Cu dimers, the diffusion of a second Cu atom along a bridging O row that is adjacent to the one in which the first Cu atom is adsorbed. An initial glance at this type of arrangement suggests that Cu dimer formation would not be likely due to the large potential energy barrier for Cu diffusion between the [001] bridging O rows [14]. However, the second Cu atom would not necessarily need to cross the large diffusion barrier located over the five-fold coordinated Ti atoms. As seen in figure 8.2(c), the Cu-Cu bond can be aligned with the $[\bar{1}10]$ direction such that each Cu is bound to a bridging O atom and the Cu-Cu bond extends over the five-fold coordinated Ti atom. In this arrangement, labeled as 5 in table 8.1, the respective Cu-Cu and Cu-O bond lengths of 2.38 Å and 2.05 Å are comparable to those found in dimer 4, where both Cu atoms lie along a single bridging O row. However, this arrangement yields an average Cu binding energy of 2.10 eV, which is significantly stronger than the value found for any of the previous Cu dimer arrangements. Additionally, this dimer is 0.68 eV more energetically favorable than the adsorption of two isolated Cu atoms.

The energetic preference of the Cu dimer shown in figure 8.2(c) can be understood by looking at the preferred binding locations of Cu atoms and the stresses imposed on the TiO_2 surface due to Cu adsorption. In this case, each Cu binds to a bridging O atom, which has been shown to be preferred for Cu on TiO_2 [14, 64]. Furthermore, for this dimer each Cu atom exerts a force on the bridging O atom to which it is bound in the $[\bar{1}10]$ direction, thus pulling it away from the [001] row. This results in a much smaller stress on the surface than occurs for forces acting on the bridging O atoms in the [001] direction, as seen by comparing the relative slopes of the potential energy minima in figures 7.2-7.4.

At this point, two important conclusions can be made regarding the formation of Cu dimers on the TiO_2 (110) surface. First, clustering of Cu atoms has been shown to be significantly preferred to isolated adatoms. Second, as shown in figure 8.2(c), the initial growth of Cu clusters on the stoichiometric surface occurs parallel to the (110) surface in the $[\bar{1}10]$ direction. This initial growth mode supports the experimentally observed arrangement of small Cu islands, where the flat (111) fcc Cu face is observed to be parallel to the TiO_2 (110) surface [54, 55].

My investigations into the formation of Cu trimers on the stoichiometric TiO_2 (110) surface build upon the most energetically favorable Cu dimer arrangements. In particular, a third Cu atom was added to the Cu dimers 4 and 5, shown in figure 8.2(b) and 8.2(c) respectively. I only studied Cu trimer formation where the three Cu atoms formed the corners of a triangle, which is similar to the configurations observed for Cu trimers experimentally [50] and those found in the fcc crystal structure of bulk Cu [56]. This is done because Cu-Cu interactions can significantly increase the average Cu binding energy of the nanocluster to the surface. Since this Cu trimer formation results in the highest possible number of Cu-Cu bonds and has been observed experimentally, it is reasonable to assume that it is the most likely configuration for a cluster of three adsorbed Cu atoms. Another reason for limiting my investigations to Cu triangles is to avoid unintended Cu-Cu interactions resulting from the use of periodic unit cells in my total energy calculations. Since these unintended Cu-Cu interactions are more likely to occur with each additional Cu adatom, and the relatively large 1×4 non-orthogonal unit cell is already computationally expensive, I further limited my investigations to Cu clusters of no more than three adatoms.

Initially, I added the third Cu atom above dimers 4 and 5 such that the Cu trimer plane is perpendicular to the TiO_2 (110) surface. The resulting relaxed configurations are shown in figure 8.3 for Cu atoms binding to a pair of nearest-neighbor bridging O atoms (a) and two bridging O atoms on adjacent [001] bridging O rows (b). The

Table 8.2: Average Cu binding energies and bond lengths are listed for the adsorption of Cu trimers on the stoichiometric TiO_2 (110) surface. The orientation of the trimer is specified by the relative angle between the trimer plane and the (110) surface. The label refers to the specific trimer descriptions found in the text, and the bond lengths are further specified with atom labels that can be found in the figure corresponding to the appropriate Cu trimer.

Cu Trimer Orientation	Label	Fig.	Avg. Binding Energy (eV)	Bond Lengths (Å)	
				Cu-Cu	Cu-O
90°	1	8.3(a)	2.22	2.33 Cu(1-1*) 2.33 Cu(1,1*-2)	1.87
90°	2	8.3(b)	2.21	2.68 Cu(1-1*) 2.31 Cu(1,1*-2)	1.97

Cu trimer in the ($\bar{1}$10) plane located on a bridging O row, labeled 1 in table 8.2 and shown in figure 8.3(a), has an average Cu binding energy of 2.22 eV. This value is 0.46 eV higher than observed for isolated Cu atoms and 0.12 eV higher than the most energetically favorable Cu dimer configuration. In this case, the Cu-Cu distances are each 2.33 Å, and the two Cu-O bonds are 1.87 Å. Figure 8.3(b) shows the second Cu trimer configuration that was investigated, where the Cu trimer lies in the (001) plane that contains the bridging O atoms to which it is bound. For this configuration, denoted 2 in table 8.2, the average binding energy is comparable to the value obtained for trimer 1 at 2.21 eV, and the two 1.97 Å Cu-O bonds are larger than those in trimer 1. However, here the Cu-Cu bond lengths are observed to differ, where the Cu-Cu distance for the two atoms adsorbed on the surface (labeled 1 and 1* in figure 8.3(b)) increases to 2.68 Å, and the remaining Cu-Cu bonds are each 2.31 Å.

Having found that growth from a Cu dimer to a trimer, in the [110] direction, is energetically favorable, I proceeded to investigate Cu trimer formation where the trimer plane aligns at different inclinations with respect to the TiO_2 surface plane.

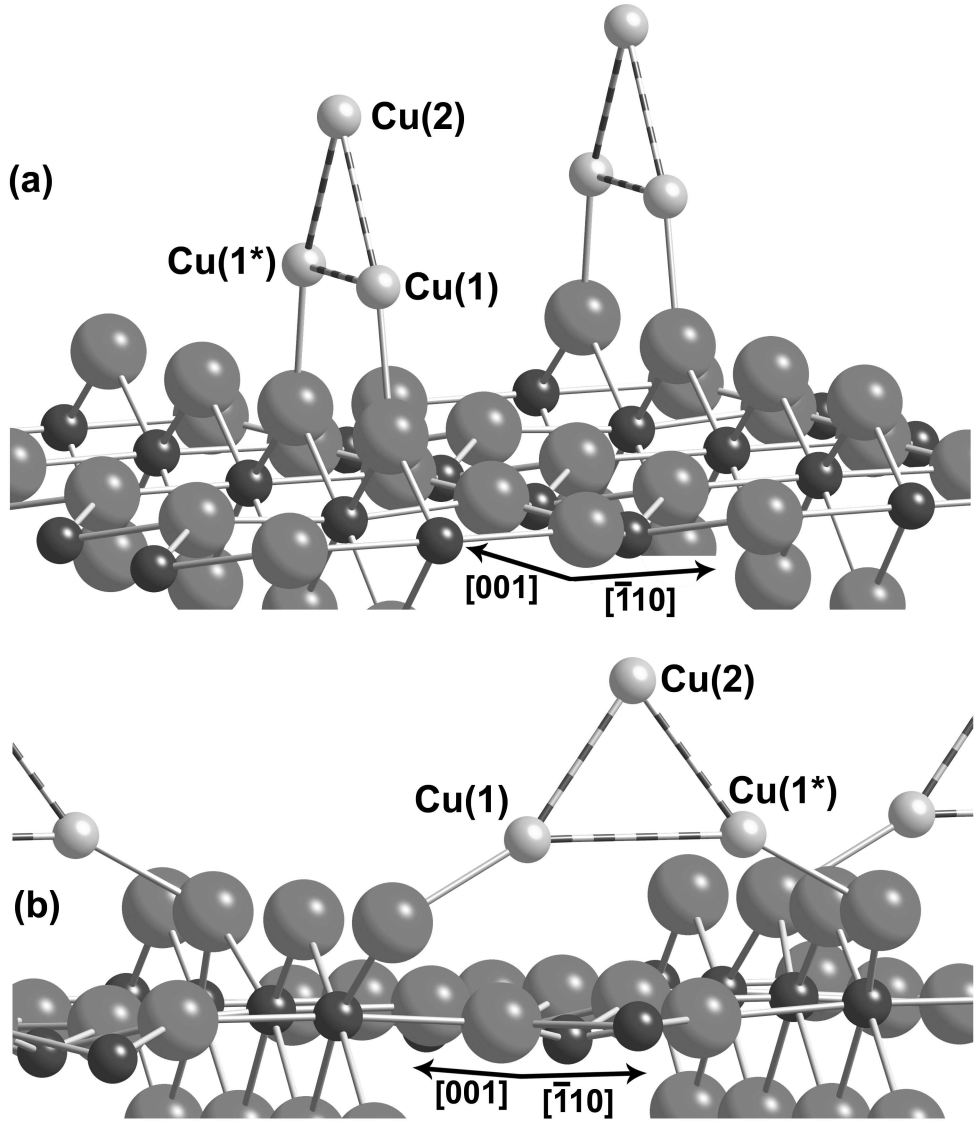

Figure 8.3: Cu trimer formation for adsorption on the stoichiometric TiO_2 (110) surface is shown using ball and stick models. The large-light, small-dark, and small-light spheres represent O, Ti, and Cu atoms respectively. Arrangements are observed for Cu trimer 1 and 2, which are shown in parts (a) and (b) respectively. The numbers correspond to those in table 8.2 and the descriptions in the text.

To do this, I reoriented the Cu trimer in both configurations shown in figure 8.3 such that the trimer plane was approximately parallel to the TiO_2 (110) surface. In both cases, the location for the third Cu atom is initially near one or more planar O atoms, and the Cu trimer configuration more closely resembles the experimental observations [50]. However, relaxation of both systems resulted in the Cu trimer reorienting itself to a configuration where the trimer plane is (nearly) perpendicular to the TiO_2 surface, as shown in figure 8.3.

Two important conclusions can be drawn from my investigations of Cu trimers on the stoichiometric TiO_2 surface. First, the average binding energy for the adsorbed Cu atoms in the trimer configurations is higher than either isolated Cu atoms or Cu dimers. This demonstrates the continued preference for Cu adatoms to cluster together. Additionally, while the energetics of the initial Cu dimers used to form the trimers are significantly different, the resulting trimer energies are identical, within the precision of the total-energy calculations. This further supports the experimental observations of strong interactions between the adsorbed Cu atoms and between the Ti and O atoms of the surface, and a much weaker Cu-surface interaction [54, 68]. Second, after initial cluster growth in the $[\bar{1}10]$ direction, Cu clustering proceeds perpendicular to the TiO_2 surface, in the [110] direction. This can be understood by noting that the orientation of the Cu trimer parallel to the TiO_2 surface does not allow for the third Cu atom to bind to a bridging O atom, which is the most energetically favorable type of Cu-surface interaction when bridging O vacancies are not present [14, 64]. Preferred cluster growth perpendicular to the surface is further supported by the relatively large lattice mismatch between fcc Cu and the TiO_2 (110) surface, regardless of the growth orientation in the surface direction, as discussed in the beginning of this chapter.

The above discussion focuses on the aspects of my results that are in good agreement with experimental and theoretical work. However, not all of my results show

such good agreement. I found Cu trimers to orient perpendicular to the surface, whereas experimental results showed the formation of a Cu trimer oriented such that the plane of the Cu trimer was inclined at an angle of -30° with respect to the (110) surface. In this experiment, two Cu atoms bonded to bridging O atoms along the [001] row, in agreement with the results discussed above, but the third Cu was much closer to the surface near the planar O atoms. While this arrangement has been observed experimentally for Cu nanoclusters [50], it is not observed experimentally in Cu island formation on the stoichiometric surface where Cu trimers are observed to form both parallel to and perpendicular to the TiO_2 surface [47, 48, 51–55, 68]. Therefore, my results showing perpendicular trimer growth continue to support the experimentally observed Cu growth on the stoichiometric surface where the fcc Cu (111) plane is parallel to the TiO_2 (110) surface. Additionally, even though the calculated Cu-Cu and Cu-O bond lengths listed in table 8.2 are in relatively good agreement with the experimentally reported values (2.44(2) Å and 2.33(5) Å respectively [50]), the calculated and experimental Cu trimer orientations do not agree. There are many possible reasons for this disagreement, one of which is related to the effects of a bridging O vacancy. Since the following section addresses Cu clustering on the non-stoichiometric surface, this discussion on this experimentally observed formation of Cu nanoclusters will resume below.

8.3 Effects of Bridging O Vacancies on Cu Clustering

An approach similar to the one described above for Cu clustering on the stoichiometric surface was used to study Cu clustering near isolated (25%) and interacting (50%) bridging O vacancies. In this case, the initial adsorbed Cu atom is assumed to be located in the vacant site when studying the isolated 25% vacancy arrangement, and either in one or between the two vacant sites (over the center Ti atom) for the 50% interacting vacancy arrangement. Initial investigations focused on the formation of

Cu dimers by once again considering the approach of a second Cu atom from the [110] direction (above the first Cu atom), the [001] direction (diffusing along the same bridging O row that the first Cu atoms is adsorbed on), and a combination of the [001] and [$\bar{1}$10] directions (diffusing along a bridging O row that is adjacent to the one in which the first Cu atoms is adsorbed).

As discussed in the previous chapter, the formation of one or more bridging O vacancies reduces the energy barrier between adjacent [001] bridging O rows, making Cu diffusion in the [$\bar{1}$10] direction more likely. This would increase the chances of forming a Cu dimer oriented in the [$\bar{1}$10] direction, which as discussed above, has the highest average binding energy for Cu dimers on the stoichiometric surface. However, this high average binding energy is due to the combination of the single Cu-Cu bond with two Cu-O bonds, where each Cu atom binds to a bridging O atom on adjacent [001] rows. Since the formation of one or more bridging O vacancies would result in the loss of one of the Cu-O bonds, this Cu dimer arrangement would appear to be much less likely to occur near a bridging O vacancy. Calculations involving this Cu dimer orientation for both the 25% and 50% vacant surfaces confirmed this. In each case, relaxation of the system results in the Cu dimer moving away from the vacancy(ies) and towards the remaining bridging O atom on the [001] row that is adjacent to the vacancy(ies), i.e., in the [$\bar{1}$10] direction. Since the Cu atoms were observed to move away from the vacancy(ies), and the surface unit cell used is defined such that any location in the unit cell is considered to be near a vacancy, further investigation of these Cu dimer orientations was not pursued.

While the formation of Cu dimers oriented in the [$\bar{1}$10] direction is not observed to occur near bridging O vacancies, Cu clustering is found to occur on the reduced surface. In particular, three dimers were formed such that the Cu-Cu bond is aligned with the [110] direction. Two dimers were formed by the initial adsorption of a Cu atom in a vacant site, with the second atom above the first, on the 25% (labeled 6) and

Table 8.3: Average Cu binding energies and bond lengths are listed for the adsorption of Cu dimers on the non-stoichiometric TiO_2 (110) surface. The orientation of the dimer is specified by the direction in which the Cu-Cu bond lies with respect to the surface, and the label refers to the specific dimer descriptions (including the vacancy concentration of the TiO_2 surface) found in the text. Bond lengths are further specified with labels corresponding to the coordination (4-fold and 5-fold) of the Ti atoms in the bridging O row near one or more vacancies.

Cu Dimer Orientation	Label	Fig.	Avg. Binding Energy (eV)	Bond Lengths (Å)		
				Cu-Cu	Cu-O	Cu-Ti
[110]	6	-	1.23	2.26	-	2.88 Ti(5)
[110]	7	-	1.56	2.28	-	2.57 Ti(4) 2.76 Ti(5)
[110]	8	-	1.51	2.27	-	2.53 Ti(4)
[001]	9	8.4(a)	2.10	2.30	2.01	2.55 Ti(5)
[001]	10	8.4(b)	1.99	2.29	-	2.56 Ti(4) 2.76 Ti(5)
[001]	11	8.4(c)	1.96	2.42	1.93	2.64 Ti(4)

50% (labeled 7) reduced surfaces. A second dimer was constructed on the 50% vacant surface (labeled 8) where the first Cu atom is adsorbed above the Ti atom between the vacancies, and the second Cu adatom is once again located on top of the first. The characteristics of these dimers, listed in table 8.3, are similar to those found for dimers that form in the same orientation on the stoichiometric surface (dimers 1 and 2 in table 8.1). Specifically, the Cu-Cu bond lengths are found to be identical, within the precision of my calculations. Analysis of the average binding energies for all of these dimers show that the adsorption of isolated Cu atoms on either the stoichiometric (1.76 eV) or 50% vacant (1.88 eV) surfaces is preferable over Cu dimer formation in this orientation. While the average binding energies for [110]-oriented dimers do differ, this is primarily due to the different types of bonding occurring between the adsorbed Cu atoms and the TiO_2 surface. The higher binding energies for dimers 1 and 2 arise from the presence of strong Cu-O bonds, whereas the lower energies for dimers 6-8 result from a shift to Cu-Ti bonds due to the bridging O vacancies. Furthermore, as shown in the previous chapter, decreasing the coordination number of the Ti atoms in the [001] bridging O row (increasing the vacancy concentration) results in a corresponding increase in Cu-Ti binding energy. This is reflected in the higher binding energies listed in table 8.3 for dimers 7 and 8 which are adsorbed on the 50% vacant surface.

The remaining approach direction to be investigated assumes that the second Cu atom diffuses along the same [001] bridging O row as the first adsorbed Cu atom, and, in this case, the bridging O vacancy(ies). Admittedly, the diffusion of Cu along the [001] row approaching one or more vacancies is less likely to occur than similar diffusion on the stoichiometric surface [14]. As discussed in the previous chapter, this is due to the smaller affinity for the adsorbed Cu atom to bind to the bridging O atoms adjacent to the vacant sites. However, once that potential energy barrier is overcome, continued motion in the [001] direction across one or more vacant sites is

much more likely to occur, as shown in (the inverse of) figure 7.5. This approach leads to the formation of three additional Cu dimers on the reduced surfaces (labeled 9-11 in table 8.3) that are described below and illustrated in figure 8.4.

As shown in figure 8.4(a), the formation of a single Cu dimer in this [001] orientation is observed to occur near an isolated bridging O vacancy. The corresponding energetic and structural characteristics are listed in table 8.3 (dimer 9), where the average binding energy of the adsorbed Cu atoms and the Cu-Cu bond length is seen to be is 2.10 eV and 2.30 Å respectively. These are nearly identical to the characteristics of the most favorable Cu dimer on the stoichiometric surface (dimer 5), which is oriented between [001] rows such that each Cu atom binds to its own bridging O atom. In this case, the vacancy allows the Cu dimer along the [001] row to adsorb in a similar manner, where each Cu atom binds to a bridging O atom with a comparable bond length of 2.01 Å. Even though Cu-O bonding is less likely for bridging O atoms adjacent to a vacancy, this dimer has a much higher average binding energy ($0.40 - 0.54$ eV) than the dimers adsorbed on the stoichiometric surface with the same orientation (dimer 3 and 4). This can be explained by the additional interaction of the Cu dimer with the Ti atoms on the [001] row. The bridging O vacancy allows for the Cu dimer to bind much closer to the TiO_2 surface, as seen by comparison of figures 8.4(a) and 8.2(b). Also, the formation of the vacancy transfers charge to the surface Ti atoms, making Cu-Ti bonding more likely [10]. As a result, each Cu atom in this orientation on the reduced surface also has a 2.55 Å bond to the Ti atoms on the [001] bridging O row. Therefore, the energetic preference for Cu dimer formation along the [001] row at a bridging O vacancy is due to the combination of Cu-Cu, Cu-O, and Cu-Ti bonding.

A similar result is seen for Cu dimer formation on the 50% interacting vacancy arrangement, as described in table 8.3 for dimers 10 and 11. On this surface, Cu dimers were found to form either with each Cu atom in a vacant site (dimer 10), or over two

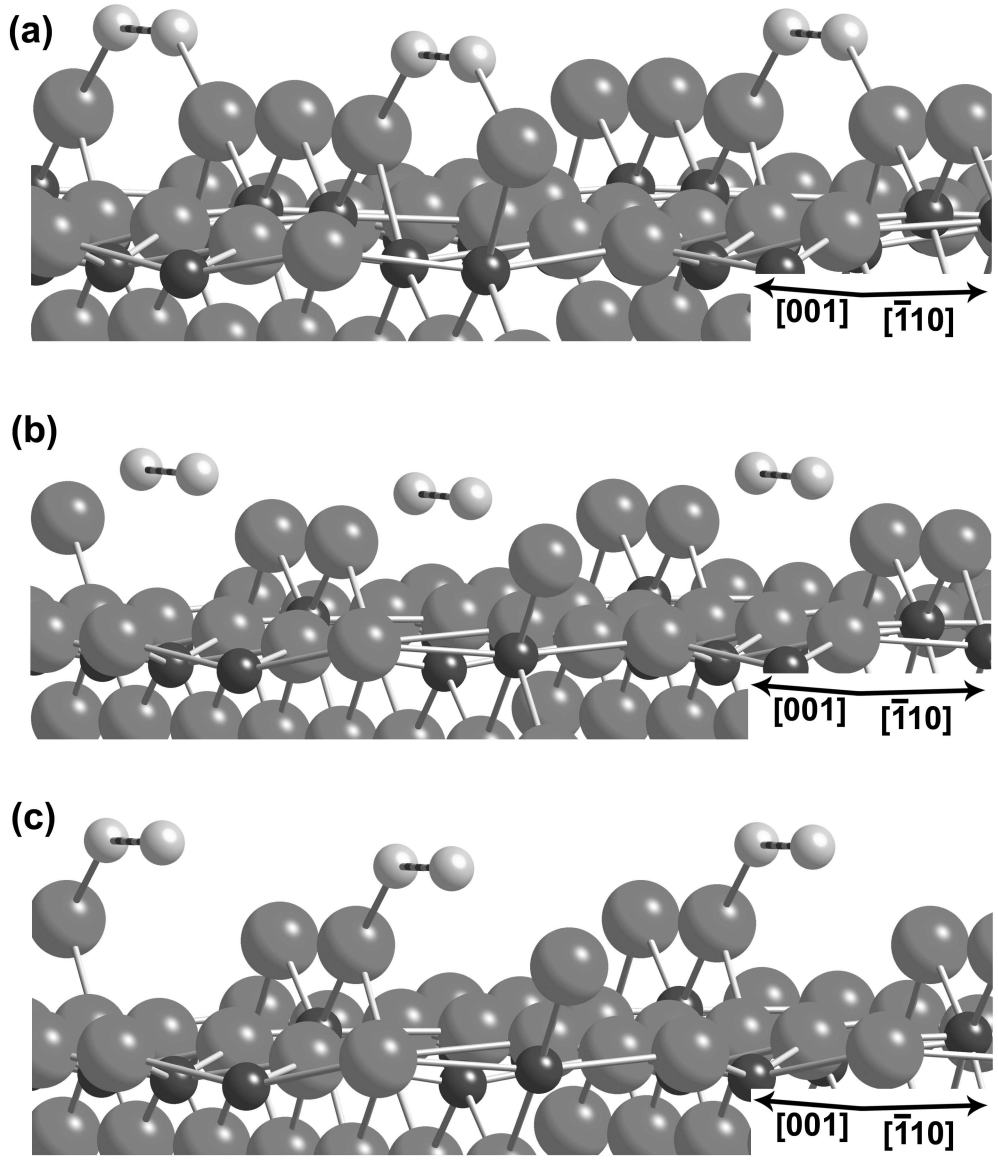

Figure 8.4: Cu dimer formation for adsorption in the [001] orientation on the reduced TiO_2 (110) surface is shown using ball and stick models. The large-light, small-dark, and small-light spheres represent O, Ti, and Cu atoms respectively. Part (a) illustrates dimer 9, which corresponds to adsorption near an isolated bridging O vacancy. Whereas dimers 10 and 11, shown in parts (b) and (c) respectively, correspond to adsorption on the 50% vacant surface.

of the Ti atoms uncovered by the vacancies and bound to a bridging O atom adjacent to one of the vacancies (dimer 11), as shown in figures 8.4(b) and 8.4(c) respectively. As seen in table 8.3, the average binding energies for each of these arrangements are computationally equivalent. Additionally, the Cu-Cu bond lengths are comparable to each other and the Cu dimers discussed previously. Similar to the adsorption of a single Cu atom on this 50% vacant surface, the most significant binding occurs with the Ti atom located between the vacancies. For the dimer formed in the vacant sites (dimer 10), each Cu is found to be 2.56 Å away from this Ti atom. However, for Cu dimer 11, only a single Cu atom is bound to this Ti atom with a slightly larger 2.64 Å bond length. In this case, additional binding occurs between the other Cu atom and the nearby bridging O atom that is adjacent to the vacancy. The resulting Cu-O bond of 1.93 Å is comparable to the corresponding Cu-O bond length in dimers 1-5 and 9. Therefore, the combination of Cu-O and Cu-Ti interactions once again result in a pair of energetically equivalent dimer arrangements.

As shown in table 8.3, Cu dimer formation on surfaces containing isolated (25%) or interacting (50%) vacancies is energetically favorable over the isolated adsorption of Cu atoms on either the stoichiometric (1.76 eV) or reduced (1.88 eV) TiO_2 surface. This supports the experimentally observed clustering of Cu atoms on reduced surfaces [47]. The energy preference for Cu clustering on the reduced surface is comparable to clustering on the stoichiometric surface. However, the orientation of the Cu dimer for initial cluster growth in the most energetically favorable configuration on the reduced surface (in the [001] direction) differs from that found for the stoichiometric surface (in the $[\bar{1}10]$ direction). While this suggests that Cu clusters would grow differently on significantly reduced surfaces, as compared to the stoichiometric surface, it does not support one experimentally observed growth pattern for fcc Cu on TiO_2 (110) over the other. This is because both orientations, found experimentally and shown in figure 8.1, consist of alignment between the $[1\bar{1}0]$ direction of fcc Cu and the [001]

Table 8.4: Average Cu binding energies and bond lengths are listed for the adsorption of Cu trimers near an isolated bridging O vacancy on the TiO_2 (110) surface. The orientation of the trimer is specified by the relative angle between the plane containing the three Cu atoms and the (110) surface. The label refers to the specific trimer descriptions found in the text. The bond lengths are further specified with atom labels that can be found in the figure corresponding to the appropriate Cu trimer, where bonds between two atoms labeled with an * are identical to the similarly numbered bonds by symmetry.

Orien.	Lbl.	Fig.	BE (eV)	Bond Lengths (Å)		
				Cu-Cu	Cu-O	Cu-Ti
90°	3	8.5(a)	2.12	2.58 Cu(1-1*) 2.32 Cu(1-2)	1.91 Cu(1)-O(1)	2.75 Cu(1)-Ti(1)
−22°	4	8.5(b)	2.12	2.45 Cu(1-1*) 2.32 Cu(1-2)	2.01 Cu(1)-O(1) 2.12 Cu(2)-O(2)	2.70 Cu(1)-Ti(1) 2.74 Cu(2)-Ti(2)

direction of the TiO_2 surface, which corresponds to the formation of Cu-Cu bonds along the [001] bridging O rows [47, 55].

In order to determine if the reduced TiO_2 surface supports a different growth mode than observed on the stoichiometric surface, a third Cu atom was adsorbed for the Cu dimer on the 25% reduced surface, shown in figure 8.4(a). In this case, a third Cu atom was initially adsorbed above the center of the dimer (as done for the stoichiometric surface) resulting in the Cu trimer oriented perpendicular to the (110) surface as shown in figure 8.5(a). As listed in table 8.4 under trimer 3, this configuration results in an average binding energy for the Cu atoms of 2.12 eV, which supports continued Cu clustering. Furthermore, as compared to the initial Cu dimer, expansion of the Cu-Ti bonds to 2.75 Å and reduction of the Cu-O bonds to 1.91 Å is similar to the formation of trimer 2 on the stoichiometric surface. Additionally, the Cu-Cu bond length for the Cu atoms composing the initial Cu dimer (labeled 1 and

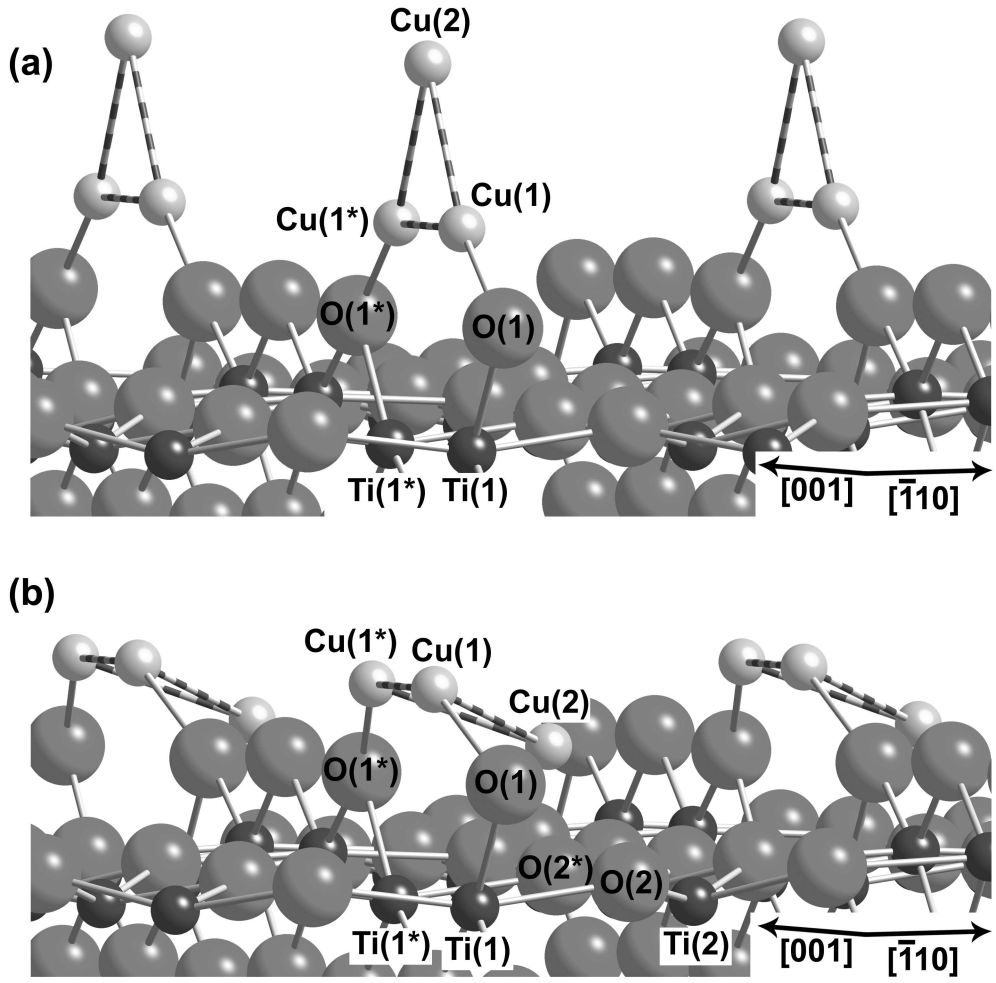

Figure 8.5: Cu trimer formation near an isolated vacancy on the TiO_2 (110) surface is shown using ball and stick models. The large-light, small-dark, and small-light spheres represent O, Ti, and Cu atoms respectively. Arrangements are observed for Cu trimer 3 and 4, which are shown in parts (a) and (b) respectively. The trimer numbers and atom labels correspond to those in table 8.4 and the descriptions in the text.

1* in figure 8.5(a)) expands slightly to 2.58 Å, and the remaining Cu-Cu bonds have a length of 2.32 Å, which was also observed to occur in the formation of trimer 2.

While the clustering characteristics of Cu atoms are further supported by this trimer formation, specifying a preferential growth mode is still not possible. Therefore, as done with Cu trimers on the stoichiometric surface, investigations were done where the trimer was initially place parallel to the surface. In this case, as shown in figure 8.5(b) and described in table 8.4 under trimer 4, the system relaxed to a new configuration. Specifically, the Cu trimer is oriented at an angle of -22° with respect to the TiO_2 (110) plane where the third Cu atom (labeled 2 in figure 8.5(b)) is closer to the surface than the other two Cu atoms of the trimer. The average binding energy of this arrangement is 2.12 eV, identical to the Cu trimer oriented perpendicular to the surface. For this orientation, the Cu-Cu bond length for the Cu atoms composing the initial Cu dimer expanded by a slightly smaller amount to 2.45 Å, while the remaining Cu-Cu bonds have the same 2.32 Å length. However, in this configuration each adsorbed Cu atom interacts with both O and Ti atoms on the surface, as detailed in table 8.4. In particular, the Cu atoms near the [001] bridging O row bond with the bridging O atoms adjacent to the vacancy and the Ti atoms on the [001] row. The Cu atom closer to the surface interacts with the planar O atoms and the Ti atom located between the [001] bridging O rows.

As discussed in detail for Cu trimer formation in the previous section, experiments have observed this type of Cu trimer growth on a surface that is assumed to be stoichiometric [50]. One possible explanation for the disagreement between the experimental trimer formation and theoretical investigations of Cu trimer on the stoichiometric surface is that the experimentally observed trimer formed at an isolated bridging O vacancy. This is suggested for three main reasons. First isolated bridging O vacancies are commonly present on the TiO_2 surface. Since the experiments were conducted in a vacuum at a temperature of 363 K [50], it is possible that some

isolated vacancies would form even if they were not initially present. The results presented above for Cu dimer and trimer formation show that clustering of Cu is energetically likely to occur near and far from an isolated vacancy, so observing Cu nanoclusters at a vacant site would not be unlikely. Second, the model used to fit the experimental data focused primarily on the orientation of the Cu trimer with the surface, not the local characteristics of the TiO_2 surface. Specifically, the Cu trimer was modeled using an unrelaxed TiO_2 surface [50]. Third, as shown in the previous chapter, Cu atoms are not likely to adsorb near a Ti atom located between bridging O rows unless a nearby bridging O vacancy is present. Therefore, the formation of a Cu trimer inclined towards the surface, as seen in figure 8.5(b), is much more likely to occur on the reduced TiO_2 surface. Assuming the experimental Cu trimer growth occurred near an isolated bridging O vacancy results in a good agreement between the experimental and theoretical trimers, where the -22° inclination of the Cu trimer is relatively close to experiment, which models a -30° inclination and comparable Cu-Cu bonds [50].

Additionally, this rearrangement of the Cu trimer into an energetically equivalent arrangement inclined at an angle of -22° to the TiO_2 surface suggests a relationship between Cu cluster growth and the number of vacancies on the surface. This orientation corresponds to Cu growth on the surface such that the [001] direction of fcc Cu is aligned with the $[\bar{1}10]$ direction on the TiO_2 surface, as shown in figure 8.1(a). Continued growth in this manner would result in the fcc Cu (110) plane forming parallel to the TiO_2 (110) surface, which agrees with the experimental Cu island growth done on highly reduced surfaces [47]. As discussed previously, the smaller lattice mismatch for this Cu-surface orientation would support the observed growth of larger Cu islands [47]. Therefore, my investigations on Cu clustering on the stoichiometric and reduced surfaces suggest that the different growth patterns for the experimentally observed Cu islands is largely due to the presence of bridging O vacancies on the TiO_2 surface.

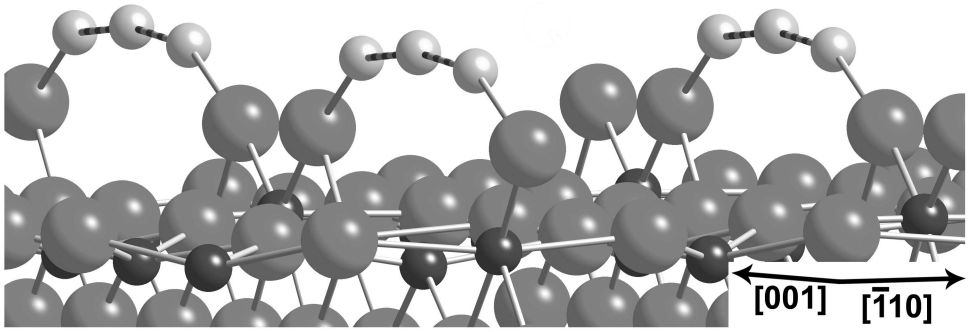

Figure 8.6: Cu trimer formation near interacting vacancies on the TiO_2 (110) surface is shown using ball and stick models. The large-light, small-dark, and small-light spheres represent O, Ti, and Cu atoms respectively. As described in the text, the Cu atoms form a 1-D chain aligned with the vacancies in the [001] bridging O row.

This can be explained by the increased preference for Cu-Ti binding that occurs when a vacancy is formed. However, the experiments showing this more favorable growth, and therefore larger Cu islands, did not contain isolated vacancies, but rather were highly reduced (66% vacancy concentration) [47].

To take this into account, the adsorption of a third Cu atom on the interacting 50% vacant surface was investigated. Initially, the third Cu atom was place above each of the two dimers shown in figure 8.4(b,c), as done for the previous trimer formation. Further studies were then conducted for a reorientation of the Cu trimer plane such that it was initially parallel to the TiO_2 surface. In all of these scenarios, relaxation resulted in the formation of a Cu chain aligned with the [001] direction and positioned above the vacant sites, as shown in figure 8.6, where the average binding energy per Cu atom is 2.18 eV. For each relaxed arrangement, the Cu bond lengths (2.33-2.35 Å), the length of the center Cu atom bond to the four-fold coordinated

Ti atom (2.48-2.51 Å), and the bond angle between the Cu-Cu bonds (185-187°), remained relatively constant. However, the positions of the Cu atoms with respect to the bridging O atoms adjacent to the vacant sites varied with one Cu-O bond length between 1.98 Å and 2.08 Å, and the other between 2.32 Å and 2.60 Å. While one edge of the Cu chain was relatively close to a bridging O atom, the precise positions of the remaining atoms relative to the surface were found to be independent of the average binding energy for the Cu atoms.

The flexibility for this alignment of Cu chains with the TiO_2 surface, when located over two or more adjacent bridging O vacancies on the [001] row, plays an important role in Cu clustering. While a regular pattern of vacancies can be used to promote Cu growth such that the fcc Cu (110) plane forms parallel to the TiO_2 (110) surface, a large lattice mismatch of 13% still exists for Cu growth along the [001] direction of the surface. However, the grouping of bridging O vacancies along these [001] rows makes a precise alignment of the Cu cluster and the surface less important. This type of ordered vacancy arrangement was found for the experimental TiO_2 surface used to grow the large 260-780 Å wide Cu islands, and could account for part of the observed order of magnitude increase in Cu island size [47].

Chapter 9

Conclusions

Titanium dioxide surface science continues to be a rich and active field of study, due to the importance of this material in both basic research on oxides and a wide array of industrial applications. This dissertation has described contributions I have made in the theoretical understanding of certain key physical attributes of the surface properties of TiO_2. I anticipate the insights provided by these investigations will benefit ongoing and future studies of this important system. The three broad areas of my investigations of this system focused on (a) structural properties of the (110) surface, (b) interactions between bridging O vacancies, and (c) adsorption of Cu atoms and nanoclusters. A principle outcome of my structural research is the recommendation that TiO_2 and other covalently bonded crystals be described in terms of bond lengths and angles instead of absolute atomic positions. My research on surface oxygen vacancies provides explanations for the wide variety of experimentally observed bridging O vacancy arrangements, has reproduced common features of these arrangements through Monte Carlo simulation, and has predicted new ordered vacancy arrangements. Finally, my investigations of the adsorption of Cu on the TiO_2 surface both with and without oxygen vacancies have resulted in an improved knowledge and understanding of the binding and diffusion characteristics for Cu on TiO_2. These studies have also provided the basis for understanding the different growth modes that have been experimentally observed for the formation of Cu nanoclusters and islands.

Beginning with the surface structure, high precision calculations, along with newly published, more accurate experimental data, has resolved the long-standing discrepancies between experimental and theoretical results. Specifically, the absolute atomic positions obtained in my DFT calculations agree very closely with the experimental data, provided both sets of atomic positions are reported relative to the same fixed reference point. Furthermore, I determined that structural relaxations are better described in terms of bond lengths and bond angles, which do not require the designation of an arbitrary reference point. By making this transition to a more physical description of the surface structure, general agreement was observed not only between the present calculations and the recent experiment, but also with previous theoretical and experimental studies of the TiO_2 (110) surface. Therefore, presenting future descriptions of this material, and other covalently bonded solids, in terms of bond length and angles appears to provide a more useful and robust description of the crystalline structure.

In my investigations of surface structural properties, I determined that a computational model consisting of four trilayers, where the bottom two remain fixed in their bulk positions, is sufficient to accurately reproduce the surface structure. Since the relatively small primitive unit cell for this 4(2) model only contains 24 atoms, corresponding calculations are very efficient. While the adsorption of Cu is precisely modeled using this same thin slab model, the formation of a bridging O vacancy has a larger penetrating effect into the surface, resulting is a slightly larger precision error due to the finite slab thickness. Therefore, future advances in computational hardware and algorithmic improvements would allow for calculating vacancy interactions using sufficiently thick slabs.

The use of this accurate, computationally efficient, 4(2) model allows for the relatively fast computation of large surface regions, which has proven instrumental in the study of vacancy interactions and Cu nanocluster formation. Computations done

on surfaces containing up to eight primitive surface unit cells allowed for the study of numerous distinct bridging O vacancy arrangements. This was essential for the development of a vacancy-vacancy interaction model that is able to predict average vacancy formation energies in close agreement with full DFT calculations. Further exploration used Monte Carlo simulations to study larger surfaces that are comparable to those observed experimentally. These simulations predict two stable ordered vacancy arrangements, each persisting over a relatively wide range of surface chemical potentials. One of these phases occurs at 25% vacancy concentration and corresponds to the closest packing of effectively non-interacting (i.e., isolated) vacancies. The other occurs at 50% vacancy concentrations, where the heavily interacting vacancies are observed to form in pairs along the [001] bridging O rows. Other structural motifs revealed by these simulations include the formation of vacancy pairs at concentrations less than 50%, clusters of vacancies along [001] bridging O rows at higher concentrations, and the consistent pairing of bridging O atoms on surfaces with vacancy concentrations at or above 50%, all of which have also been observed experimentally. This robust DFT-parameterized interaction model provides physical explanations for each of the vacancy arrangements mentioned above.

Both the 25% and 50% ordered vacancy arrangements predicted using Monte Carlo simulations of my vacancy-vacancy interaction model can be described using a 1×4 non-orthogonal primitive unit cell. This is important for future calculations on reduced TiO_2 surfaces since the 1×4 cell has half the volume and number of atoms than the 2×4 orthogonal unit cell that has been more commonly used to study isolated bridging O vacancies. Therefore, this smaller unit cell enables future investigations on the non-stoichiometric TiO_2 surface with significantly less computational resources. This non-orthogonal 1×4 unit cell also permits more computationally efficient studies of adsorption of metals and molecules on the stoichiometric surface of TiO_2. Also,

similar non-orthogonal cells can be applied to studies on other crystals normally represented using orthogonal lattice vectors, saving additional time and resources.

My investigations on Cu adsorption have improved the current level of understanding about the different Cu-TiO_2 interactions that occur for Cu adatoms on the stoichiometric surface, near an isolated O vacancy, and near a pair of O vacancies. In general, the binding and diffusion characteristics of a Cu adatom on the non-stoichiometric surfaces are significantly different than those on the stoichiometric surface. For example, the diffusion of Cu atoms is significantly enhanced when the Cu atom is adsorbed on the [001] bridging O row in a pair or chain of vacancies, and is significantly weaker along the same [001] row near an isolated vacancy.

Further study on the adsorption of additional Cu atoms shows that details of the vacancy arrangement on the TiO_2 (110) surface has a profound effect on initial Cu cluster growth. On the stoichiometric surface, pairs of Cu atoms initially cluster in the $[\bar{1}10]$ direction, promoting Cu growth parallel to the TiO_2 surface. The adsorption of a third Cu atoms results in a Cu trimers that is oriented perpendicular to the surface. This demonstrates both the tendency of Cu atoms to cluster and the weak interaction between the surface and the adsorbed Cu atoms. These results are in good agreement with experimental observations on the stoichiometric surface, where small hemispherical islands have been observed to orient such that the fcc Cu (111) plane is parallel to the TiO_2 (110) surface.

The presence of bridging O vacancies has two important effects on the clustering of Cu atoms. First, the presence of isolated vacancies promotes initial Cu dimer formation in the [001] direction. The further growth of Cu clusters results in the formation of a Cu trimer whose plane is inclined at an angle of 22° towards the surface. This type of growth, where the fcc Cu (110) plane is parallel to the TiO_2 (110) surface, results in a much smaller lattice mismatch than growth on the stoichiometric surface. Second, Cu chains can be adsorbed on vacancy pairs along the [001] bridging O row

in many energetically equivalent orientations. This suggests that the remaining effect of the relatively large 13% lattice mismatch for Cu growth in the [001] direction of the surface is energetically less significant when Cu atoms are adsorbed over pairs (or longer lines) of vacancies. Experimental observations on a highly non-stoichiometric surface (67% vacancy concentration) are in very good agreement with these results. Specifically, as compared to Cu island formation on the stoichiometric surface, the Cu islands were observed to orient as described above, such that a smaller lattice mismatch occurs, resulting in island sizes that are an order of magnitude larger.

The investigations presented in this dissertation have also revealed new areas of interest that merit further study. For example, my vacancy-vacancy interaction model predicted ordered arrangements that have many features in common with experimentally observed surfaces. However, the precision of my model was not sufficient to include the longer ranged interactions necessary to predict the 67% ordered vacancy phase that has been observed experimentally. One way to improve the accuracy of this interaction model is to use thicker slabs, thereby reducing the precision error due to the finite slab thickness. Another example involves Cu clustering on the stoichiometric and non-stoichiometric surfaces. My DFT total-energy calculations support the different growth modes observed experimentally on these surfaces. However, due to the limitations on the number of atoms and size of the unit cell inherent to this method, they can not efficiently predict the formation of Cu islands. Whereas molecular dynamics simulations are well-suited to the study of larger systems, and could be used to overcome these system size problems in the study of Cu cluster growth. The calculated surface potentials for an adsorbed Cu atom could be incorporated into this type of study, since a functional form has been developed that contains a relatively small number of basis functions. This type of study would allow for investigations on the role played by specific bridging O vacancy concentrations and arraignments on Cu island formation on the TiO_2 (110) surface.

Bibliography

[1] Kaneko, M. and Okura, I. *Photocatalysis Science and Technology.* Springer, (2002).

[2] Henrich, V. E. and Cox, P. A. *The Surface Science of Metal Oxides.* Cambridge, (1994).

[3] Kawai, T. and Sakata, T. *J. Chem. Soc., Chem. Commun.* , 695 (1980).

[4] Kanno, H., Yamamoto, Y., and Harada, H. *Chem. Phys. Lett.* **121**, 245 (1985).

[5] Ohtani, B., Imai, K., i. Nishimoto, S., and Sato, S. *J. Phys. Chem. B.* **101**, 3746 (1997).

[6] Martin, R. M. *Electronic Structure Basic Theory and Practical Methods.* Cambridge, (2004).

[7] Kresse, G. and Furthmüller, J. *Phys. Rev. B* **54**, 11169 (1996).

[8] Kresse, G. and Furthmüller, J. *Compt. Mat. Sci.* **6**, 15 (1996).

[9] Kresse, G. and Furthmüller, J. *VASP: the Guide.* Wien, Austria, (2003).

[10] Vijay, A., Mills, G., and Metiu, H. *J. Chem. Phys.* **118**, 6536 (2003).

[11] Iddir, H., Öğüt, S., Browning, N. D., and Disko, M. M. *Phys. Rev. B* **72**, 081407 (2005).

[12] Iddir, H., Skavysh, V., Öğüt, S., Browning, N. D., and Disko, M. M. *Phys. Rev. B* **73**, 41403 (2006).

[13] Wang, Y. and Hwang, G. S. *Surf. Sci.* **542**, 72 (2003).

[14] Pillay, D., Wang, Y., and Hwang, G. S. *Catalysis Today* **105**, 78 (2005).

[15] Pillay, D. and Hwang, G. S. *Phys. Rev. B* **72**, 205422 (2005).

[16] Wörz, A. S., Heiz, U., Cinquini, F., and Pacchioni, G. *J. Phys. Chem. B* **109**, 18418 (2005).

[17] Blöchl, P. E. *Phys. Rev. B* **41**, 5414 (1990).

[18] Vanderbilt, D. *Phys. Rev. B* **41**, 7892 (1990).

[19] Abrahams, S. C. and Bernstien, J. L. *J. Chem. Phys.* **55**, 3206 (1971).

[20] Manghnani, M. H., Fisher, E. S., and W. S. Brower, J. *J. Phys. Chem. Solids* **33**, 2149 (1972).

[21] Glassford, K. M. and Chelikowsky, J. R. *Phys. Rev. B* **46**, 1284 (1992).

[22] Muscat, J., Swamy, V., and Harrison, N. M. *Phys. Rev. B* **65**, 224112 (2002).

[23] Charlton, G., Howes, P. B., Nicklin, C. L., Steadman, P., Taylor, J. S. G., Muryn, C. A., Harte, S. P., Mercer, J., McGrath, R., Norman, D., Turner, T. S., and Thornton, G. *Phys. Rev. Lett.* **78**, 495 (1997).

[24] Ramamoorthy, M., King-Smith, R. D., and Vanderbilt, D. *Phys. Rev. B* **49**, 7709 (1994).

[25] Swamy, V., Muscat, J., Gale, J. D., and Harrison, N. M. *Surf. Sci.* **504**, 115 (2002).

[26] Elliott, S. D. and Bates, S. P. *Surf. Sci.* **495**, 211 (2001).

[27] Bates, S. P., Kresse, G., and Gillan, M. J. *Surf. Sci.* **385**, 386 (1997).

[28] Lindan, P. J. D., Harrison, N. M., Gillan, M. J., and White, J. A. *Phys. Rev. B* **55**, 15919 (1997).

[29] Lindan, P. J. D., Muscat, J., Bates, S. P., Harrison, N. M., and Gillan, M. J. *Faraday Discuss.* **106**, 135 (1997).

[30] Sano, H., Mizutani, G., Wolf, W., and Podloucky, R. *Phys. Rev. B* **70**, 125411 (2004).

[31] Vogtenhuber, D., Podloucky, R., Neckel, A., Steinmann, S. G., and Freeman, A. J. *Phys. Rev. B* **49**, 2099 (1994).

[32] Thompson, S. J. and Lewis, S. P. *Phys. Rev. B* **73**, 073403 (2006).

[33] Thompson, S. J. and Lewis, S. P. *Computer Simulation Studies in Condensed-Matter Physics*, volume 19. edited by D. P. Landau, S. P. Lewis, and H.-B. Schüttler, Springer Proceedings in Physics, (in press).

[34] Lindsay, R., Wander, A., Ernst, A., Montanari, B., Thornton, G., and Harrison, N. M. *Phys. Rev. Lett.* **94**, 246102 (2005).

[35] Bredow, T., Giordano, L., Cinquini, F., and Pacchioni, G. *Phys. Rev. B* **70**, 035419 (2004).

[36] Wang, S.-G., Wen, X.-D., Cao, D., Li, Y.-W., Wang, J., and Jiao, H. *Surf. Sci.* **577**, 69 (2005).

[37] Hameeuw, K., Cantele, G., Ninno, D., Trani, F., and Iadonisi, G. *Phys. Stat. Sol. (a)* **203**, 2219 (2006).

[38] Wendt, S., Schaub, R., Matthiesen, J., Vestergaard, E. K., Wahlström, E., Rasmussen, M. D., Thostrup, P., Molina, L. M., Laegsgaard, E., Stensgaard, I., Hammer, B., and Besenbacher, F. *Surf. Sci.* **598**, 226 (2005).

[39] Thompson, T. L. and J. T. Yates, J. *Topics in Catalysis* **35**, 197 (2005).

[40] Bouzoubaa, A., Markovits, A., Calatayud, M., and Minot, C. *Surf. Sci.* **583**, 107 (2005).

[41] Diebold, U. *Appl. Phys. A* **76**, 681 (2003).

[42] Kuyanov, I. A., Lacks, D. J., and Diebold, U. *Phys. Rev. B* **68**, 233404 (2003).

[43] Bredow, T. and Pacchioni, G. *Chem. Phys. Lett.* **355**, 417 (2002).

[44] Oviedo, J., Miguel, M. A. S., and Sanz, J. F. *J. Chem. Phys.* **121**, 7427 (2004).

[45] Tilocca, A. and Selloni, A. *Chem. Phys. Chem.* **6**, 1911 (2005).

[46] Namai, Y. and Matsuoka, O. *J. Phys. Chem. B* **109**, 23948 (2005).

[47] Wagner, M., Kienzle, O., Bonnell, D. A., and Rühle, M. *J. Vac. Sci. Technol. A* **16**, 1078 (1998).

[48] Wagner, M., Bonnell, D. A., and Rühle, M. *Appl. Phys. A Material Science and Processing* **66**, S1165 (1998).

[49] Landau, D. P. and Binder, K. *A Guide to Monte Carlo Simulations in Statistical Physics.* Cambridge, (2005).

[50] Tanizawa, Y., Shido, T., Chun, W. J., Asakura, K., Nomura, M., and Iwasawa, Y. *J. Chem. Phys. B* **107**, 12917 (2003).

[51] Reddic, J. E., Zhou, J., and Chen, D. A. *Surf. Sci.* **494**, L767 (2001).

[52] Zhou, J., Kang, Y. C., and Chen, D. A. *J. Phys. Chem. B* **107**, 6664 (2003).

[53] Zhou, J. and Chen, D. A. *Surf. Sci.* **527**, 183 (2003).

[54] Diebold, U., Pan, J. M., and Madey, T. E. *Phys. Rev. B* **47**, 3868 (1993).

[55] Moller, P. J. and Wu, M.-C. *Surf. Sci.* **224**, 265 (1989).

[56] Ashcroft, N. W. and Mermin, N. D. *Solid State Physics*. Brooks/Cole, 64 edition, (1976).

[57] Diebold, U. *Surf. Sci. Rep.* **49**, 1 (2002).

[58] www.chemlink.com.au/titanium.htm. *Titanium Dioxide Pigment*. online, (1997).

[59] Fujishima, A., Kobayakawa, K., and Honda, K. *J. Eletrochem. Soc.* **122**, 1487 (1975).

[60] Wang, R., K. Hashimoto, A. F., Chikuni, M., Kojima, E., Kitamura, A., Shimohigoshi, M., and Watanabe, T. *Nature* **388**, 431 (1997).

[61] Ohtani, B., Okugawa, Y., i. Nishimoto, S., and Kagiya, T. *J. Phys. Chem.* **91**, 3550 (1987).

[62] Ohtani, B., Kominami, H., Bowman, R. M., Jr., P. C., Noguchi, H., and Uosaki, K. *Chem. Lett.* , 579 (1998).

[63] Landsberg, P. T. *Recombination in Semiconductors*. Cambridge, (1991).

[64] Giordano, L., Pacchiono, G., Bredow, T., and Sanz, J. F. *Surf. Sci.* **471**, 21 (2001).

[65] Molina, L. M., Rasmussen, M. D., and Hammer, B. *J. Chem. Phys.* **120**, 7673 (2004).

[66] Ding, K., Li, J., and Zhang, Y. *J. Molec. Struct. THEOCHEM* **728**, 123 (2005).

[67] Coloma, F., Marquez, F., Rochester, C. H., and Anderson, J. A. *Phys. Chem. Chem. Phys.* **2**, 5320 (2000).

[68] Wagner, T., Marien, J., and Duscher, G. *Thin Solid Films* **398-399**, 419 (2001).

[69] Hohenberg, P. and Kohn, W. *Phys. Rev.* **136**, B864 (1964).

[70] Kohn, W. and Sham, L. J. *Phys. Rev.* **140**, A1133 (1965).

[71] Hartree, D. R. *Proc. Cambridge Philos. Soc.* **24**, 89 (1928).

[72] Fock, V. *Z. Physik* **61**, 126 (1930).

[73] Wigner, E. *Phys. Rev.* **46**, 1002 (1934).

[74] Gell-Mann, M. and Brueckner, K. A. *Phys. Rev.* **106**, 364 (1957).

[75] Fetter, A. L. and Walecka, J. D. *Quantum Theory of Many-Particle Systems.* Dover, (2003).

[76] Jones, R. O. *Introduction to Density Functional Theory and Exchange-Correlation Energy Functionals in Computational Nanoscience: Do It Yourself!, NIC Series*, volume 31. edited by J, Grotendorst, S. Blügel, and D. Marx, John von Neumann Institute for Computing, Jülich, (2006).

[77] Grinberg, I., Ramer, N. J., and Rappe, A. M. *Phys. Rev. B* **63**, 201202 (2001).

[78] C. Filippi, C. J. U. and Taut, M. *J. Chem. Phys.* **100**, 1290 (1994).

[79] Boese, A. D. and Handy, N. C. *J. Chem. Phys.* **114**, 5497 (2001).

[80] Perdew, J. P., Burke, K., and Ernzerhof, M. *Phys. Rev. Lett.* **77**, 3865 (1996).

[81] Becke, A. D. *Phys. Rev. A* **38**, 3098 (1988).

[82] Perdew, J. P. and Wang, Y. *Phys. Rev. B* **45**, 13244 (1992).

[83] Payne, M. C., Teter, M. P., Allan, D. C., Arias, T. A., and Joannopoulos, J. D. *Rev. Mod. Phys.* **64**, 1045 (1992).

[84] Monkhorst, H. and Pack, J. *Phys. Rev. B* **13**, 5188 (1976).

[85] Teter, M. P., Payne, M. C., and Allen, D. C. *Phys. Rev. B* **40**, 12255 (1989).

[86] Bylander, D. M., Kleinman, L., and Lee, S. *Phys. Rev. B* **42**, 1394 (1990).

[87] Davidson, E. R. *Methods in Computational Molecular Physics*, volume 113. edited by G. H. F. Dickerson and S. Wilson, Plenum, New York, (1983).

[88] Wood, D. M. and Zunger, A. *J. Phys. A* , 1342 (1985).

[89] Pulay, P. *Chem. Phys. Lett.* **73**, 393 (1980).

[90] Press, W. H., Flannery, B. P., Teukolsky, S. A., and Vetterling, W. T. *Numerical Recipes in FORTRAN 77: The Art of Scientific Computing.* Chapter 12. Cambridge, (1992).

[91] Methfessel, M. and Paxton, A. T. *Phys. Rev. B* **40**, 3616 (1989).

[92] Tinkham, M. *Group Theory and Quantum Mechanics.* Dover, (2003).

[93] *CRC Handbook of Chemistry and Physics.* CRC, (1983).

[94] Overbury, Bertrand, and Somorjai. *Chem. Rev.* **75**, 547 (1975).

[95] Parkinson, G. S., Muñoz-Márquez, M. A., Quinn, P. D., Gladys, M. J., Tanner, R. E., Woodruff, D. P., Baily, P., and Noakes, T. C. Q. *Phys. Rev. B* **73**, 245409 (2006).

[96] Göpel, W., Rocker, G., and Feierabend, R. *Phys. Rev. B* **28**, 3427 (1983).

[97] Calatayud, M., Markovits, A., Menetrey, M., Mguig, B., and Minot, C. *Catalysis Today* **85**, 125 (2003).

[98] Menetrey, M., Markovits, A., and Minot, C. *Surf. Sci.* **524**, 49 (2003).

[99] Linsebigler, A., Lu, G., and J. T. Yates, J. *J. Chem. Phys.* **103**, 9438 (1995).

[100] Li, J., Wu, L., and Zhang, Y. *Chem. Phys. Lett.* **342**, 249 (2001).

[101] Wu, X., Selloni, A., and Nayak, S. K. *J. Chem. Phys.* **120**, 4512 (2004).

[102] Walter, E. J. and Rappe, A. M. *Surf. Sci.* **427-428**, 11 (1999).

[103] Jr., M. W. C., Davies, C. A., Jr., J. R. D., Frurip, D. J., McDonald, R. A., and Syverud, A. N. *J. Phys. Chem. Ref. Data* **11 (Suppl. 2)** (1982).

[104] Binder, K. and Landau, D. P. *Surf. Sci.* **108**, 503 (1981).

[105] Einstein, T. L. *Physical Structure at Solid Surfaces, in Handbook of Surface Science*, volume 1, 577. edited by W. N. Unertl, Elsevier, (1996).

[106] de Fontaine, D. *Cluster Approach to Order-Disorder Transformations in Alloys, in Solid State Physics*, volume 47. edited by H. Ehrenreich and D. Turnbull, Academic Press, (1994).

[107] Kirkpatrick, S. and Stoll, E. *J. Comput. Phys.* **40**, 517 (1981).

[108] www.csp.uga.edu/Resources/resource/rn1279 standalone.f95. *Random number generator R1279.* online, (2004).

[109] Metropolis, N., Rosenbluth, A. W., Rosenbluth, M. N., Teller, A. H., and Teller, E. *J. Chem. Phys.* **21**, 1087 (1953).